Optimized Energy Management for Serial Hybrid Vehicles

Sebastien Rouquet

THÈSE DE DOCTORAT DE

L'ÉCOLE CENTRALE DE NANTES

ÉCOLE DOCTORALE N° 601
Mathématiques et Sciences et Technologies de l'Information et de la Communication
Spécialité : Génie électrique

Par
Sébastien ROUQUET

Gestion d'énergie optimisée pour véhicule hybride série

Thèse présentée et soutenue à Centrale Nantes, le 5 juillet 2021
Unité de recherche : UMR 6004, Laboratoire des Sciences du Numérique de Nantes (LS2N)

Rapporteurs avant soutenance :

Xuefang LIN-SHI	Professeure des Universités, INSA Lyon
Olivier GEHAN	Maître de Conférences HDR, ENSICAEN

Composition du Jury :

Président :	Maurice FADEL	Professeur des Universités, ENSEEIHT/INPT, Toulouse
Examinateurs :	Rosane USHIROBIRA	Chargée de Recherche HDR, INRIA Lille
	Jean-Pierre BARBOT	Professeur des Universités, ENSEA - Centrale Nantes
Dir. de thèse :	Malek GHANES	Professeur des Universités, École Centrale de Nantes
Co-enc. de thèse :	Yuri SHTESSEL	Distinguished Professor, University of Alabama in Huntsville (États-Unis)

Invité :

Ludovic MERIENNE	Ingénieur de Recherche, Technocentre Renault, Guyancourt

Acknowledgement

Les résultats de cette thèse sont le fruit d'une collaboration entre le groupe Renault et le laboratoire LS2N de l'Ecole Centrale de Nantes. Je souhaite remercier très chaleureusement mes encadrants. Un grand merci à mon directeur de thèse Pr. Malek Ghanes et mon co-directeur Pr. Yuri Shtessel qui m'ont soutenu et encouragé tout le long de cette thèse. J'adresse aussi mes remerciements aux Pr. Franck Plestan, Pr. Jean-Jacques Loiseau et Pr. Jean-Pierre Barbot pour leurs nombreux conseils. Du côté de Renault, je tiens à remercier tout particulièrement mon encadrant M. Ludovic Merienne qui a su donner une perspective intéressante à mes travaux et cela aux travers de nombreuses discussions. Je souhaiterais aussi exprimer ma gratitude envers M. Ahmed Ketfi-Cherif et M. Abdelmalek Maloum de Renault, pour leurs soutiens et encouragements.

Je remercie Pr. Maurice Fadel et Pr. Rosane Ushirobira de m'avoir suivi, conseillé et d'avoir accepté de faire partie du jury de la soutenance de thèse. Je remercie Pr. Xuefang Lin-Shi et Pr. Olivier Géhan d'avoir accepté de juger mon travail en tant que rapporteurs.

Mes remerciements s'adressent aussi à tous mes collègues, Stéphane, Maël, Robert, Arnaud, Bob, Damien, Rémi, Philippe L., Denis, Sébastien, Yassir, Amir, Adrien, Houssein, Christine, Philippe P., Peggy, Sabine et j'en oublie sûrement, qui m'ont précieusement entouré, avec qui les pauses étaient toujours animées et remplies de bonne humeur.

Je souhaite aussi remercier ma famille et mes amis pour leur soutien et encouragement. Pour finir, je souhaite particulièrement remercier deux personnes, car sans eux je n'en serais pas ici aujourd'hui: Hamza, Marie, merci!

Table of Contents

List of Figures

List of Abbreviations and Symbols

EV	Electric Vehicle
HEV	Hybrid Electric Vehicle
PHEV	Plug-in Hybrid Electric Vehicle
BEV	Battery Electric Vehicle
AC	Alternative Current
DC	Direct Current
PMSM	Permanent Magnet Synchronous Motor
PWM	Pulse Width Modulation
IGBT	Insulated Gate Bipolar Transistor
M1	Traction motor
M2	High voltage alternator
ICE	Internal Combustion Engine
R_s	Stator resistance
L_d, L_q	dq-axis inductances
L_0, L_2	Average and differential inductances
Φ_f	Permanent magnet flux
i_d, i_q	Stator current in dq-axis
v_d, v_q	Stator voltage in dq-axis
i_a, i_b, i_c	Stator current in abc-axis
v_a, v_b, v_c	Stator voltage in abc-axis
θ	Electric angular position
Ω	Rotational speed of the ICE and the flywheel
R_{M2}	Reduction ratio between the ICE and the M2
Ω_{M2}	Rotational speed of the M2
Ω_{M1}	Rotational speed of the M1
J	Moment of inertia on the ICE shaft
T_{ICE}	Output torque of the ICE
T^*_{ICE}	Torque request for the ICE
T_{M1}	Output torque of the M1
T^*_{M1}	Torque request for the M1
i_{M1}	DC bus current of the M1
P_{l1}	The M1 electrical losses

T_{M2}	Output torque of the M2
T^*_{M2}	Torque request for the M2
i_{M2}	DC bus current of the M2
P_{l2}	The M2 electrical losses
U_{DC}	Voltage of the DC bus
i_{aux}	DC bus current of the auxiliary circuit
T_r	The friction torque on the flywheel axle
S_a, S_b, S_c	IGBT control signal
α_a, α_b, α_c	PWM duty cycle
V_D	Inverters diode reverse voltage
T_D	Inverters deadtime
V_{car}	Speed of the car
m_{car}	Car mass
$R_{gearbox}$	Gearbox ratio
r_{wheel}	Wheels radius

List of the powertrain parameters introduced in the thesis

System	Symbol	Value	Unit
ICE	τ_+	$10\pi/3$	-
	τ_-	$40\pi/3$	-
	$\tau_\pm$	$25\pi/3$	-
M1	p	8	-
	R_s	0.035	Ω
	L_d	0.23	mH
	L_q	0.3	mH
	Φ_f	0.083	Wb
M2	p	4	-
	R_s	0.035	Ω
	L_d	0.1	mH
	L_q	0.3	mH
	Φ_f	0.042	Wb
	R_{M2}	2.52	-
Inverters	V_D	2.5	V
	T_D	1	μs
Inertia	J	40	gm^2
Capacitor	C	1	mF
Car	m_{car}	1500	kg

Table 2 – The E-TECH simulation parameters

General introduction

This thesis is part of the Renault Chair project for the improvement of vehicle propulsion. The goal of this partnership is to innovatively contribute to the development of novel control strategy for future vehicles based on electric and hybrid propulsion. In this context, this thesis mainly contributes to increasing the robustness, reliability and performance of control strategies for vehicles based on the aforementioned propulsion architectures. These improvements also lead to potential reductions in risk of damage, costs and implementation issues.

0.1 Background

During the last decades, Hybrid Electrical Vehicles (HEV) have emerged as a viable alternative to the traditional fuel powered automobiles despite the latter's historical market dominance [van+10]. Indeed, petrol powered engines have occupied the majority of the market for a century. This dominance was largely the result of fossil fuels enabling extended travel distances and faster refuel time at relatively low costs [Edw11; ADE18]. However, these benefits of the Internal Combustion Engine (ICE) are counteracted by the emissions resulting from its fossil fuel consumption. In other words, the convenience of ICE vehicles was enjoyed at the expense of their environmental footprint.

This trend is being challenged as awareness of the dependency on non-renewable energies and its resulting impact on air quality is increasing. This change of perception is expected to greatly influence vehicle sales. This claim is backed by the projected distribution of new light-duty vehicle sales sorted by drive type between 2017 and 2035 shown in figure 1. It is expected that the share of pure gasoline and diesel engine vehicles will plummet from their 2017 level of 95% to quasi-irrelevance, while the sales of HEVs increases from 3.1% to 62.6% with a further 24.4% sales being taken by Battery Electric Vehicles (BEV). Indeed, HEVs are a rather attractive candidate as they significantly reduce toxic and harmful gas emissions without sacrificing travel range.

HEVs have gone through several design iterations throughout their development history, amongst which are planetary gear-based architectures, dual clutch serial–parallel,

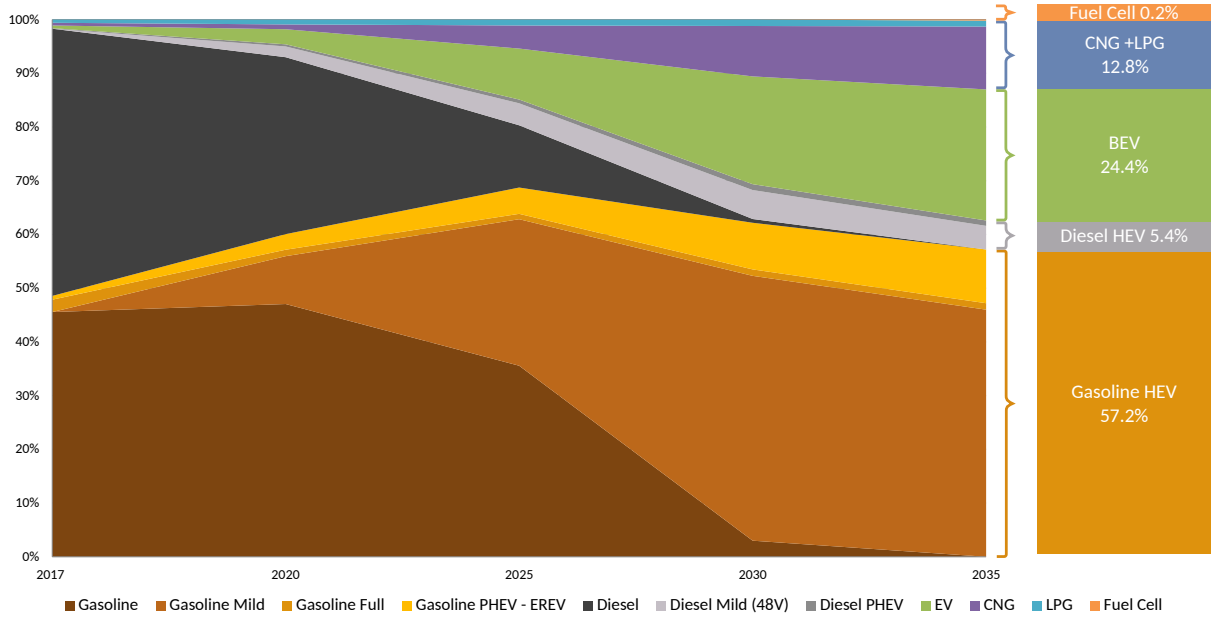

Figure 1 – Study of the predicted distribution of new light-duty vehicle sales over the 2017 to 2035 period sorted by drive-train. Taken from [PFA18]

Continuous Variable Transmission (CVT) and range extender. However, vehicle manufacturers need to innovate on existing architectures in order to improve HEV sales.

The HEV architecture studied in this thesis is one of the newer concepts, it is made possible by the development of a robust control system. It is based on the combination of an ICE coupled with a high voltage alternator and an electric motor. The gearbox is designed to connect the ICE and the electric motor independently of each other to the wheels. A tradeoff was necessary in order to fit the powertrain in a light-duty car: the clutch and mechanical synchronization typically found in a classical gearbox were removed, and replaced with a control software. In this configuration, the control software synchronizes the axle speed for the gear shifting and supervises the traction of the car.

0.2 Problem statement

In the context of serial HEVs, fine control strategies are required by the system in the event of main battery disconnection. Indeed, in the absence of the main battery, the powertrain has very limited energy storage capabilities, thus making the system sensitive to small disturbances. In the sequel, the technological context of the serial HEV without the battery is introduced and a state of art is presented.

0.2.1 Technological context

The core of our study is without the main battery, the control reaction has to be sufficient to absorb both the transient disturbance and the persistent disturbance. In order to achieve this, it is necessary to design a control algorithm able to maintain the level of two energies buffers: the rotational speed of the flywheel and the voltage of the capacitor. These energies buffers are the key to maintain the power transmission needed to propel the vehicle.

In the serial hybrid mode, the power goes from the ICE to the electric motor driving the wheel. The ICE produces mechanical power by burning the fuel, a high voltage alternator converts this power into electrical power and an electrical motor uses this power to propel the vehicle. The ICE is connected to the alternator through a flywheel. This flywheel is originally designed to smooth the torque produce by the ICE, but here the flywheel acts like a mechanical energy buffer. The alternator is connected to the electrical motor via a DC bus. On a normal serial hybrid DC bus, the battery acts like an electrical buffer and a capacitor is used to filter Pulse Width Modulation (PWM) harmonics of the inverter. However, here without the battery, the only electrical buffer is the capacitor present on the DC bus. Thus, from the ICE to traction motor, the level of energy buffer available along the power transmission are represented by the capacitor voltage and the flywheel rotational speed, making them two critical buffers.

The system under consideration has the particularity of having three concurrent time scales. The small and large time scales representing the fast and slow dynamics respectively. The small time scale is the current dynamic of each electric motor (the alternator and the traction motor), while the medium time scale is the voltage dynamic of the DC bus and the larger one is the rotational speed dynamic of the flywheel between the ICE and the alternator. The challenge is to control each one of them with the constraint of a slow variation of the ICE torque, a fast variation of the electric current and the sampling periods of the control unit. Moreover, working with an ICE introduces the issue of implanting precise torque control on an entity involving chemical transformation.

Handling these varying time scales are a fundamental driver of the control design, as it needs to provide a strategy that is simultaneously successful in partitioning the control, maintaining the level of energy buffer, assessing the perturbations and improving the operation of the powertrain.

0.2.2 State of the art

In the literature, many works have been developed around HEVs. Figure 2 presents, the main authors held on different topics developed in this thesis, which are: the energy management for HEV, the dynamic model of the ICE, the coupling of an ICE with a PMSM, the modeling of the PMSM, control approaches and industrial patents.

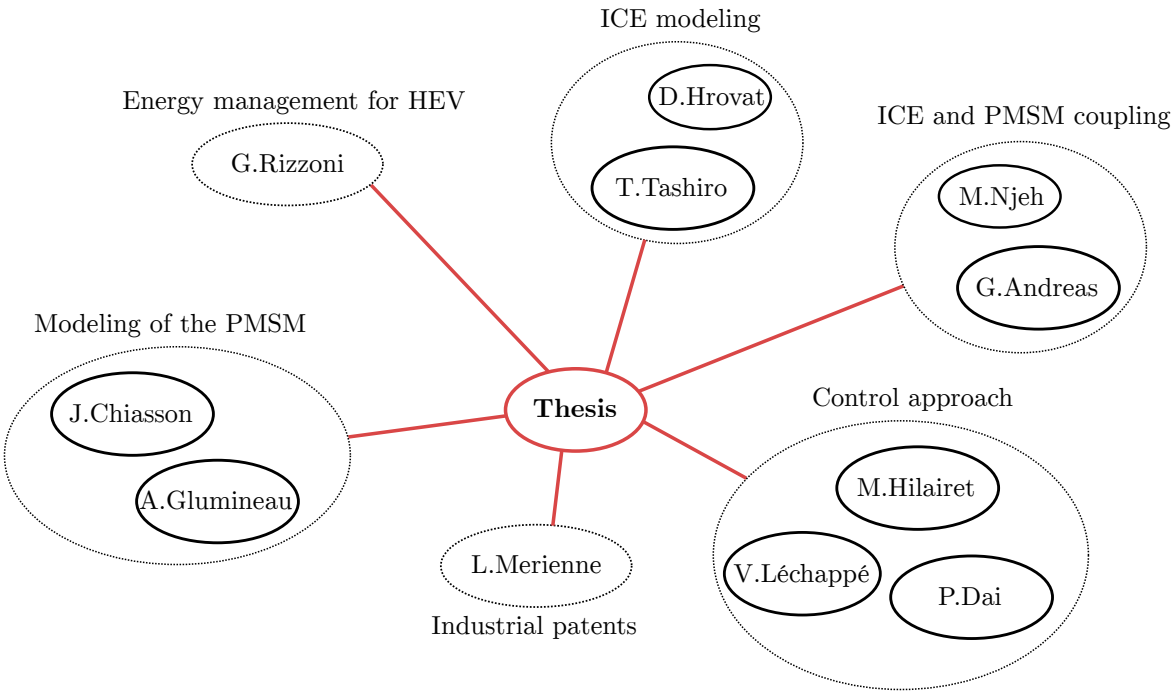

Figure 2 – Bibliography oriented between differents topics

[RO15] resumes 15 years of development on energy management of hybrid electric vehicle. With steady state models, different methods are developed: Rule-Based, Equivalent Consumption Minimization, Dynamic Programming, Optimal Method and Pontryagin's Minimun Principle. The ICE torque dynamic has been modeled as a second order linear system to achieved traction control with a model predictive control in [TM17]. A more sophisticated approach, resembling at the model used in this thesis, can be found in this article [HS97] and in this thesis [Bre12]. The physics involve in synchronous motor has been studied and published in the book [Chi05]. The modeling and control approach of the PMSM has been explain in [AD05]. The book has given the opening of controlling the PMSM without the angular sensor and more recently the thesis of [Mes19] has been given a more detailed on the sensorless control of the PMSM. The coupling of an ICE with a PMSM has presented the opportunity to reduce the torque ripple induced by the

ICE with a PMSM [NCC10], while the opportunity of removing the ICE throttle and controlling the generated power has been studied in [Ger+16]. The background utility of disconnecting the battery of the E-TECH powertrain is detailed in patent [MK17], where more details on the gearbox control can be found in this patent [MK16]. The last axis has been the control approaches that inspired the work of this thesis: the predictive approach used to control input delay system in [Léc+16], the two time scales system formed by a fuel cell and a supercapictor in [Hil+13] and the two time scales system formed by a supercapictor and a battery in [Dai15].

To our best knowledge the existing works have tackled only parts of the problem and have never considered the thesis technological context, i.e. the energy management of the serial HEV without the main battery.

0.3 Objectives

With respect to the technological context, the objective of this work is to devise a control strategy that achieves the traction demand required by the driver in a serial hybrid vehicle without a battery according to the technological context.

In order to achieve this global objective, the following quantities must be controlled:

— the current of the electric motors,

— the voltage of the DC bus,

— the rotational speed of the flywheel.

After proposing different strategies, the interaction between these control stages are then studied with the singular perturbation approach. The technical difficulties are to control the different time scales while rejecting the disturbances and improving the time response of the serial mode. In doing so, it is possible to achieve a better understanding of the coupling between time scales and prove the stability of the overall control system. Additional control objectives include fulfilling the voltage and rotational speed references so as to avoid exceeding the power limit of each element.

The control algorithm developed in this work emerged from the need to overcome a major failure happening to the main battery. In this case, the study presented at the beginning of this thesis has been required to overcome the battery failure. But, the idea driving this research has been to provide a more advance solution, where the battery can be safely disconnected to improve the traction performance when the battery is cold or discharged.

The last objective studied in the thesis consists of proposing a strategy for improving the responsiveness on transient traction demand from the driver. The approach developed here is to delay the driver demand in order to store energy while providing an improved feeling response.

0.4 Organization of the thesis

The thesis is organized following the main axis considered in this work, which are: feasibility of the DC bus voltage regulation, strategies for the control of the rotational speed of the flywheel, power management and finally the validation of the developed algorithm on a test bench. Accordingly, chapter 2 of this thesis presents the work related to the DC bus voltage control; chapters 3 and 4 refer to the work performed to control the rotational speed of the flywheel; while chapter 5 is centered around the power management and chapter 6 covers the experimental axis.

In each chapter, the modeling, control law and simulation needed to properly asses each axis are presented. For readers interested in reading this thesis following the organization modeling, control design, simulation and experimentation; the relevant sections of this manuscript to each activity are presented below:

— system modeling: 2.2, 3.2 and 5.2,
— control design: 2.3, 4.2 and 5.4.3,
— simulation: 3.3.1, 3.3.1, 3.3.2, 3.3.3 and 5.4.4,
— experimentation: 6.

Chapter 1 presents a first review of the working principles of hybrid powertrains, the specific context of this thesis and the characteristics of the powertrain considered in this work.

Chapter 2 introduces the control of the DC bus voltage. The modeling of each electrical part is covered. The design of the voltage control is developed and simulation results are shown in the nominal case and in a more advanced case.

In chapter 3, the modeling is made for larger time scale than the last chapter and the system in its entirety is considered. The idea is to show the different strategies existing for the control of two critical parts of the hybrid serial vehicle. The performances of the strategies are then compared on key performance indicators and one of them is subsequently selected.

Chapter 4 provides an in-depth presentation of the previously selected strategy. A bet-

ter understanding of the time scale coupling is achieved through the singular perturbation and regulation performance is improved with input-output injection observers.

Chapter 5 proposes a power management strategy that ultimately provides the references for the flywheel rotational speed and the DC bus voltage in order to fulfill the user demand. The principal aim behind the power management is to deal with the saturation of each element of the hybrid serial vehicle and find the best references that lead to the realization of the driver's request.

In chapter 6, experiments are carried out to further verify the effectiveness of the control algorithm designed in the previous chapters. The test bench is introduced and the effect of the scale difference between the vehicle powertrain and the bench parameters is discussed. The control algorithms presented in the previous chapters are recalled and applied in the test bench configuration. The experimental results are presented and explained.

The final chapter concludes this thesis manuscript and provides recommendations for further research.

0.5 Contributions of the thesis

This work led to several publications and a patent:

— Patent deposit number: 2102130, S. Rouquet, M. Ghanes and L. Merienne, *Commande d'un groupe motopropulseur d'un véhicule automobile hybride fonctionnant dans un mode série à batterie déconnectée* (Accepted).

— S. Rouquet, M. Ghanes, J.P. Barbot, L. Merienne, *Power Management in Serial Hybrid Electric Vehicle: A singular perturbation approach*, 21th IFAC World Congress, Berlin, Germany, IFAC-PapersOnLine, Volume 53, Issue 2, 2020, Pages 13775-13780, ISSN 2405-8963, https://doi.org/10.1016/j.ifacol.2020.12.885.

— S. Rouquet, M. Ghanes, J.P. Barbot, Y.B. Shtessel and L. Merienne, *Energy management in a mechatronics system with delay: A series hybrid electric vehicle case*, 2020 IEEE Conference on Control Technology and Applications (CCTA), 2020, pp. 679-684, Montréal, Canada, doi: 10.1109/CCTA41146.2020.9206269.

— S. Rouquet, M. Ghanes, J.P. Barbot, Y.B. Shtessel and L. Merienne, *Energy management in a mechatronics system with delay: A series hybrid electric vehicle case* 2021 IEEE Transactions on Control Systems Technology (Submited).

Chapter 1

The E-TECH powertrain: from the concept to the technical difficulties

Over the last 25 years, the traction energy of a car has evolved from internal combustion engine and electric motor to a more sophisticated fusion between the two technologies. Although hybrid vehicle architectures promise to take the advantages of both technologies in term of the energy efficiency of the electric, the long range and quick fuel reload capabilities of the ICE; they also raise an increasing number of technical challenges. In order to understand the latter, it is first necessary to delve into the details of HEV architecture and the varying hybridization sizing's.

This chapter presents declination and usage of the HEV, then the powertrain concept is introduced in order to present his operation and then culminates in presenting a complete statement of the technical difficulties overcome in this thesis.

1.1 Declination and usage of the HEV

Through the possible architecture and size of a HEV, the background needed to understand the placement of the powertrain studied in this thesis is given.

Architecture of the HEV

The HEV can be decomposed on several architectures [Kes+08; MV00; Gaz19; Mal14], see figure 1.1.

The four architectures are characterized by the available path for the power coming from the fuel or the battery and going to the wheels of the car. Essentially the architectures use distinct gearboxes to provide different power paths. The power in the serial

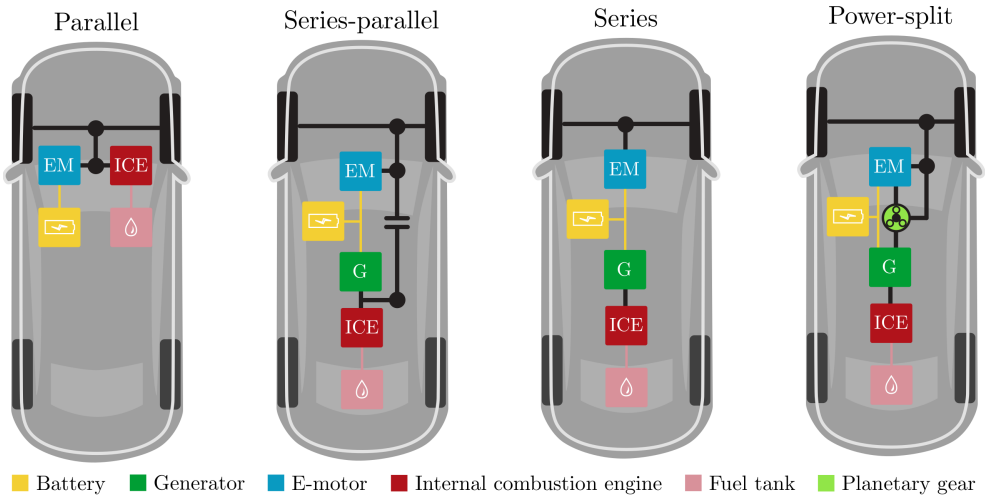

Figure 1.1 – HEV architectures

architecture goes from the combustion of the fuel in the ICE to the rotational power, converted into electrical power and then converted back into the mechanical power used to propel the car. The parallel architecture can independently utilize the combustion energy or the electrical energy to propel the car. With the combination of the two architectures, the serial-parallel architecture can run in serial or parallel mode. This combination allows to take the advantage of both architectures. Coming from the serial architecture, the ICE is able to run at the best efficiency point. The parallel architecture permits the power to be converted from the fuel tank to the wheel without the electric conversion and without the downside of the efficiency accumulation of the conversions in the serial mode. The power-split is a planetary gear-based architecture. Each input of the planetary gear is coupled to a motor (ICE or electrical motor). It introduces a constant mix between the electric and fuel power and it has to be constantly powered by each input, i.e. the system cannot work only with the ICE or the electrical motor. In all cases, the battery acts as a reversible storage and as it can be seen in the next part fixes another characteristic of the HEV.

Various size of the hybridization

The HEV can also be decomposed on several scales [TS09; Har12]:

— Micro,

— Mid,

— Full,

— Plug-in,
— Extended range.

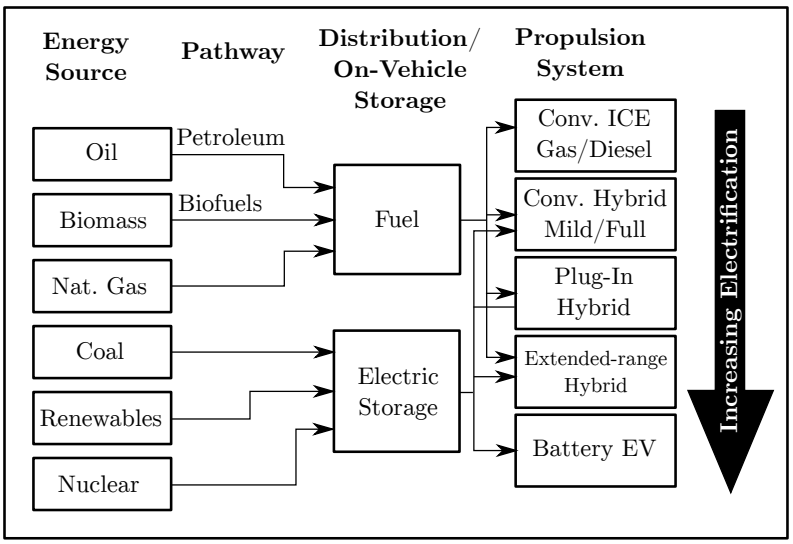

Figure 1.2 – HEVs topologies [TS09]

From the micro hybrid to the extender range hybrid, the scale depends on the level of the electrical power used in the hybridization. The micro hybrid is often characterized to a start and stop system, allowing to frequently stop the ICE when the vehicle is not moving. The mild/full hybrid represents the possibility to retrieve energy from deceleration of the car and made the best use of the ICE by recharging the battery when it is underused. The plug-in hybrid originates from a larger battery than the last scale and the possibility to recharge the vehicle by plug-in the car to the electric network. The range extender is a powertrain sized to principally use the electrical propulsion and only power on the ICE when the extended range is needed.

As mentioned in the study [PFA18] presented in the introduction, it can be noted that the target type of the hybrid sales for light-duty vehicles is the mild/full hybrid.

1.2 The E-TECH powertrain

The E-TECH powertrain is the Renault powertrain studied in this thesis. The concept and issue behind this powertrain is presented in the sequel.

1.2.1 The concept of the powertrain

Among the history of HEV, several designs have occurred. In 1997, Toyota introduced the first HEV, the Toyota Prius uses a planetary gear-based transmission acting as a power split between the ICE and electric motors to propel the car. Honda introduced the Honda Insight [Sit09] in 1999. The Insight uses belt and pulley to make the Continuously Variable Transmission CVT. In 2015, Honda proposed a new type of hybrid transmission: the dual clutch drive with the Honda Fit [HON]. The 2011 Chevrolet Volt with the 2011 Opel Ampera are presented to be first extended-range hybrid vehicles [ME14]. In the HEV market, Toyota is the clear leader based on volume sales of the models with it "synergy drive system". With brisk market acceptance and success of the Prius, HEV technology has shown its maturity and potential.

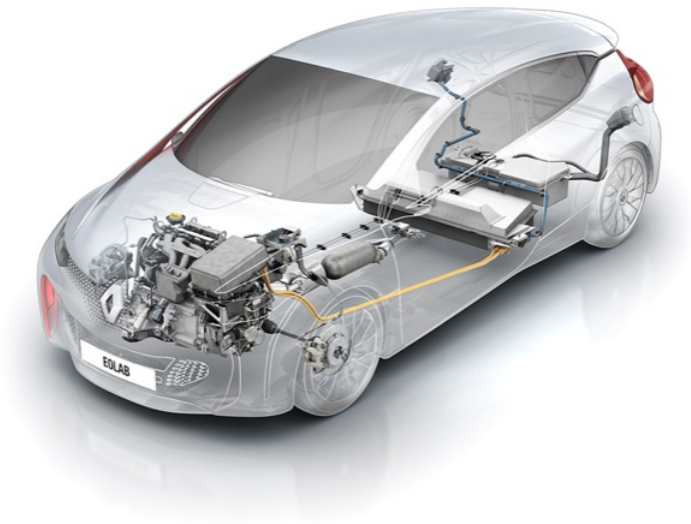

Figure 1.3 – A concept car the Renault EOLAB 2014

But to create a more attractive HEV, a new concept for improving the HEV powertrain is born at Renault. The concept uses a dedicated hybrid transmission made possible with the development of robust control systems. The new powertrain has demonstrated great interest in the concept car the EOLAB in 2014 (see figure 1.3). First call the locodiscobox in the EOLAB, the powertrain has been recalled the E-TECH for his enter in the marker

at the beginning of 2020. The target size of the E-TECH powertrain has been declined in full and plug-in hybrid by adapting the size of the battery.

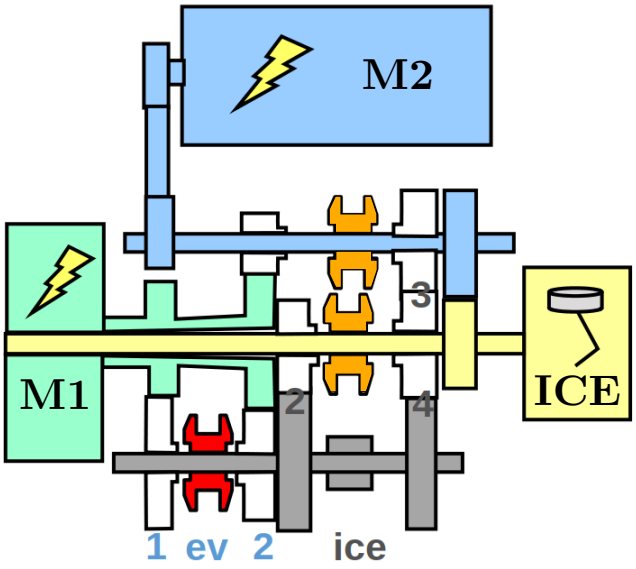

Figure 1.4 – The E-TECH powertrain

The E-TECH powertrain, seen in figure 1.4, utilized the combination of an ICE (in yellow) coupled with a high voltage alternator (in blue call the M2) and an electric motor (in green call the M1) to propel the car. The gearbox is designed to connect the ICE and the M1 motor independently of each other to the wheel (gray shaft in figure 1.4). Indeed, the gearbox allows to connect the M1 to the wheel through two different gear-ratio. In figure 1.4, the red selector can be shifted to the left to engage the first gear and to the right to engage the second gear. The gearbox also allows to connect the coupled ICE-M2 to the wheel through three different gear-ratio. Noted ICE 2,3 and 4 in figure 1.4, two orange selectors permits to select between the three ICE gear-ratio. In order to fit the powertrain into the light-duty car, the tradeoff has been to remove the clutch and the mechanical synchronization found in classical gearbox. And replaced the missing part by developing a control software able to synchronize the shafts speed during gears shifting and supervise the traction of the car.

Through the dedicated transmission, Renault has developed the E-TECH HEV to be serial-parallel hybrid. At low speed (inferior to 20km/h) or between ICE gear shifts, the powertrain is constrained to work in the serial mode and the powertrain can work in parallel mode the rest of the time.

1.2.2 The disconnected battery context

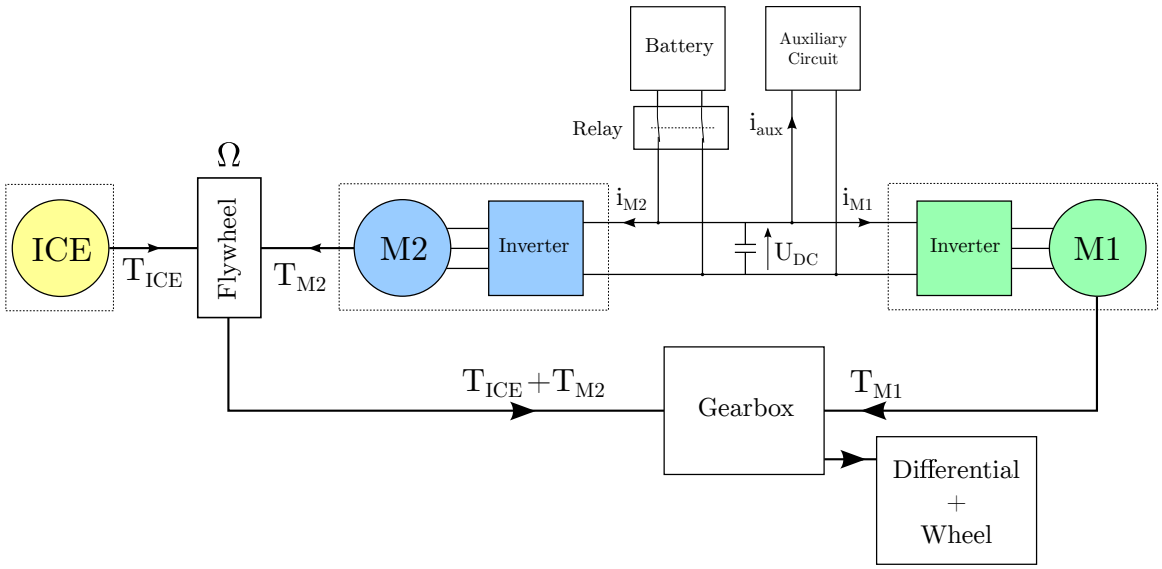

Figure 1.5 – Architecture of the system

The electrical connection between the inverter, the battery and the auxiliary circuit are shown in figure 1.5. The M1 and M2 are both Permanent Magnet Synchronous Motors (PMSM). Two inverters are in charge to convert the electric power from alternative to constant current and vice versa. The inverter shares the electrical power through a DC bus with one capacitor. The battery is connected to the DC bus with a relay. The auxiliary circuit is connected to the DC bus through a DC/DC converter. It step down the voltage to power the 12V battery, the control unit, assisted steering, the light, the air conditioning and other auxiliary system found on the car.

In the event of the high-voltage battery disconnection, the battery relay open and the system is affected differently in serial or parallel mode. As explained before, the serial mode and parallel mode can be used by powertrain, but one of this mode is more advanced than the other.

In the serial mode, the power goes from the ICE to the M1 driving the wheel. The ICE produces mechanical power by burning the fuel, the M2 converts this power into electrical power and the M1 used this power to tract the vehicle. The ICE is connected to the M2 through a flywheel. This flywheel acts like a mechanical energy storage. The M2 is connected to the M1 via a DC bus. On a normal hybrid vehicle, the battery is connected to this DC bus and acts like an energy storage. However, here without the battery, the

only electrical storage is the capacitor present between M2 and M1. The flywheel and the capacitor are the only storage able to maintain the power transmission from the ICE to the wheel. In this configuration, the control requires to maintain two quantities: the voltage of the DC bus and the rotational speed of the flywheel.

In the parallel mode, the ICE can be connected to the wheel for propelling the vehicle, the M1 is turn off because the disconnected battery doesn't add any power. The M2 is utilized to maintain the DC bus for supplying the energy to the auxiliary circuit. Only the DC bus control is needed from the development of the serial mode, placing the serial mode has the more advance mode. Moreover, before going in parallel mode, the serial mode is needed for starting the vehicle from 0 to 20km/h.

Thus, the serial mode is the critical mode and it has been the selected mode for this study. In the sequel, the battery disconnection problem is detailed.

1.3 The serial mode without the battery: objectives, time scales and technical difficulties

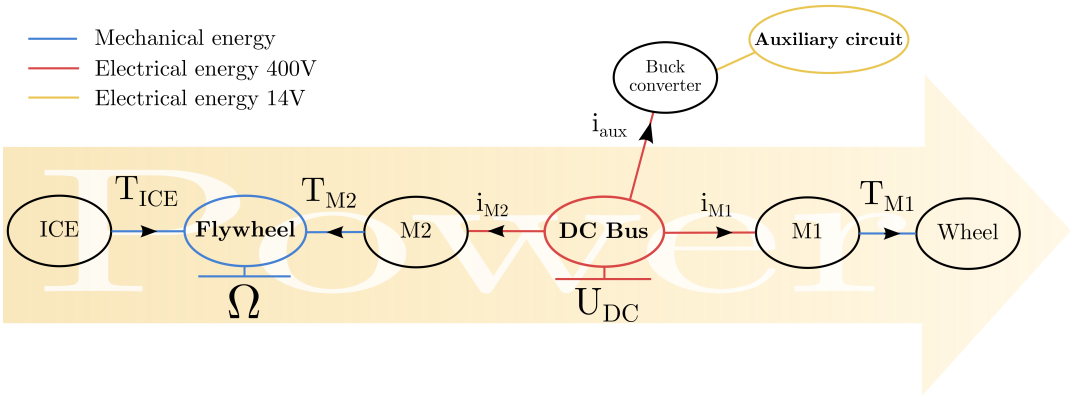

Figure 1.6 – Transmission of the power from the Internal Combustion Engine (ICE) to the wheels

In this section, the objectives, time scales and difficulties encounter in the serial mode without the battery are presented. In this mode, see figure 1.6, the power goes from the ICE to the M1 driving the wheel. The system has two energy buffers the flywheel between the ICE and the M2 and the capacitor between the M2 and the M1. Each buffer had the level of energy storage represented by the physical value of the flywheel rotational speed or the capacitor voltage. Note that the auxiliary circuit acts as a disturbance connected

to DC bus. Because the auxiliary circuit can be trigger by the assisted steering, the light or the air conditioning unit, it is supposed to be unknown.

1.3.1 Objectives

Our global objective is to do the best to realize the driver demand, it is here the accelerator pedal and has to somehow correspond to the M1 torque. The driver is suspected to encounter discomfort, if the powertrain reacts with a slow variation of the output torque and large delay. For the acceptance of the serial mode without battery, the goal is to provide an Electrical Vehicle EV feeling or at least an ICE feeling. The EV feeling corresponding at a time-respond around 100-150ms and an ICE feeling is around 150ms-300ms. Thus, another objective of the thesis is to propose a strategy able to produce an EV/ICE feeling without the battery connected. Before encountering the user feeling, the primary objective is to overcome the battery failure and known if the powertrain can be drive without it.

For achieving the power transmission from the ICE to the wheels, the following control objectives must be carried out:

— the current of the electric motors,

— the voltage control of the DC bus,

— the rotational speed control of the flywheel.

The two first control objectives have to deal with the voltage control of the DC bus and the possibility to maintain the voltage under the disturbance caused by the auxiliary circuit. The second objective is realized by proposing strategies to control the rotational speed with a multi input/output system.

1.3.2 Input-output of the system

The control law developed in this thesis will be implemented in the inverter control units. The software in this control unit has direct access to the inverter signals. It controls the IGBT through PWM signals, measures the current and position of the motors. The software can run and access all inverters signals at 10kHz. The software communicates the ICE torque demand to the engine control unit through can bus protocol at 100Hz.

When the current controls of the inverters are made, the M1 and the M2 can receive a current or torque reference and the input-output of the powertrain are:

— T^*_{ICE} for the ICE torque reference,

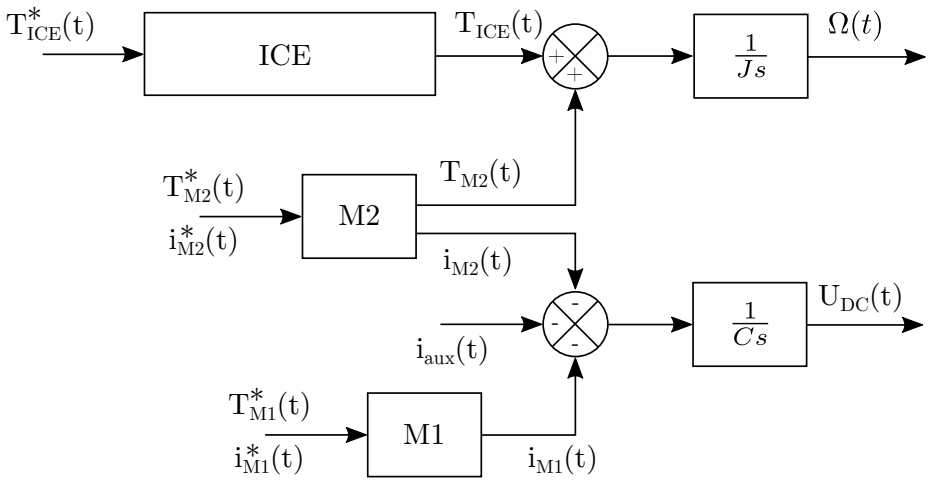

Figure 1.7 – Diagram of the input-output of the powertrain

— T^*_{M2} or i^*_{M2} for the M2 torque or current reference,
— T^*_{M1} or i^*_{M1} for the M1 torque or current reference,
— U_{DC} the DC bus voltage,
— Ω the rotational speed of the flywheel.

Note that the system shown on figure 1.7 correspond to the beginning of chapter 3.

1.3.3 Time scale decomposition of the HEV

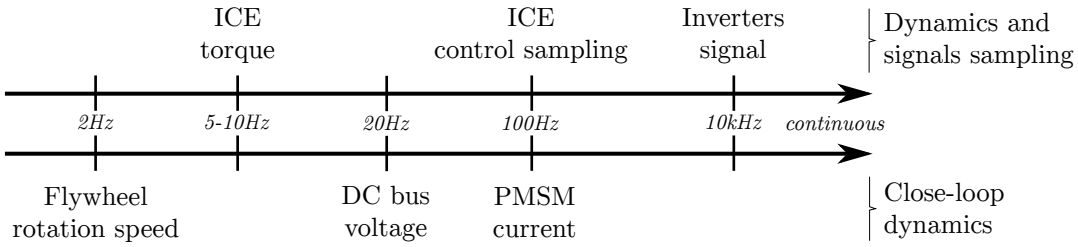

Figure 1.8 – Time scale of each part of the serial hybrid vehicle

The dynamics of the powertrain are divided in three time scales. The small time scale being the fast dynamic and the larger one representing the slow dynamic. The small time scale is the current of the M1 and the M2, the medium time scale is the voltage of the DC bus and the larger one is the rotational speed of the flywheel between the ICE and the M2. The different time scale and control signal frequency are shown in figure 1.8. The three control objectives can be retrieved on the lower part of figure 1.8 with an idea of the

bandwidth associates with each other. On the upper portion of figure 1.8, the sampling frequency of the ICE torque demand and the inverters signals (measurement and control) can be seen with the given dynamics of the ICE torque.

The challenge for the closed loop controls is then to distribute each bandwidth according to their sub stage and upper stage.

1.3.4 Technical difficulties

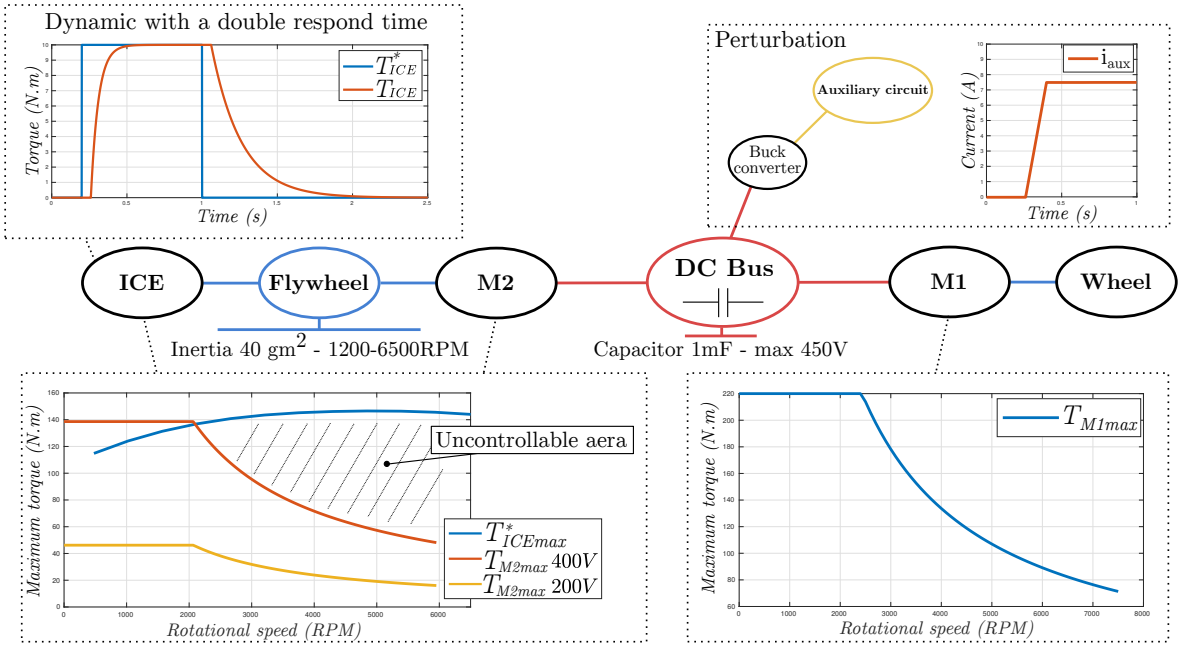

Figure 1.9 – Usage domain and constraint for the serial hybrid vehicle

For the current of each electric motor, the control has to be robust regardless of the uncertainties, the non-linearity of the motor and the non-linearity of the inverters. The overall current dynamic has to be fast enough for the upper stage: the regulation of the DC bus voltage. For the the DC bus voltage, the control has to provide a fine regulation of the voltage with the bandwidth of the current control or the DC bus won't be able to transmit the energy. For the rotational speed of the flywheel, the control has the same objectives as for the voltage control. It has to regulate the rotational speed or the power transmission will collapse.

Moreover, working with an ICE introduces the complexity of implanting precise torque control with an engine involving chemical transformation. Nevertheless, the torque control

of the electrical motor is a topic mastered from long time. In our case, the system is such that the precision of the ICE control is enough to fit the purpose but involves a prediction scheme.

This thesis has been decomposed from the smaller time scale to the higher time scale of the control behind the serial hybrid vehicle. Thus, the next chapter introduces the smaller scale that is electrical part of the thesis, where the key is to control the DC bus voltage.

Chapter 2

Control of the DC Bus Voltage

2.1 Introduction

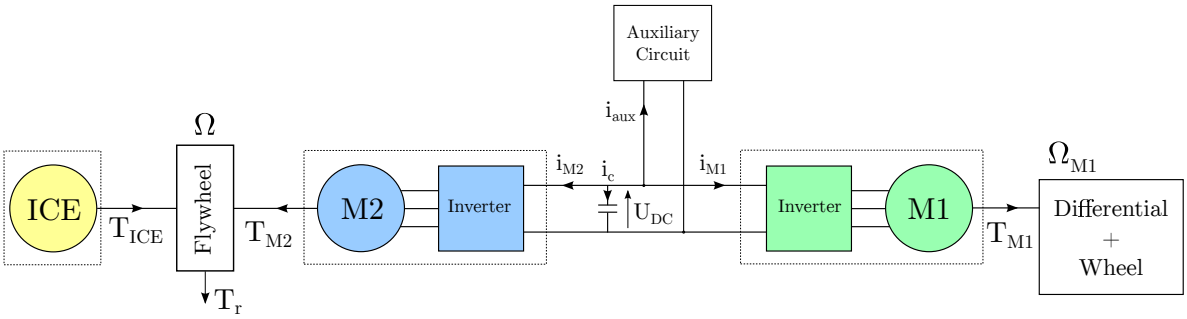

Figure 2.1 – Transmission of the power from the Internal Combustion Engine (ICE) to the Wheel

This chapter introduces the control of the DC bus voltage. On serial hybrid vehicle figure 2.1, the DC bus voltage is a key part without the battery connected. Limited by the hardware constraint, if the voltage goes to high major failure can occur and irreversible damage can happen. If the voltage drops to low, the DC bus cannot transmit the power from one Permanent Magnet Synchronous Motors (PMSM) to the other.

For studying the feasibility of the voltage control of the DC bus, different topic has to be mastered. The first topic is the modeling. The physical law involves inside the PMSM [Chi05] can draw under some assumptions a simplified and representative model of the machine [AD05] and [MAC18]. Inspired by [Jan11], two modeling of the inverters are needed. An average model for large time scale simulation and the designing of the current control is made. A second inverters modeling call the switching model for small time scale simulation and the robustness of the DC bus voltage control is also made. The second topic is the optimization of the current references of the PMSM. The thesis of [Sep17] presents different strategies and proposes algorithms to solve this problem. Lastly, the control is designed as [RET08] and [Kot12].

This chapter is developed around the M2 maintaining the DC bus voltage. Nevertheless, the same methodology can be used with the M1 maintaining the DC bus voltage. In our case, it only implies changing the parameter from one PMSM to the other and this will be used in the next chapter around other strategies.

In the following, the modeling aspect of each electrical part is approached. The current control is detailed and the offline optimization is shown. The simulation result are studied on the nominal case and after with the switching model of the inverters.

2.2 Electrical modeling

In this section, the electrical system is divided into several pieces, which are: the PMSM, the inverter and the DC bus. The organization of the electric parts is shown on the next section. Then, the PMSM characteristic and modeling are introduced, the inverter non-linearity is presented and the DC bus modeling is given.

2.2.1 Architecture of the electrical parts

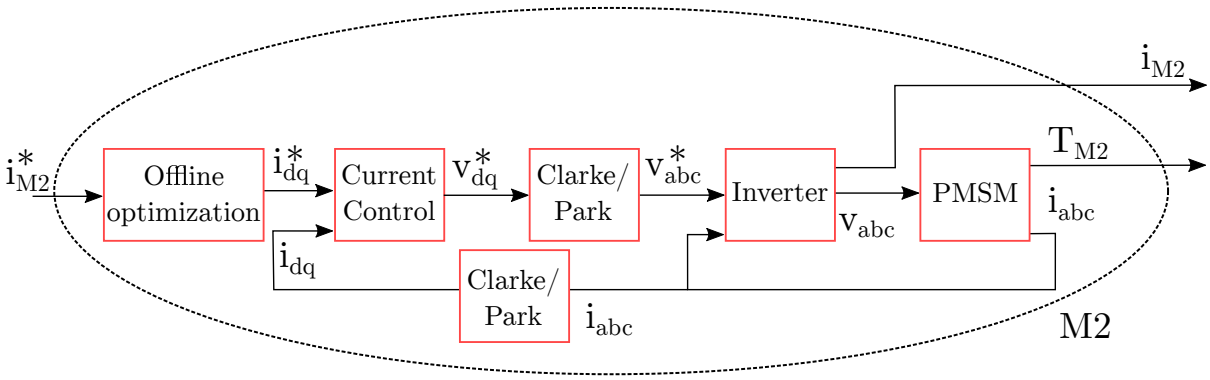

Figure 2.2 – Architecture of the electrical subsystem

In order to be integrated in the DC bus voltage control, the electrical system M2 is decomposed in different part, see figure 2.2. From the outer loop, the system can receive a torque or a DC current reference and output torque on PMSM shaft and current on the DC bus. From the inner loop, the PMSM react to the voltages impose by the inverter to produce currents. Theses currents are measured and transmit to the current control responsible to create the duty-cycle that control the inverter. Moreover an offline optimization dictated the AC current reference, send to the current control, that minimize

the joule heating and respect the DC current or torque reference.

2.2.2 PMSM characteristics

In variable speed application, Alternative Current (AC) motor has been competing with Direct Current (DC) motor. But, where DC motor are much simple to control, AC motor come with the mechanical benefit that they are brushless [YPK14] and thus don't necessitate all the maintenance of DC motor. PMSM are part of AC motor and are widely used across industrial and home application. Against asynchronous motor, the other type of AC motor, the synchronous motor have higher efficiency than asynchronous motor [XCC08], they also have high energy density but come with the disadvantageous to be dependent on angular sensor.

The first two letters of PMSM stand for the rotor of the motor being a Permanent Magnet and it is opposed to excited rotor, where the rotor is producing magnetic flux with an electrical winding. Also Synchronous comes with the rotor turning at the same speed than the magnetic rotating field created by the stator winding. In this thesis, the PMSM type is reduced to internal permanent magnet, i.e. the rotor is covered by magnet and inside the stator. But the model presented here can be easily extended to external magnet.

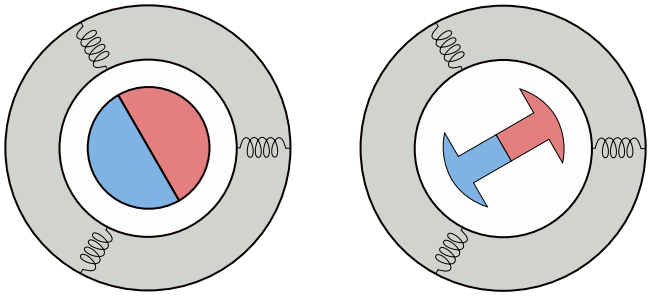

Figure 2.3 – Smooth and salient poles

Depending on the magnet arrangement, see figure 2.3, two types of machine can be seen: smooth and salient poles. The smooth poles implies some simplification in the PMSM model: the inductance L_d and L_q presented in the dynamic model 2.6 are equal, simplifying the optimization problem on the section 2.4. The M1 and M2 studied in this thesis are salient poles, as it can be seen in the table 2, $L_d \neq L_q$ for both motors. But, the PMSM used in the experimentation chapter has smooth poles.

2.2.3 PMSM modeling

The physics of the PMSM involves different fields: electrical, magnetic, mechanical, thermal and others. In the context of torque and current control, only electromagnetic and electromechanical phenomena are relevant [Mes19] for the modeling. Maxwell's equations, Laplace's force and Newton's second law describe this phenomena [Chi05; AD05] and under some assumptions permit to get a simplified and representative model of the machine.

Assumption 1 (PMSM modeling assumptions)

- *The magnetic saturation is neglected,*
- *The magnetomotive force is supposed to be sinusoidal,*
- *Temperature effect, hysteresis phenomena, skin effect and the Foucault's current of the machine are neglected,*
- *The damping effect of the rotor is neglected.*

With these assumptions, the equations applied to the PMSM describe a model depending on the rotor position. Thus, the model obtained lead to difficulty to design the controller and the Clarke and Park transformations will be used in the sequel to design a simpler controller.

Model in the stator axis

See figure 2.4, on the left, the PMSM is represented with one magnetic pair of poles. The magnetic field generated by the rotor is aligned on the d axis. The PMSM have three winding, each one along a, b and c axis. In this representation, each a, b and c axis are separated by 120° and d, q axis by 90°. The electric angle θ is measured from the a axis to the d axis. On the right of figure 2.4, the PMSM is represented with two pair of magnetic poles: six winding and the rotor also has two magnetic poles. The electric angle θ on this case is such that $\theta = \theta_m\, p$, where p is the pair of poles and θ_m represents the mechanical angle of the shaft. In this way, the PMSM can be modeled in the electric axis with $p = 1 \,\text{or}\, 2$ and the model can be extended to any p pairs of magnetic poles. Note that, the difference of the PMSM pair of poles is represented here by multiplying the number of winding, but it also can be illustrated by changing the number of magnetic poles on the rotor.

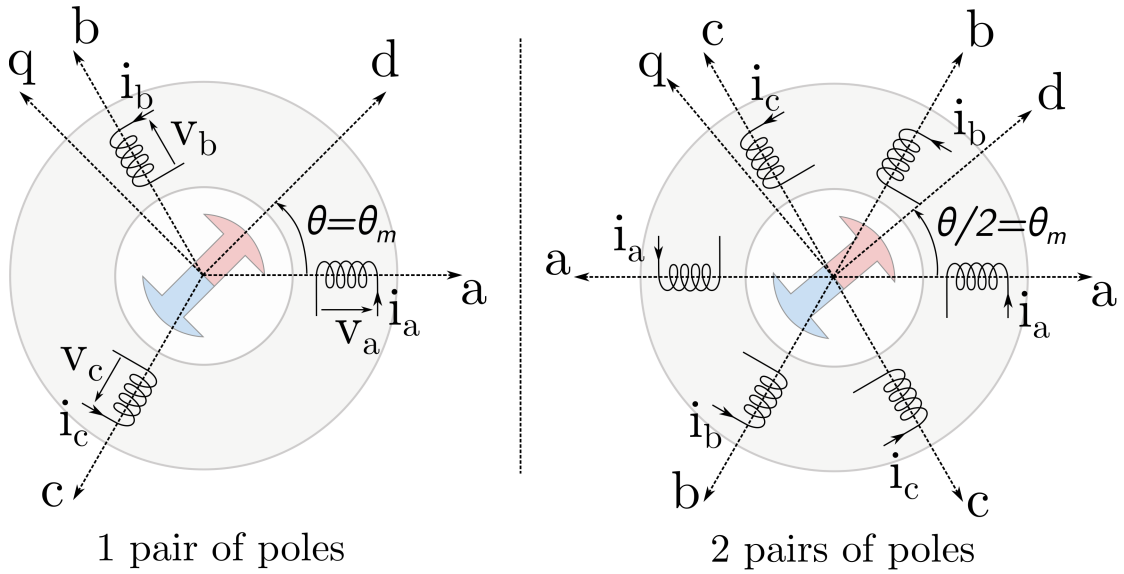

Figure 2.4 – abc axis and dq axis

In the stator axis [AD05] and [MAC18], the voltage-flux model is:

$$\begin{bmatrix} v_a \\ v_b \\ v_c \end{bmatrix} = R_s \begin{bmatrix} i_a \\ i_b \\ i_c \end{bmatrix} + \frac{d}{dt} \begin{bmatrix} \Psi_a \\ \Psi_b \\ \Psi_c \end{bmatrix} \tag{2.1}$$

where $[v_a,\ v_b,\ v_c]^T$ are the stator voltage, R_s is the stator resistance, $[i_a,\ i_b,\ i_c]^T$ are the stator current and $[\Psi_a,\ \Psi_b,\ \Psi_c]^T$ the stator fluxes.

The stator fluxes can be expressed as:

$$\begin{bmatrix} \Psi_a \\ \Psi_b \\ \Psi_c \end{bmatrix} = L_s \begin{bmatrix} i_a \\ i_b \\ i_c \end{bmatrix} + \Psi_f \begin{bmatrix} cos(\theta) \\ cos(\theta - 2\pi/3) \\ cos(\theta - 4\pi/3) \end{bmatrix} \tag{2.2}$$

where Ψ_f is the flux generated by the permanent magnet and L_s is the inductance. In the general case of the salient poles, the statoric inductance L_s is formed by the variable

term:

$$L_s = \begin{bmatrix} L_{s0} & M_{s0} & M_{s0} \\ M_{s0} & L_{s0} & M_{s0} \\ M_{s0} & M_{s0} & L_{s0} \end{bmatrix} + L_{s2} \begin{bmatrix} cos(2\theta) & cos(2\theta - 2\pi/3) & cos(2\theta + 2\pi/3) \\ cos(2\theta - 2\pi/3) & cos(2\theta + 2\pi/3) & cos(2\theta) \\ cos(2\theta + 2\pi/3) & cos(2\theta) & cos(2\theta - 2\pi/3) \end{bmatrix} \tag{2.3}$$

with L_{s0}, L_{s2} and M_{s0} being the self and mutual inductance.

Clarke and Park transformations

The Clarke and Park transformations consist of the following matrix:

$$\begin{bmatrix} x_a \\ x_b \\ x_c \end{bmatrix} = P(\theta) \begin{bmatrix} x_d \\ x_q \end{bmatrix} \tag{2.4}$$

where

$$P(\theta) = \begin{bmatrix} cos(\theta) & -sin(\theta) \\ cos(\theta - \frac{2\pi}{3}) & -sin(\theta - \frac{2\pi}{3}) \\ cos(\theta + \frac{2\pi}{3}) & -sin(\theta + \frac{2\pi}{3}) \end{bmatrix} \tag{2.5}$$

Model in the dq axis

From the previous PMSM model (see (2.1) and (2.2)), the design of the control of the motor is not clever. The PMSM model expressed in the (a, b, c) frame has to be transferred in the rotating frame (d, q) using the Park and Clarke transformations. Using the transformation (2.4) on the model (2.1), the following PMSM model is obtained:

$$\begin{aligned} v_d &= R_s i_d + L_d \dot{i}_d - \omega_r L_q i_q \\ v_q &= R_s i_q + L_q \dot{i}_q + \omega_r L_d i_d + \omega_r \Phi_f \end{aligned} \tag{2.6}$$

where

$$\begin{aligned} L_d &= L_{s0} + \tfrac{3}{2} L_{s2} - M_0 \\ L_q &= L_{s0} - \tfrac{3}{2} L_{s2} - M_0 \\ \Phi_f &= \sqrt{\tfrac{3}{2}} \Psi_f \end{aligned} \tag{2.7}$$

Note that, ω_r is the rotational speed of the magnetic field. It is linked to the rotational

speed Ω_{M2} of the shaft by the number of pair poles p as:

$$\omega_r = p\,\Omega_{M2} \tag{2.8}$$

Electromagnetic torque

The electromagnetic torque T_{EM} is created by the interaction of the permanent magnets and the magnetic flux induced by the current in the stator winding. Thus, the produced torque is applied to the shaft output such that:

$$T_{EM} = p\tfrac{3}{2}(\Phi_f + (L_d - L_q)i_d)i_q \tag{2.9}$$

Mechanical connection of the PMSM

The two motors M1 and M2 are connected differently to the system. The M1 is connected directly to the differential system. The M2 is connected using a gear ratio R_{M2} between the shaft of the motor and the flywheel.

Thus, the following relations between the M2 shaft and the flywheel output exist such that:

$$\begin{aligned} \Omega_{M2} &= R_{M2}\,\Omega \\ T_{M2} &= R_{M2}\,T_{EM2} \end{aligned} \tag{2.10}$$

where Ω is the rotational speed of the ICE shaft, Ω_{M2} the rotational speed of the M2 shaft and T_{M2} the output torque of the M2 motors applied to the ICE shaft.

The electromagnetic torque T_{EM1} is the output torque of the M1:

$$T_{M1} = T_{EM1} \tag{2.11}$$

2.2.4 Inverter Model

The inverter is in charge to convert the constant voltage of the DC bus into an alternative voltage for the PMSM. It uses six Insulated Gate Bipolar Transistor (IGBT) each one paired with a diode to execute the conversion. Inspired by [Jan11], two modeling are developed:

— an average model for large time scale simulation and designing the current control,
— a switching model for small time scale simulation and testing the robustness of the DC bus voltage control.

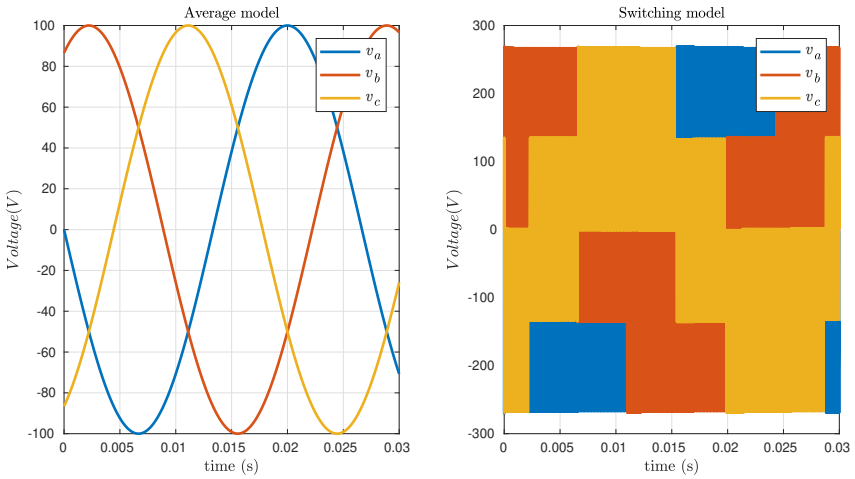

Figure 2.5 – Illustration of the average model and the switching model

See figure 2.5, the average model doesn't show the commutation of the IGBT, the output of the average model looks sinusoidal. On the other end, the switching model takes into account the commutation of the IGBT and permits to visualize the high frequencies.

Average model

The average model is an ideal model where the inverter is represented by a unite gain, see (2.12). This model is utilized for the design of the current control of the PMSM and voltage control of the DC bus, also for a larger time scale dynamic that is the control of the ICE speed.

$$\begin{bmatrix} v_a \\ v_b \\ v_c \end{bmatrix} = \begin{bmatrix} v_a^* \\ v_b^* \\ v_c^* \end{bmatrix} \tag{2.12}$$

where $[v_a, v_b, v_c]^T$ are the stator voltage of the PMSM and $[v_a^*, v_b^*, v_c^*]^T$ are the voltage reference.

Remark 1 *This model does not take into account the voltage or current saturation of the inverter.*

Switching model

The switching model will served for small time scale simulation and testing the robustness of the voltage control. The modeling is divided in three steps from the input signal to the output of the model, see figure 2.6. First of all, the reference voltage is scaled to be the duty-cycle between $[0, 1]$. Using Pulse Width Modulation (PWM) algorithm, the duty-cycle is translated into a binary control signal fixing the IGBT state of the arm. The control signal is compared to the PMSM current to determine if the IGBT or the diode is conductive. Then, the output voltage is found using the model of the IGBT or the diode depending on the current path. The idea of the switching model is to reconstruct the voltage reference, such that the average of the voltage output on one PWM period T_s is equal to the voltage reference. Note that, the model of the IGBT, the diode and the deadtime add an uncertainty to the output voltage.

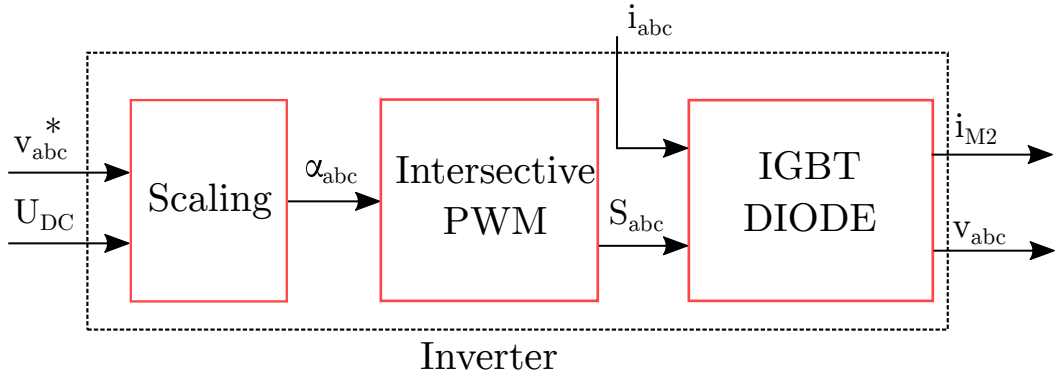

Figure 2.6 – Inverter modeling

Assumption 2 *The IGBT are considered as ideal interrupter and the diode forward voltage V_D is supposed to be constant.*

Moreover, the inverter can be decomposed in three arms, see figure 2.7. Each arm (A, B or C) is individually responsible to create the voltage of each phase. In the sequel, the study will focus on the A arm, but the B and C arm will work on the same matter.

The scaling consist of:

$$\begin{bmatrix} \alpha_a \\ \alpha_b \\ \alpha_c \end{bmatrix} = \frac{1}{U_{DC}} \begin{bmatrix} v_a^* \\ v_b^* \\ v_c^* \end{bmatrix} + \frac{1}{2} \tag{2.13}$$

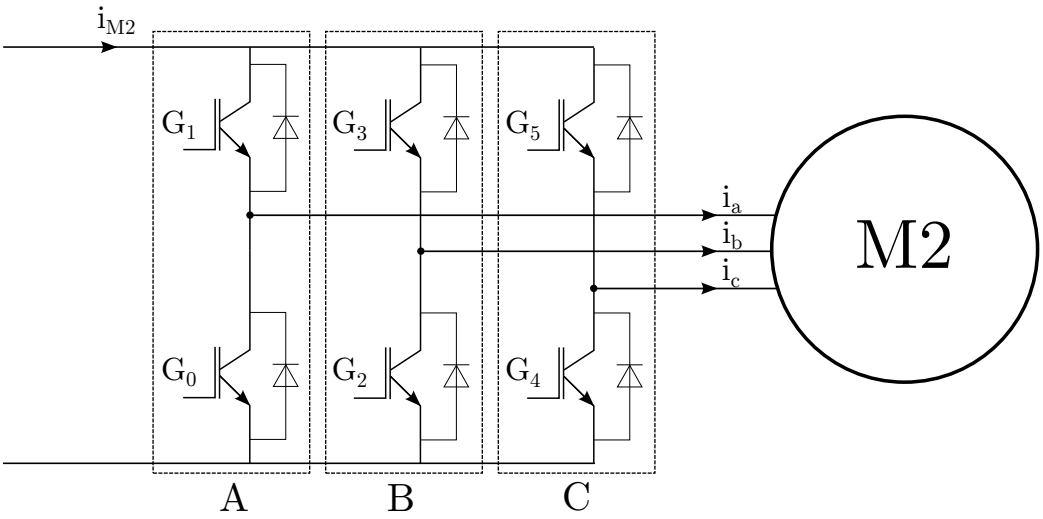

Figure 2.7 – Inverter Scheme

where $[v_a^*, v_b^*, v_c^*]^T$ are the voltage reference, $[\alpha_a, \alpha_b, \alpha_c]^T$ are the duty-cycle and U_{DC} is the DC bus voltage.

The Sinusoidal PWM (or SPWM), originally introduced in [Sch64] and explained in [Bou17], consists of a duty-cycle and a triangular wave, see the illustration in figure 2.8. When the duty-cycle wave α_a is superior to the triangular carrier, the output signal S_a is set to 1, else is set to 0.

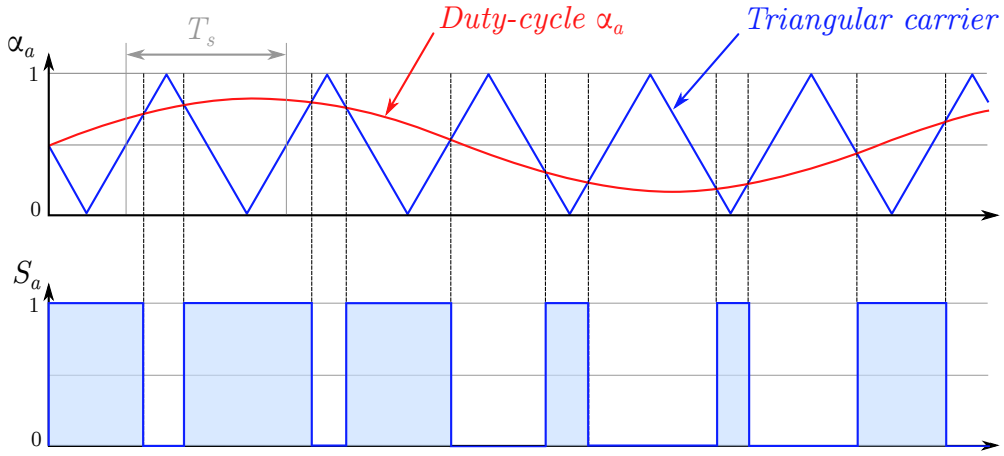

Figure 2.8 – PWM - The intersective method

Each arm use two IGBT and two diodes, see figure 2.9, each IGBT works on a complementary mode:

— when S_a is equal to 1, G_1 is set to be on and G_0 is off,

— when S_a is equal to 0, G_0 is on and G_1 is off.

To avoid any risk of short circuit between the negative and positive side of the DC bus, a deadtime T_D is introduced between each IGBT commutation (see figure 2.9).

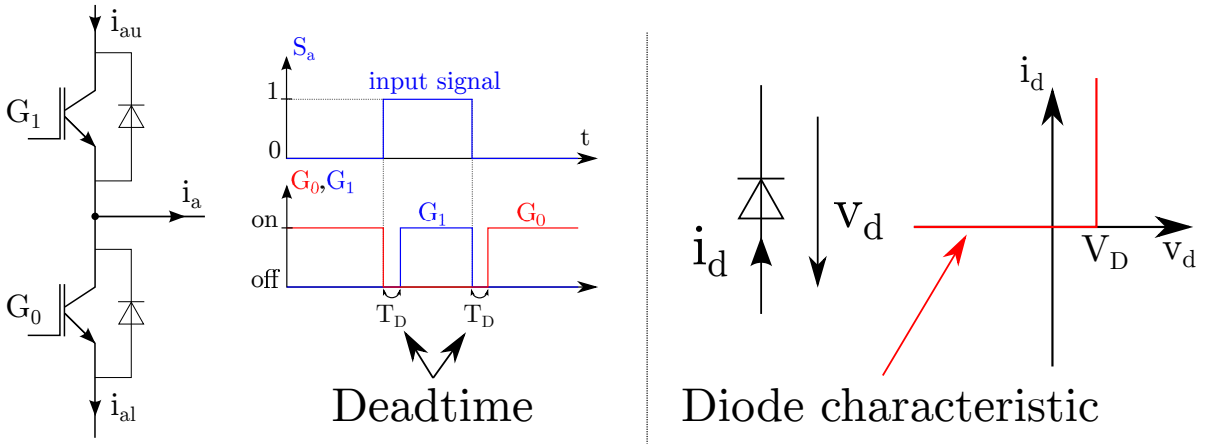

Figure 2.9 – Inverter Scheme with deadtime and diode characteristic

The voltage output and current on each arm is deduced using the following algorithm (see figure 2.10). The algorithm considers the current from the PMSM i_a and the state of the IGBT to determine the current path. Then, using the model of the component the PMSM voltage is established.

if $i_a > 0$ **then**
  if G_1 is off **then**
    $i_{al} = -i_a$ and $v_a = -V_D$
  else
    $i_{au} = i_a$ and $v_a = U_{DC}$
  end if
else
  if G_0 is off **then**
    $i_{au} = i_a$ and $v_a = U_{DC} - V_D$
  else
    $i_{al} = -i_a$ and $v_a = 0$
  end if
end if

Figure 2.10 – Inverter modeling algorithm

Example, if the current $i_a > 0$ and the upper IGBT G_1 is off, the current can only

flow from the lower diode, then the output voltage v_a is equal to the voltage bias of the diode $-V_D$.

Additionally, the DC bus current i_M can be calculated using one of this expression:

$$i_M = i_{au} + i_{bu} + i_{cu} \text{ or } i_M = i_{al} + i_{bl} + i_{cl} \tag{2.14}$$

where i_{au}, i_{bu} and i_{cu} are the upper current in each arm and i_{al}, i_{bl} and i_{cl} are the lower current in each arm. Note that the sum of each current on the upper side of the inverter has to be equal to the sum of the lower side.

Remark 2 *Considering the switching model of the inverter and the scaling, the output voltage is limited to:*

$$\begin{bmatrix} |v_a| \\ |v_b| \\ |v_c| \end{bmatrix} \leq \frac{U_{DC}}{2} \tag{2.15}$$

Remark 3 *This method for modeling and computing the output of the inverter can be utilized with more advance model of each component.*

2.2.5 DC bus Model

The DC bus carry the power from one PMSM to the others subsystem, see figure 2.11. The capacitor was initially used to filter Pulse Width Modulation (PWM) harmonics of the inverter and thus for protecting the battery from them. Here without the battery, this capacitor is a small energy storage. It fixed the DC bus voltage and ensure the energy transfer through the DC link.

Assumption 3 (DC bus modeling assumptions)
The capacitor has a constant capacity and negligible losses.

The voltage dynamic is given by the balance of every current such that:

$$\dot{U}_{DC} = \frac{i_c}{C} = \frac{-i_{M2} - i_{aux} - i_{M1}}{C} \tag{2.16}$$

where C represent the capacity.

Thus, the modeling of each needed electrical part has been given and the next section will presents the current control law.

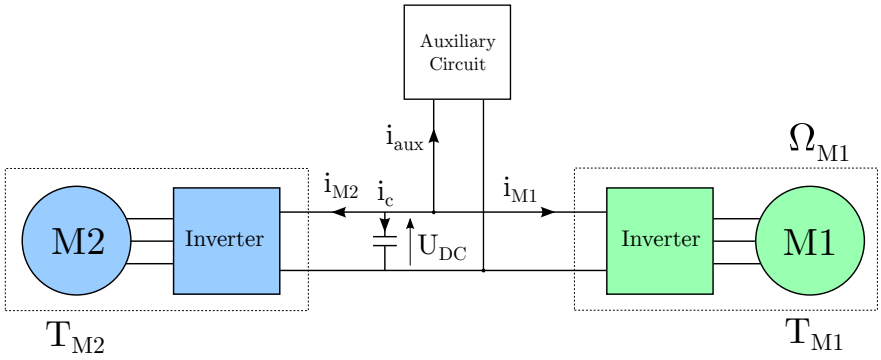

Figure 2.11 – DC bus diagram

2.3 Control of the PMSM current

This section presents the control law involves in the regulation of the PMSM current. The current control is designed using the PMSM model (2.6) and the average model of the inverter (2.12). The average model of the inverter gives the following simplification: the output of the current control $[v_d^*, v_q^*]^T$ is the PMSM voltage $[v_d, v_q]^T$. Thus, the current dynamic is:

$$\begin{aligned} \dot{i}_d &= \frac{v_d^* - R_s i_d + \omega_r L_q i_q}{L_d} \\ \dot{i}_q &= \frac{v_q^* - R_s i_q - \omega_r L_d i_d - \omega_r \Phi_f}{L_q} \end{aligned} \tag{2.17}$$

Two PI control law with the decoupling term are introduced such that:

$$\begin{aligned} v_d^* &= k_{di} \int (i_d^* - i_d) dt + k_{dp}(i_d^* - i_d) - L_q i_q \omega_r \\ v_q^* &= k_{qi} \int (i_q^* - i_q) dt + k_{qp}(i_q^* - i_q) + \omega_r \Phi_f + L_d i_d \omega_r \end{aligned} \tag{2.18}$$

where k_{di} and k_{dp} are the control gain for the d axis and k_{qi} and k_{qp} are the control gain for the q axis.

The control inputs (2.18) being applied to the system (2.17) yields to the closed loop system:

$$\begin{aligned} \dot{i}_d &= \frac{k_{di} \int (i_d^* - i_d) dt + k_{dp}(i_d^* - i_d) - R_s i_d}{L_d} \\ \dot{i}_q &= \frac{k_{qi} \int (i_q^* - i_q) dt + k_{qp}(i_q^* - i_q) - R_s i_q}{L_q} \end{aligned} \tag{2.19}$$

Next, the following variables are introduced as:

$$\begin{aligned} k_{dp} &= 2\xi L_d \omega_c - R_s \\ k_{di} &= L_d \omega_c^2 \\ k_{qp} &= 2\xi L_q \omega_c - R_s \\ k_{qi} &= L_q \omega_c^2 \end{aligned} \tag{2.20}$$

where ω_c and ξ are the tuning parameter.

The system (2.19) can be rewritten as follows:

$$\begin{aligned} \dot{i}_d &= \omega_c^2 \int (i_d^* - i_d)dt + 2\xi\omega_c(i_d^* - i_d) - \frac{R_s}{L_d} i_d^* \\ \dot{i}_q &= \omega_c^2 \int (i_q^* - i_q)dt + 2\xi\omega_c(i_q^* - i_q) - \frac{R_s}{L_q} i_q \end{aligned} \tag{2.21}$$

Using the Laplace domain s, the system (2.21) becomes:

$$\begin{aligned} \frac{i_d}{i_d^*} &= \frac{(2\xi\omega_c - \frac{R_s}{L_d})s + \omega_c^2}{s^2 + 2\xi\omega_c s + \omega_c^2} \\ \frac{i_q}{i_q^*} &= \frac{(2\xi\omega_c - \frac{R_s}{L_q})s + \omega_c^2}{s^2 + 2\xi\omega_c s + \omega_c^2} \end{aligned} \tag{2.22}$$

In this form, the denominator of each fraction (2.22) can be related to a second order system, where ξ is the damping factor and ω_c the time constant. The thesis [Car10] and [Err10] propose more detail on the linearization and the tuning process.

Figure 2.12 presents an illustration of the respond time with the parameter of the M2. The simulation is run with $\xi = 1$, $\omega_c = 628\,rad/s$, $U_{DC} = 400V$ and $\Omega_{M2} = 5000\,RPM$. The simulation is made with the average model of the inverter. At the time t_0, t_1 and t_2, the simulation shows the coupling between the current i_q and i_d.

After designing the current law, the next section presents optimization method used to provide the current references i_d^*, i_q^*.

2.4 Offline optimization of the currents references

In this section, the goal is to fix the current reference i_d^* and i_q^* to realize a torque demand or in case of the voltage regulation, the current demand i_{M2}^*. Indeed, it exist

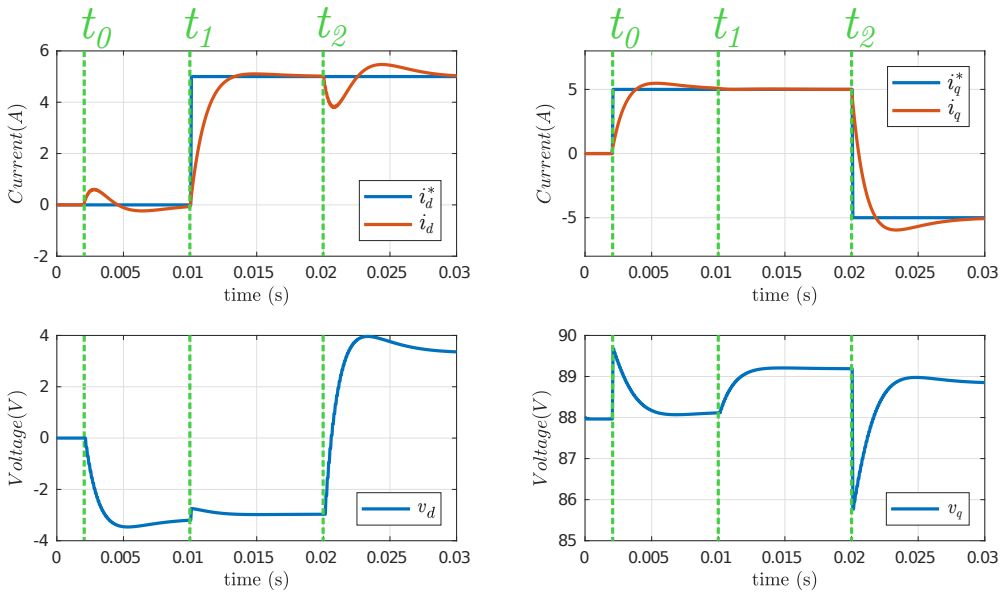

Figure 2.12 – Simulation of the current control at $U_{DC} = 400V$, $\Omega_{M2} = 5000\,RPM$, $\xi = 1$ and $\omega_c = 628\,rad/s$

number combination of i_d^* and i_q^* to realize one demand, but it exists some combination that minimizes the energy losses, maximize the rotational speed or the torque per volt. The author [Sep17] presents different strategies and proposes algorithms to solve the problem.

In this thesis, the current optimization is formulated as:

$$min \quad J = \frac{3}{2}R_s(i_d^{*2} + i_q^{*2}) \tag{2.23}$$

Subject to:

$$\begin{gathered} \frac{p\frac{3}{2}(\Phi_f + (L_d - L_q)i_d^*)i_q^*\Omega_M + \frac{3}{2}R_s(i_d^{*2} + i_q^{*2})}{U_{dc}} - i_{M2}^* = 0 \\ \sqrt{v_d^2 + v_q^2} - U_{DC}/2 < 0 \\ \sqrt{i_d^{*2} + i_q^{*2}} - i_{max} < 0 \end{gathered} \tag{2.24}$$

where i_d^* and i_q^* are the variable, J represents the cost function, it is the resistive losses in the PMSM. The first constraint represents the realization of the current reference, the second the saturation of the inverter voltage and last the current limit i_{max} of the inverter. To resolve the problem, the test domain is discretized on a 3d table, where the input are the voltage of the DC Bus, the current demand and the rotational speed $(U_{DC}, i_{M2}, \Omega_{M2})$. A numerical method, fmincon from matlab, is called on each point to get the combination

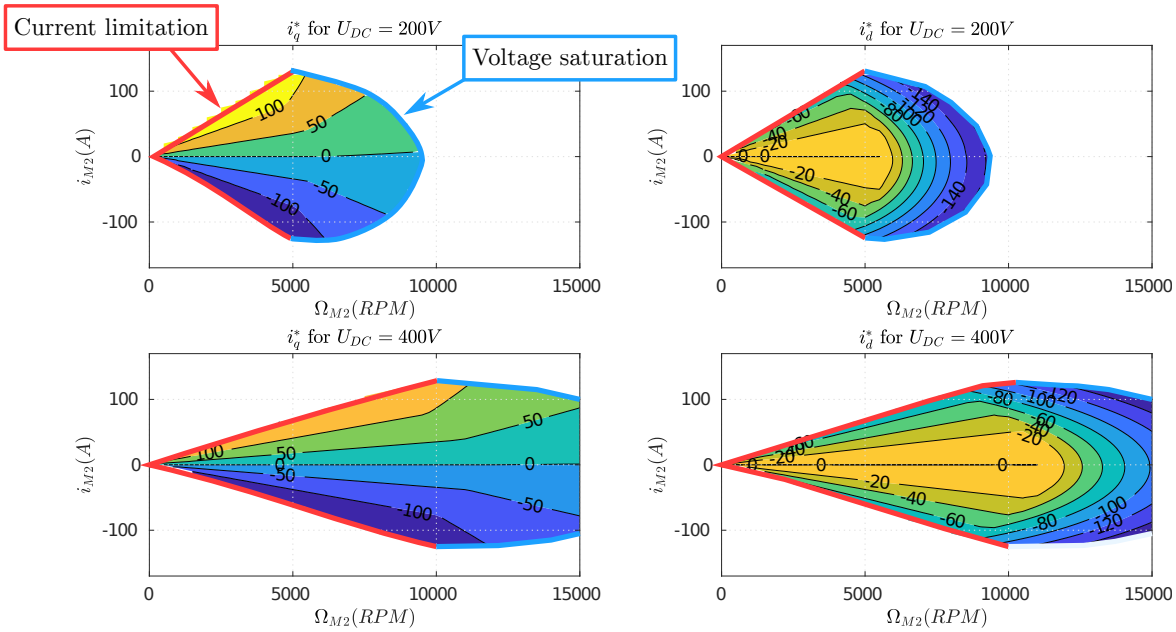

Figure 2.13 – Example of the optimization applied to the PMSM $M2$ with on the top the i_q^* and i_d^* for every i_{M2} demand at $U_{DC} = 200V$ and from $\Omega_{M2} = 0RPM$ to $15000RPM$, same on the bottom except the DC Bus voltage at $400V$

(i_d^*, i_q^*) that minimize the resistive losses on this point.

In figure 2.13, an example of the optimization is shown on the PMSM $M2$ using two different voltages. On the top-left, the currents references i_q^* can be picked for a voltage $U_{DC} = 200V$ and a given (i_{M2}, Ω_{M2}) point. In this part of the figure, the current limitation is shown by the red border and the voltage saturation by the blue border. When the top-left is compare of the bottom-left part of the figure, the limitation of the PWM strategies can be retrieved by the voltage saturation going to higher rotational speed when the DC bus voltage goes higher, from $U_{DC} = 200V$ on the top to $U_{DC} = 400V$ on the bottom. Note that, the same goes from i_d^* on the right part of the figure.

2.5 Voltage control of the DC Bus

On this section, the voltage control of the DC Bus is presented and consist of a PI controller taking the voltage reference U_{DC}^* and the voltage U_{DC} to produce the current demand i_{M2}^*. After the "testing" condition is depicted and a simulation is shown with the ideal inverter model.

2.5.1 Control design

The voltage control is a PI controller that stabilizes the DC bus voltage U_{DC} at the reference level U^*_{DC} :

$$i^*_{M2} = -C(\dot{U}^*_{DC} + \lambda_1(U^*_{DC} - U_{DC}) + \lambda_0 \int (U^*_{DC} - U_{DC})dt) \tag{2.25}$$

where λ_0 and λ_1 are the control gain and C the DC Bus capacitor.

2.5.2 Application of the voltage control

In the following test, see figure 2.14, it has been decided that the goal is to ensure that the DC bus Voltage kept on a desired range when a perturbation occur:

$$|U^*_{DC} - U_{DC}| \leq 10V \tag{2.26}$$

With the following conditions:

— the perturbation demand i_{aux} is unknown and rise from $0A$ to $7.5A$ in $100ms$,
— the closed-loop bandwidth of the PMSM current is around $100Hz$,
— the voltage control is run at $10kHz$,
— the PWM period is $0.1ms$.

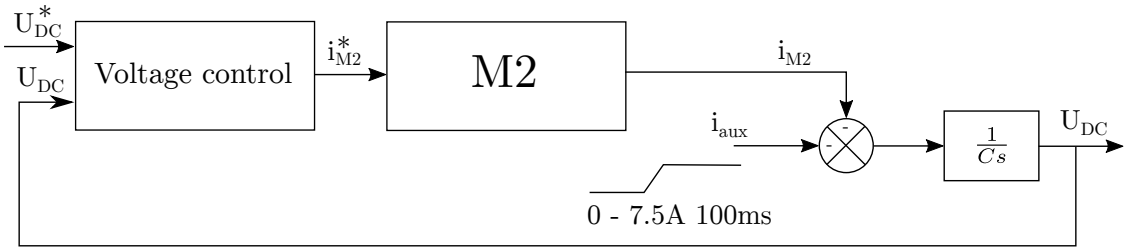

Figure 2.14 – Control design with the goal to maintain U_{DC}

Figure 2.15 shows the result with a constant rotational speed at $\Omega_{M2} = 5000\,RPM$, the tuning gain $\omega_c = 628\,rad/s$, $\xi = 0.7$, $\lambda_0 = 128$ and $\lambda_1 = 8200$. It can be seen that the voltage is kept above $390V$ when the perturbation occur at $0.05s$. Also to realize the current demand $i^*_{m2} = 7.5A$, the i^*_q and the i^*_d are moving accordingly to the current optimization figure 2.13 and the result is $i_{M2} \approx i^*_{M2}$.

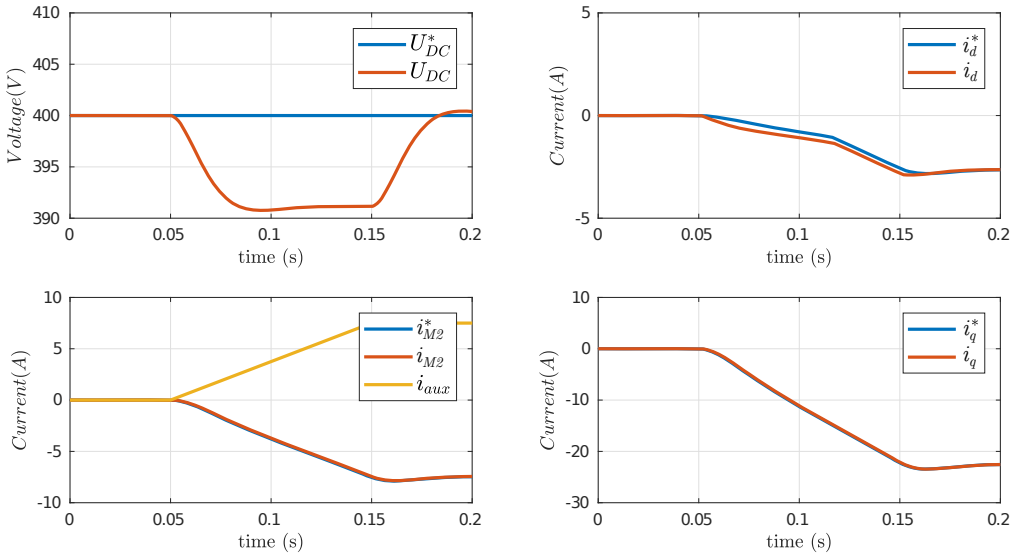

Figure 2.15 – Voltage control with the average model of the inverter

2.5.3 Robustness control with the inverter switching model

Introducing the switching model in the simulation can perturb the voltage tracking. It affects the control by adding a perturbation between the voltage reference of the current control and the voltage input of the PMSM. For the comparison, see figure 2.16, where the parameter from the last simulation is reused with the average model of the inverter (present on the left part of the figure) and the switching model (present on the right part of the figure). The comparison show oscillation on the current i_{M2} produced by the M2 resulting on oscillation on the DC bus voltage U_{DC}. Nevertheless, the voltage stays under control and the condition (2.26) is respected.

In figure 2.17, the simulation is run with the switching model of the inverter and it compares the effect of the diode forward voltage and the deadtime on the voltage control of U_{DC}. On the left, the forward voltage V_D is increase by 200% from the nominal value $2.5V$ but the deadtime is not modified. On the right, the deadtime T_D is increased by 200% from the nominal value $1\mu s$. On both simulations, the voltage doesn't go below $390V$ such that the condition (2.26) is respected. Note that, larger oscillation occurs when the deadtime is increased and seems that the voltage control is more affected for variation of the deadtime than the diode forward voltage.

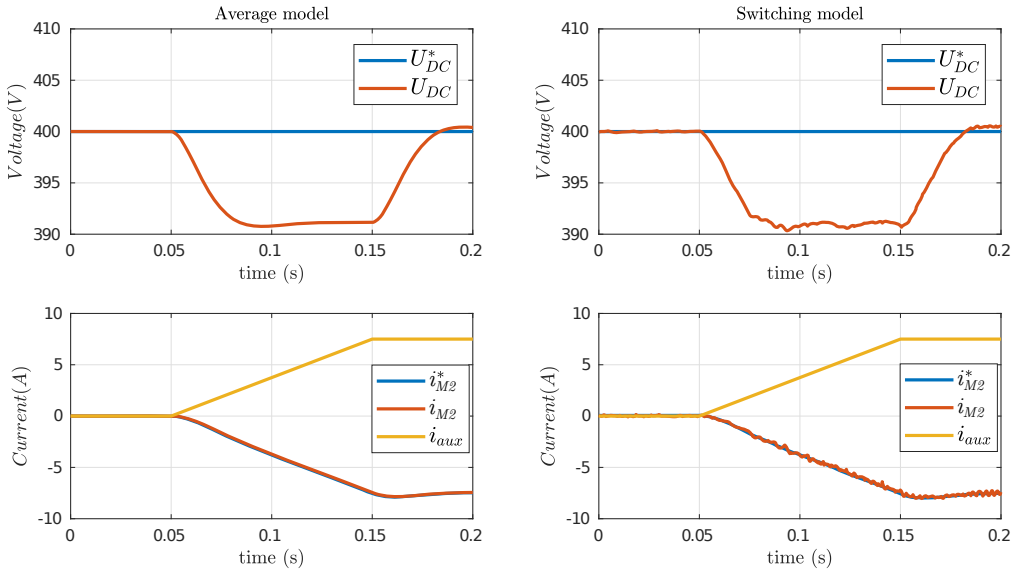

Figure 2.16 – Simulation with the average model on the left and with the switching model of the inverter on the right, $V_D = 2.5V$ and $T_D = 1\mu s$

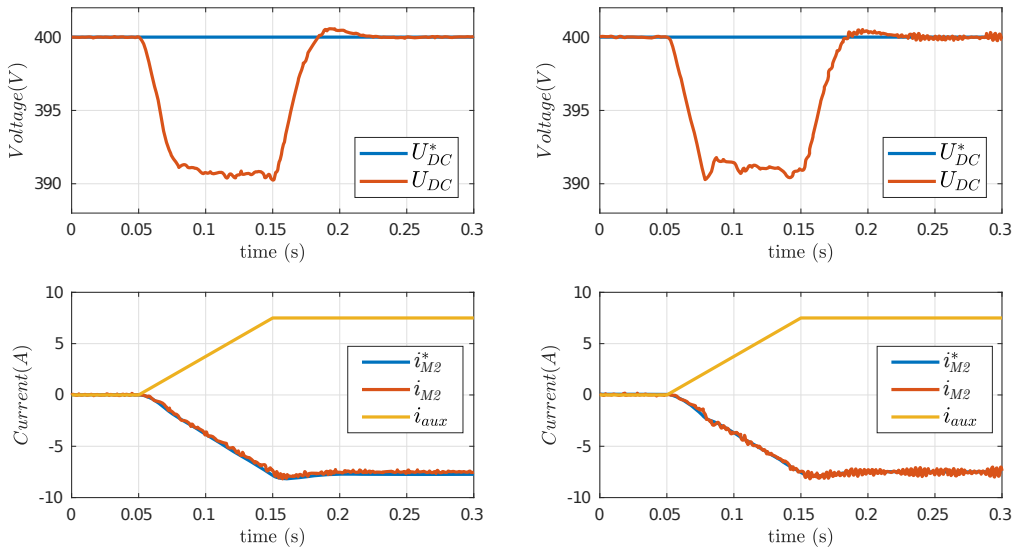

Figure 2.17 – Simulation with the switching model of the inverter – Left: $V_D = 5V$ and $T_D = 1\mu s$ – Right: $V_D = 2.5V$ and $T_D = 2\mu s$

2.6 Summary

Contributions

— Presentation of a dynamic modeling, offline optimization and control of the electrical motors.
— Proposition of a voltage control of the DC bus.
— Simulation of the voltage control under the inverter non-linearity.

Chapter 3

Control of the ICE speed

3.1 Introduction

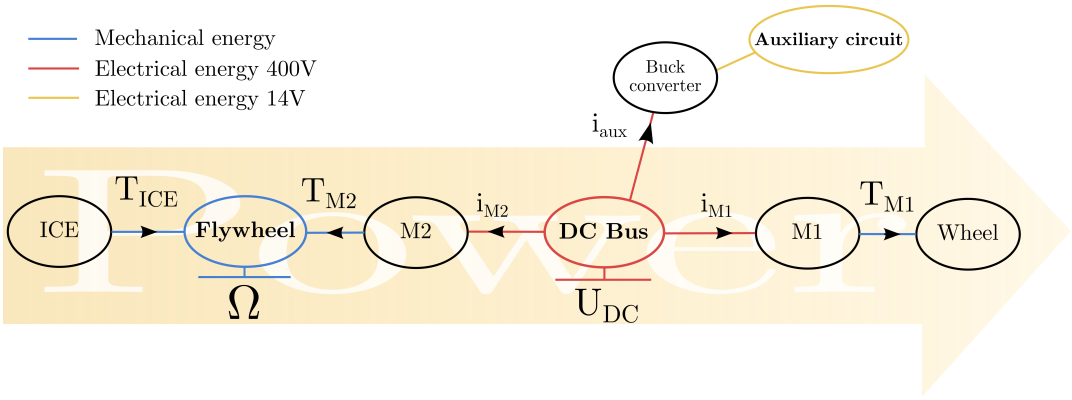

Figure 3.1 – Global Architecture

In this chapter, the modeling is made for larger time scale than the last chapter and considers the entire system of the hybrid serial vehicle figure 3.1. The principal aim is to realize the driver demand. This demand is sensed by the accelerator pedal and it has to somehow correspond to the torque of the M1. The goal of this chapter is to present different strategies for the regulation of two buffers and the realization of the torque demand. These two key parts are the DC bus voltage and rotational speed of the flywheel. In the serial hybrid vehicle, the power goes from the ICE to the M1 driving the wheel. The ICE produces mechanical power by burning the fuel, the M2 converts this power into electrical power and the M1 used this power to tract the vehicle. The ICE is connected to the M2 through a flywheel. This flywheel is originally designed to smooth the torque produce by the ICE, but here the flywheel acts like an energy storage. The dynamic of the rotational speed is dictated by the inertia of each rotational part (mainly the flywheel). The M2 is connected to the M1 via a DC bus. On a normal hybrid vehicle, the battery is connected to this DC bus and acts like an energy storage. However, here without the

battery, the only electrical storage is the capacitor present between the M2 and the M1. Each buffer has the level of energy storage represented by the physical value of the voltage and the rotational speed. In this configuration, the flywheel and the capacitor are the key to maintain the power transmission needed to realize the user demand.

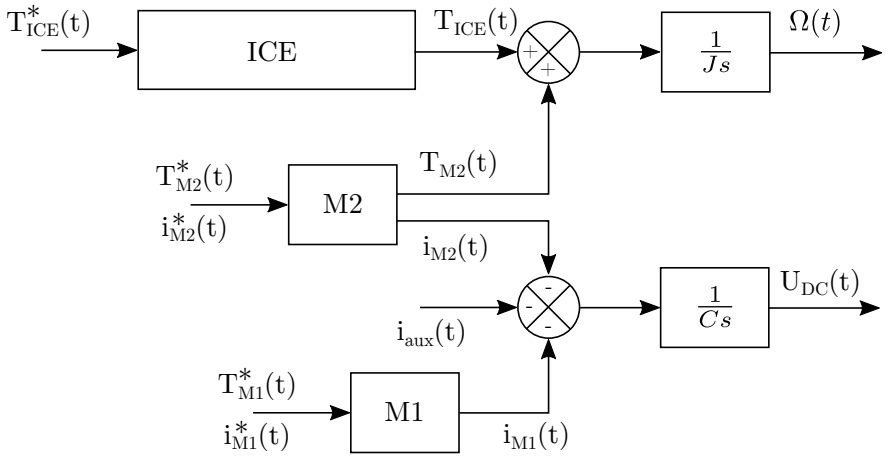

Figure 3.2 – Diagram of the control system

On figure 3.2, a diagram represents the structure of the system. It shows three inputs: the torque reference for the ICE, the torque or current reference of the M2 and the torque or current reference of the M1. Also, the control aim is to: realize the user demand that is the torque demand for the M1, stabilize the rotational speed of the flywheel and stabilize the voltage of the DC bus. Maintaining both of this value and realizing the user demand can be made with three different strategies. Where each strategy assigned one control aim to one input.

In the sequel, the mechanical part of the serial hybrid vehicle is examined. From the last chapter only the modeling of the ICE as well as the flywheel dynamic is missing. After presenting the last modeling, the different strategies are presented and illustrated with a simulation. Pro and cons of each strategy are given in order to select one strategy.

3.2 The macroscopic modeling

This section presents the modeling of the ICE, the flywheel and a simplified modeling of the electric part developed in the last chapter.

3.2.1 The ICE dynamic

From the literature, the ICE torque dynamic has been modeled as a first or second order linear system. This article [TM17] give an example where the ICE dynamic is a second order linear system and the author try to achieve traction control with a model predictive control approach. A more sophisticate approach, resembling at the model here, can be found in this article [HS97] and in this thesis [Bre12].

The ICE model describes here come from an empirical study of the motor. Where the company making the ICE has been running the motor on an instrumented test bench. Then, they have extracted the model and parameters from different tests.

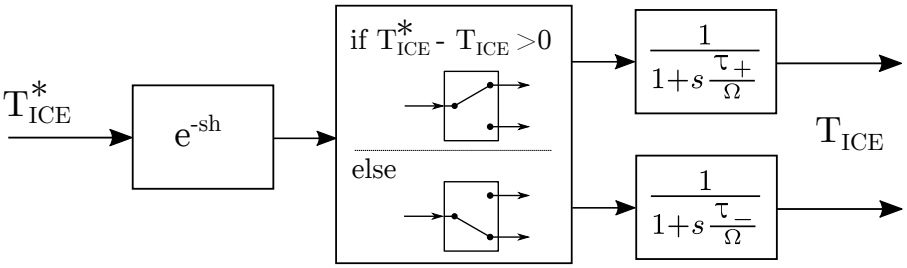

Figure 3.3 – Diagram describing the ICE modeling

Figure 3.3 illustrate the dynamic of the ICE in the laplace domain s. From the input, the torque reference $T^*_{ICE}(t)$ pass through a varying time delay $h(t) = 4\pi/\Omega(t)$ depending on the rotational speed of the flywheel $\Omega(t)$. If the delayed reference $T^*_{ICE}(t - h(t))$ is above the current output torque, the delayed reference $T^*_{ICE}(t-h(t))$ goes through a first order system with the time variable $\tau_+/\Omega(t)$. Else $T^*_{ICE}(t - h(t)) < T_{ICE}(t)$, the delayed reference $T^*_{ICE}(t-h(t))$ goes through a first order system with the time variable $\tau_-/\Omega(t)$.

In the time domain, the ICE dynamic is:

$$\dot{T}_{ICE}(t) = \frac{\Delta T_{ICE}(t)\Omega(t)}{\frac{\tau_- + \tau_+}{2} - \frac{\tau_- - \tau_+}{2} sign\Delta T_{ICE}(t)} \tag{3.1}$$

with $\Delta T_{ICE}(t) = T^*_{ICE}(t - h(t)) - T_{ICE}(t)$ and the following parameters

$$\tau_+ = \frac{5 \times 2\pi}{3},\ \tau_- = \frac{20 \times 2\pi}{3} \text{ and } h(t) = \frac{4\pi}{\Omega(t)}. \tag{3.2}$$

When introducing $\tau_{\pm} = (\tau_+ + \tau_-)/2$, the ICE dynamic becomes:

$$\dot{T}_{ICE}(t) = \frac{\Delta T_{ICE}(t)\Omega(t)}{\tau_{\pm} - \frac{\tau_- - \tau_+}{2} sign\Delta T_{ICE}(t)} \tag{3.3}$$

Figure 3.4 shows an illustration of the ICE dynamic at $1500RPM$ and $3000RPM$. The simulation shows the respond time being longer in the falling step than the rising step, unlike the input delay being the same on the rising and falling step.

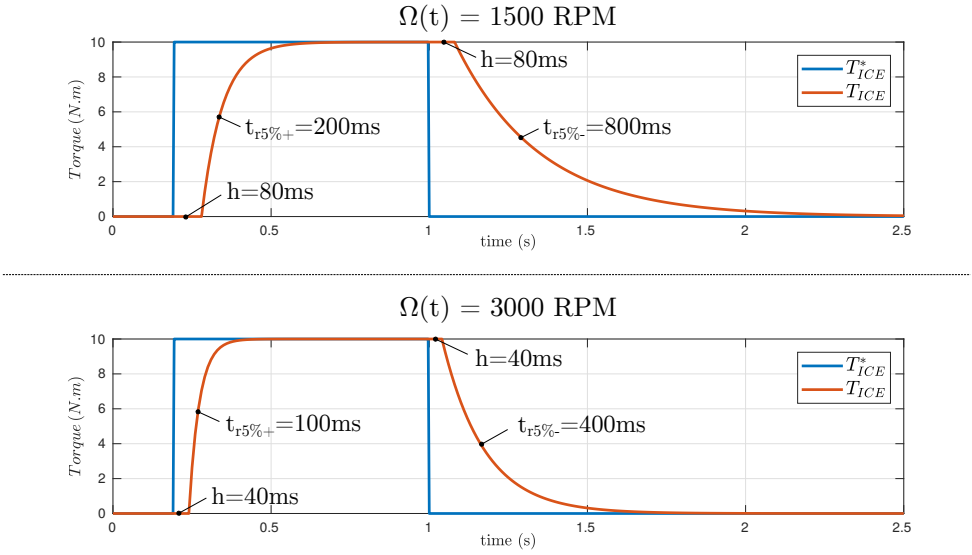

Figure 3.4 – Simulation of the ICE torque respond at $\Omega(t) = 1500\,RPM$ and $\Omega(t) = 3000\,RPM$

Remark 4 *Physically, the ICE controller realizes the torque demand T^*_{ICE} by actuating the throttle of the air intake. When the intake opens, the air path feeds the cylinder. But not instantly, depending on the flow rate, from the opening of the intake valve to the air entering in the cylinder a certain delay h occur. Also a direct correlation between the rotational speed Ω of the engine and the flow rate can be made such that: at low RPM, the delay h is much larger than at higher RPM. Then, the new air going inside the cylinder takes time to increase the output torque T_{ICE}. The same analogy goes for the time constants of the first order system: increasing the rotational speed Ω reduce the time constant $\tau_+/\Omega(t)$ to produce the output torque T_{ICE}.*

In order to design the control law and the predictor for the next strategies, the ICE

dynamic will be approximate by:

$$\dot{T}_{ICE}(t) = \frac{\Delta T_{ICE}(t)\Omega(t)}{\tau_{\pm}} \tag{3.4}$$

Remark 5 *As long as the system come close to the reference, that is* $\Delta T_{ICE}(t) = T^*_{ICE}(t - h(t)) - T_{ICE}(t) \approx 0$*, the sign function of* $\Delta T_{ICE}(t)$ *tends to constantly switch between* $+1$ *and* -1*, resulting in a comportment of the ICE dynamic being a first order system with the constant* $\tau_{\pm}$*. The use of the mean of the two constants* $\tau_{\pm} = (\tau_+ + \tau_-)/2$ *can be noted, it comes from the dynamics of the ICE* (3.3)*.*

3.2.2 The flywheel dynamic

The flywheel presented on figure 3.5 act as a dampening system, it smooth the torque output from the ICE and store mechanical energy. It fixes the rotational speed and ensures the energy transfer.

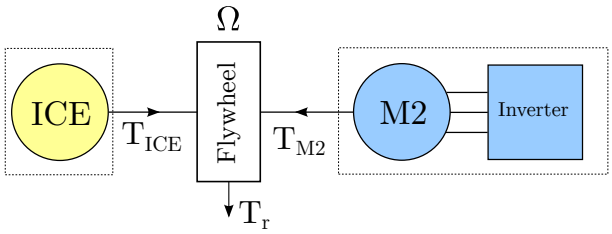

Figure 3.5 – The power generator assembly

The rotational speed dynamic is given by the torque balance such that:

$$\dot{\Omega}(t) \quad = \quad \frac{T_{ICE}(t) + T_{M2}(t) - T_r(t)}{J} \tag{3.5}$$

where J represent the inertia of all part between the ICE and M2 (shaft, flywheel, rotors, ...) and T_r the friction torque on the ICE and M2 shaft.

3.2.3 The electrical modeling

The electrical modeling corresponds at an extension of the model developed in the last chapter. From, the torque (2.9) and the optimization section 2.4, the power consumption

of the two PMSM are:

$$\begin{aligned} P_{M2}(t) &= U_{DC}(t)\, i_{M2}(t) = T_{M2}(t)\, \Omega(t) + P_{l2}(t) \\ P_{M1}(t) &= U_{DC}(t)\, i_{M1}(t) = T_{M1}(t)\, \Omega_{M1}(t) + P_{l1}(t) \end{aligned} \tag{3.6}$$

where P_{l1} and P_{l2} are the electrical losses between the electrical power and the mechanical power.

Also, the links between the torque produced by the PMSM and the current absorbed on the DC bus are:

$$T_{M2}(t) = \frac{i_{M2}(t) U_{DC}(t) - P_{l2}(t)}{\Omega(t)} \qquad T_{M1}(t) = \frac{i_{M1}(t) U_{DC}(t) - P_{l1}(t)}{\Omega_{M1}(t)} \tag{3.7}$$

3.2.4 The complete system modeling

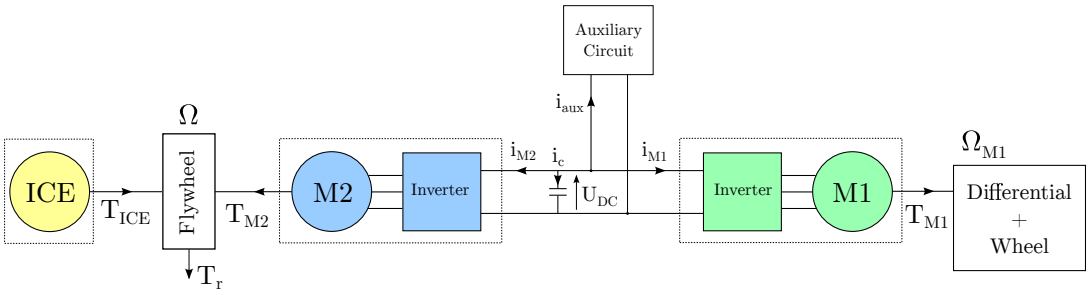

Figure 3.6 – Architecture of the serial hybrid vehicle

To sum up the last part, the state space model of the complete system figure 3.6 is:

$$\begin{aligned} \dot{\Omega}(t) &= \frac{T_{ICE}(t) + T_{M2}(t) - T_r(t)}{J} \\ \dot{T}_{ICE}(t) &= \frac{\Delta T_{ICE}(t)\Omega(t)}{\tau_{\pm} - \frac{\tau_- - \tau_+}{2} sign \Delta T_{ICE}(t)} \\ \dot{U}_{DC}(t) &= \frac{-i_{M2}(t) - i_{aux}(t) - i_{M1}(t)}{C} \end{aligned} \tag{3.8}$$

with $\Delta T_{ICE}(t) = T^*_{ICE}(t - h(t)) - T_{ICE}(t)$, $T_{M2}(t) = \dfrac{i_{M2}(t)\, U_{DC}(t) - P_{l2}(t)}{\Omega(t)}$ and $T_{M1}(t) = \dfrac{i_{M1}(t)\, U_{DC}(t) - P_{l1}(t)}{\Omega_{M1}(t)}$.

3.3 Control strategies

In this section, the objectives are to find a solution to: stabilize the rotational speed of the flywheel, stabilize the voltage of the DC bus and produce the requested torque on the M1. To realize each objective, three strategies has been developed, shown in this section and tested on the system (3.8). The system possesses three inputs: the torque reference for the ICE, the torque or current reference of the M2 and the torque or current reference of the M1. Each one of the three strategies differently assigns the control input to the objective.

Assumption 4 *For the simplification of the simulation and only in this chapter, the losses are not considered and the dynamic of the PMSMs are not introduced here, but they will be introduced in the next section. These simplifications imply:*

- $T_r(t) = 0$ *and* $P_{l1}(t) = P_{l2}(t) = 0$
- $T^*_{M2}(t) = T_{M2}(t)$ *and* $i^*_{M2}(t) = i_{M2}(t)$
- $T^*_{M1}(t) = T_{M1}(t)$ *and* $i^*_{M1}(t) = i_{M1}(t)$

3.3.1 Strategy 1: the M1 torque is the driver's demand

The first strategy developed here consists of:

- the user demand u is the M1 torque reference T^*_{M1},
- the current reference i^*_{M2} is in charge of stabilizing the DC bus voltage U_{DC},
- the torque reference T^*_{ICE} is utilized to stabilize the rotational speed of the flywheel Ω.

Rotational speed control design without taking into account the ICE input delay

On figure 3.7, the system is stabilized with two control law. The rotational speed control consists of a linearization of the output Ω relative to the input T^*_{ICE} without the delay, see [Glu15]. The control law is given by:

$$\begin{aligned} T^*_{ICE}(t) &= \frac{J\,\tau_{\pm}\,v(t)}{\Omega(t)} + T_{ICE}(t) \\ v(t) &= \ddot{\Omega}^*(t) + \lambda_2(\dot{\Omega}^*(t) - \dot{\Omega}(t)) + \lambda_1(\Omega^*(t) - \Omega(t)) + \lambda_0 \int_0^t (\Omega^*(\iota) - \Omega(\iota))d\iota \end{aligned} \tag{3.9}$$

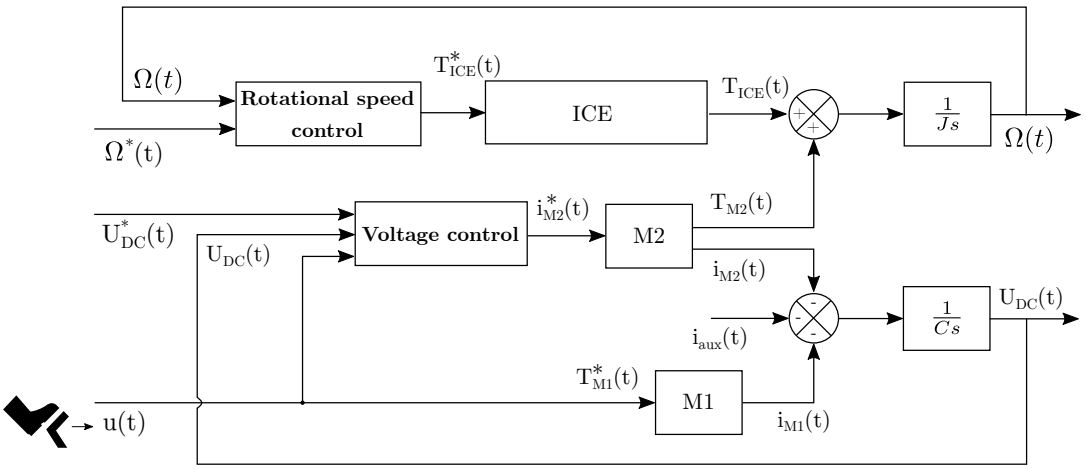

Figure 3.7 – Control scheme of the first strategy

where λ_0, λ_1 and λ_2 are the tuning gains and $\tau_\pm = (\tau_+ + \tau_-)/2$.

DC bus control design

The control law for the DC bus voltage has been taken from the section 2.5:

$$i^*_{M2}(t) \quad = \quad -C(\dot{U}^*_{DC}(t) + K_P(U^*_{DC}(t) - U_{DC}(t)) + K_I \int_0^t (U^*_{DC}(\iota) - U_{DC}(\iota))d\iota) \qquad (3.10)$$

Simulation

The simulation on figure 3.8 uses the parameters display in the table 3.1.

Symbol	Value
K_P	128
K_I	8464
λ_0	200
λ_1	235
λ_2	21

Table 3.1 – Simulation parameters

The aim is to stabilize the rotational speed at $\Omega^* = 2500RPM$ and the DC bus voltage at $U^*_{DC} = 400V$. The user demand represented by the M1 torque goes from 0 to $50N.m$ with a first order with a respond time at 5% in $1s$. The vehicle speed is $20km/h$, it corresponds at $\Omega_{M1} = 1750RPM$.

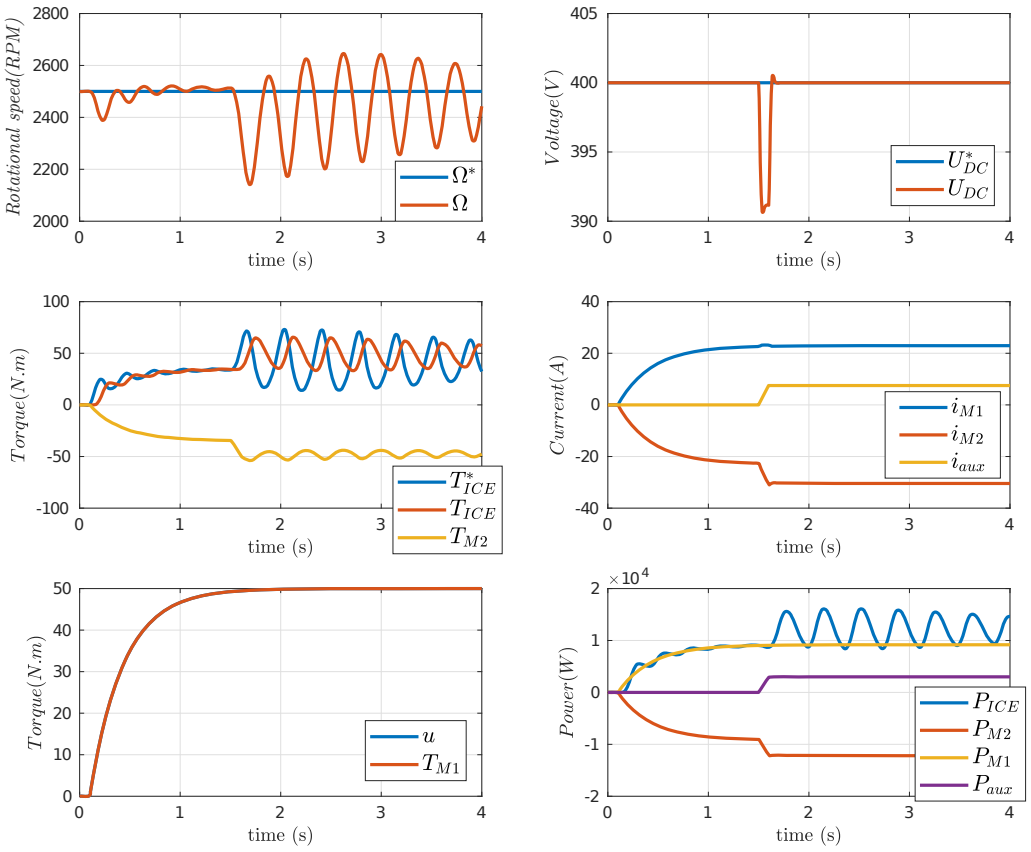

Figure 3.8 – Simulation with a disturbance $i_{aux} = 0$ to $7.5A$ in $100ms$ at $1.5s$

On the bottom of figure 3.8, the power of the M1 follows the torque and finished at $9.1kW$. The generated power of the M2 follows the consumption of the M1. Except at $1.5s$, when the auxiliary circuit disturbs the DC bus, it consume 0 to $3kW$ in $100ms$. It can be seen that the power P_{M1} consumes by the M1 doesn't change but the M2 compensates the auxiliary consumption by increasing the generated power, from $9.1kW$ to $12.1kW$. And the same effect goes for the ICE. The simulation shows a lot of oscillation on the rotational speed Ω, mostly due to the input delay of the ICE and a small part due to the double constant $\tau_{\pm}$ of the ICE. Note that, the oscillation error of Ω is around $\pm 300RPM$ and the voltage U_{DC} is kept around $\pm 10V$.

Introduction of the prediction scheme

A predictor is introduced to counteract the input delay of the ICE. See figure 3.9, the predictor is placed between the output of the system and the input of the rotational speed control. The predictor is used to approximate the rotational speed Ω of the flywheel and the ICE torque T_{ICE} in the near future $(t + h)$. The voltage control is kept as (3.10) and only the rotational speed control is adapted to the introduction of the predictor.

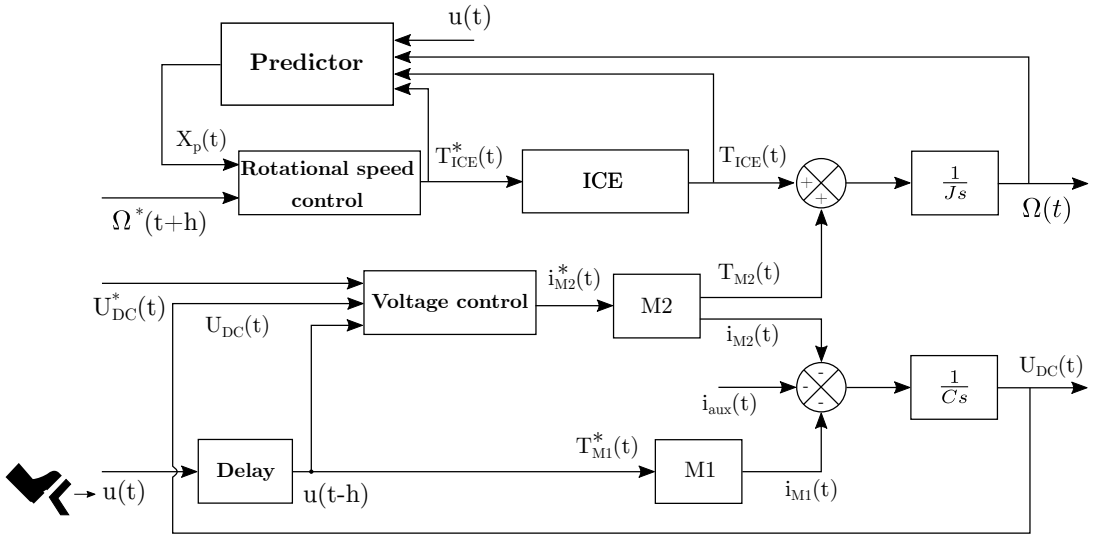

Figure 3.9 – Control scheme of the first strategy with the prediction

State space representation of the ICE

In order to introduce the predictor, the ICE dynamic is approximated as the equation (3.4) and presented in a vector-matrix format:

$$\dot{X}(t) = \begin{bmatrix} \dot{\Omega}(t) \\ \dot{T}_{ICE}(t) \end{bmatrix} = AX(t) + B\,T^*_{ICE}(t-h) + d(t) \tag{3.11}$$

with $A = \begin{bmatrix} 0 & 1/J \\ 0 & -\Omega/\tau_\pm \end{bmatrix}$, $B = \begin{bmatrix} 0 \\ \Omega/\tau_\pm \end{bmatrix}$ and $d(t) = \begin{bmatrix} \dfrac{T_{M2}(t)}{J} \\ 0 \end{bmatrix}$

The prediction

The predicted vector $X(t+h)$ for the state vector $X(t)$ is computed as [MO79] and [Léc+16]:

$$X(t+h) = e^{Ah}X(t) + \int_0^h e^{A(h-s)}BT^*_{ICE}(t-h+s)\mathrm{d}s + \int_0^h e^{A(h-s)}d(t+s)\mathrm{d}s \tag{3.12}$$

For the implementation, the disturbance term as to be known in the future:

$$d(t+h) = \begin{bmatrix} \dfrac{T_{M2}(t+h)}{J} \\ 0 \end{bmatrix} \tag{3.13}$$

As a first approximation, if $i_{aux} = 0$ and the DC bus converges around a constant voltage reference U^*_{DC}, this means that $\dot{U}_{DC} \approx 0$. From the DC bus dynamic (3.8), the M2 and M1 current is thereby:

$$i_{M2}(t+h) \approx -i_{M1}(t+h) \tag{3.14}$$

This approximation will be studied with the singular perturbation approach in the next chapter.

Thus, the equation (3.6) and the assumption 4 implies that:

$$T_{M2}(t+h) \;\; = -\frac{\Omega_{M1}(t+h)}{\Omega(t+h)}T_{M1}(t+h) = -\frac{\Omega_{M1}(t+h)}{\Omega(t+h)}u(t) \tag{3.15}$$

Remark 6 *The disturbance term d is supposed to be known at the current time t, but also in the future $t+h$. It's achieved by delaying the user demand u by h before applying it on the traction motor: $T_{M1}(t) = u(t-h) \rightarrow T_{M1}(t+h) = u(t)$.*

The state prediction (3.12) transforms the system (3.11) into a delay-free system:

$$\dot{X}_p(t) \;\; = AX_p(t) + B\,T^*_{ICE}(t) + d(t+h) \tag{3.16}$$

where

$$X_p(t) \;\; = \;\; \begin{bmatrix} X_{p1}(t) \\ X_{p2}(t) \end{bmatrix} = X(t+h). \tag{3.17}$$

The rotational speed control used previously (3.9) can be adapted to the delay-free

system (3.16) as following:

$$\begin{aligned} T^*_{ICE}(t) &= \frac{J\tau_{\pm}v(t)}{X_{p1}(t)} + X_{p2}(t) \\ v(t) &= \ddot{\Omega}^*(t+h) + \lambda_2(\dot{\Omega}^*(t+h) - \dot{X}_{p1}(t)) \\ &\quad +\lambda_1(\Omega^*(t+h) - X_{p1}(t)) + \lambda_0 \int_0^t (\Omega^*(\iota+h) - X_{p1}(\iota))d\iota \end{aligned} \tag{3.18}$$

where λ_0, λ_1 and λ_2 are the same tuning gain.

Simulation

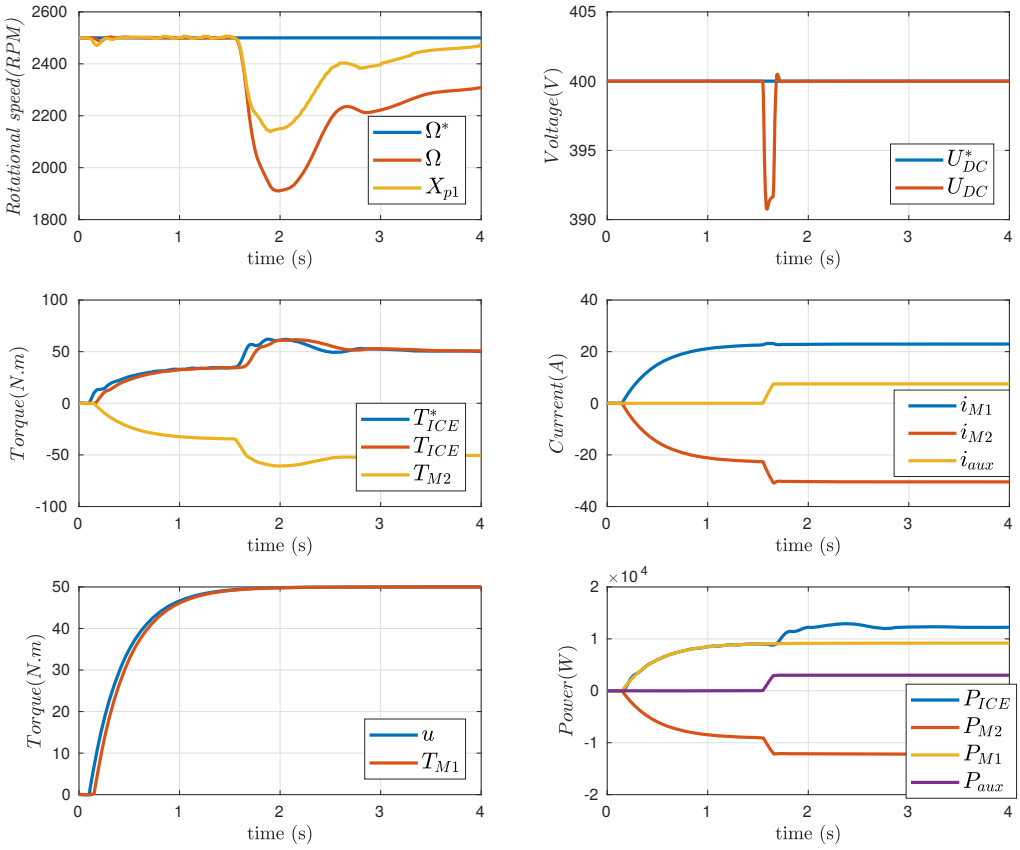

Figure 3.10 – Simulation with a disturbance $i_{aux} = 0$ to $7.5A$ in $100ms$ at $1.5s$

The new simulation, presented on figure 3.10, can be compared with the last simulation on figure 3.8. The used parameters are from the last simulation and displayed on the table

3.1. The aim is to stabilize the rotational speed at $\Omega^* = 2500RPM$ and the DC bus voltage at $U^*_{DC} = 400V$. The user demand represented by the M1 torque goes from 0 to $50N.m$ with a first order system characterized by a $1s$ respond time. The vehicle speed is set at $20km/h$, it corresponds at $\Omega_{M1} = 1750RPM$.

Unlike the last simulation, the predictor permits to stabilize the rotational speed Ω without a lot of oscillation. The DC bus voltage U_{DC} is also maintained above $390V$ when the disturbance occurs at $t = 1.5s$. Note the gap $\approx 120RPM$ between the rotational speed Ω and the predicted speed Ω_p when the disturbance occurs. The gap comes with the approximation (3.14) being somehow untruth and introducing an error on the prediction. But, without the knowledge of the auxiliary current i_{aux} and on a first approximation, the $120RPM$ gap doesn't hinder the system. In the next chapter, an observer method is proposed to estimate the losses neglected here and the auxiliary current.

3.3.2 Strategy 2: the M2 torque is the driver's demand

Figure 3.11 presents the second strategy developed here, and this strategy consists of:
— the user demand u is the M2 torque reference T^*_{M2},
— the current reference i^*_{M1} is in charge to stabilize the DC bus voltage U_{DC},
— the torque reference T^*_{ICE} is utilized to stabilize the rotational speed of the flywheel Ω.

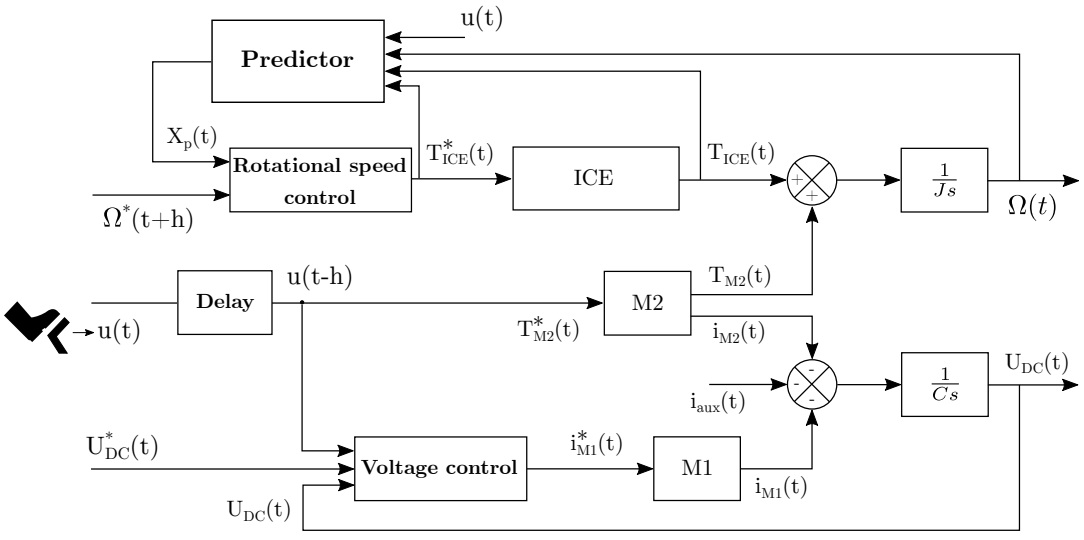

Figure 3.11 – Control scheme of the second strategy

Rotational speed dynamic

This strategy takes up the rotational speed control with the predictor from the previous strategy. Thus, the ICE dynamic is presented in a vector-matrix format:

$$\dot{X}(t) = \begin{bmatrix} \dot{\Omega}(t) \\ \dot{T}_{ICE}(t) \end{bmatrix} = AX(t) + B\,T^*_{ICE}(t-h) + d(t) \tag{3.19}$$

with $A = \begin{bmatrix} 0 & 1/J \\ 0 & -\Omega/\tau_\pm \end{bmatrix}$, $B = \begin{bmatrix} 0 \\ \Omega/\tau_\pm \end{bmatrix}$ and $d(t) = \begin{bmatrix} \frac{T_{M2}(t)}{J} \\ 0 \end{bmatrix}$.

The prediction

The predicted vector $X(t+h)$ for the state vector $X(t)$ is:

$$X(t+h) = e^{Ah}X(t) + \int_0^h e^{A(h-s)}BT^*_{ICE}(t-h+s)\mathrm{d}s + \int_0^h e^{A(h-s)}d(t+s)\mathrm{d}s \tag{3.20}$$

In this strategy, the disturbance term is directly linked to the user demand u:

$$d(t+h) = \begin{bmatrix} \frac{T_{M2}(t+h)}{J} \\ 0 \end{bmatrix} = \begin{bmatrix} \frac{u(t)}{J} \\ 0 \end{bmatrix} \tag{3.21}$$

Remark 7 *The idea is the same as remark 6: the disturbance term d is needed at the current time t, but also in the future $t+h$. It's achieved by delaying the user demand u by h before applying it on the M2: $T_{M2}(t) = u(t-h)$.*

The state prediction (3.20) transforms the system (3.19) into a delay-free system:

$$\dot{X}_p(t) \;\; = AX_p(t) + B\,T^*_{ICE}(t) + d(t+h) \tag{3.22}$$

where

$$X_p(t) \;\; = \;\; \begin{bmatrix} X_{p1}(t) \\ X_{p2}(t) \end{bmatrix} = X(t+h). \tag{3.23}$$

Rotational speed control design

The rotational speed control used previously (3.18) can be adapted to the delay-free system (3.22) as following:

$$\begin{array}{lcl} T^*_{ICE}(t) & = & \dfrac{J\tau_{\pm}v(t)}{X_{p1}(t)} + X_{p2}(t) \\ v(t) & = & \ddot{\Omega}^*(t+h) + \lambda_2(\dot{\Omega}^*(t+h) - \dot{X}_{p1}(t)) + \lambda_1(\Omega^*(t+h) - X_{p1}(t)) \\ & & +\lambda_0 \int_0^t (\Omega^*(\iota+h) - X_{p1}(\iota))d\iota \end{array} \tag{3.24}$$

where λ_0, λ_1 and λ_2 are the tuning gain.

DC bus control design

The control law for the DC bus voltage has been taken from the section 2.5:

$$i^*_{M1}(t) = -C(\dot{U}^*_{DC}(t) + K_P(U^*_{DC}(t) - U_{DC}(t)) + K_I \int_0^t (U^*_{DC}(\iota) - U_{DC}(\iota))d\iota) \tag{3.25}$$

Simulation

Symbol	Value
K_P	128
K_I	8464
λ_0	200
λ_1	235
λ_2	21

Table 3.2 – Simulation parameters

See figure 3.12, the simulation uses the parameters display in the table 3.2. The aim is to stabilize the rotational speed at $\Omega^* = 2500RPM$ and the DC bus voltage at $U^*_{DC} = 400V$. The vehicle speed is constant and $\Omega_{M1} = 1750RPM$. The user demand represented by the M2 torque goes from 0 to $-45N.m$ with a first order with a respond time at 5% in $1s$.

On the bottom of figure 3.12, the power of the M1 chases the traction torque and finished at $8.5kW$. The generated power of the M2 follows the consumption of the M1. Except at $1.5s$, when the auxiliary circuit disturbs the DC bus, it consumes 0 to $3kW$ in $100ms$. It can be see that the power P_{M2} produced by the M2 doesn't change, but the M1 consumption decreases when the auxiliary consumption happens, from $11.5kW$

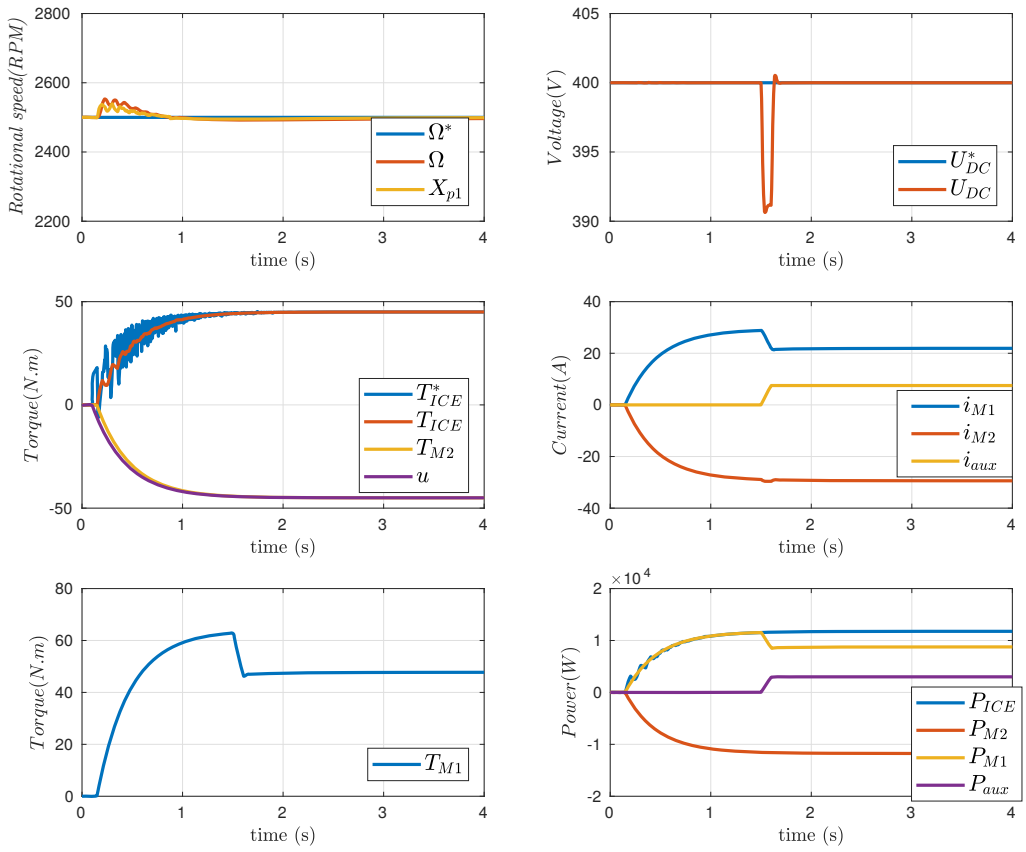

Figure 3.12 – Simulation of the strategy 2 with an instantaneous disturbance $i_{aux} = 7.5A$ at 1.5s

to $8.5kW$. The simulation shows some oscillation on the rotational speed Ω, a part is due to the double constant $\tau_\pm$ of the ICE. Note that, the voltage U_{DC} is kept around $\pm 10V$.

3.3.3 Strategy 3: the ICE torque is the driver's demand

The third strategy presented on figure 3.13 consists of:

— the user demand u is the ICE torque reference T^*_{ICE},

— the current reference i^*_{M1} is in charge of stabilizing the DC bus voltage U_{DC},

— the torque reference T^*_{M2} is utilized to stabilize the rotational speed of the flywheel Ω.

In this strategy, the input delay of the ICE doesn't effect the control law. Thus, the

predictor is not needed.

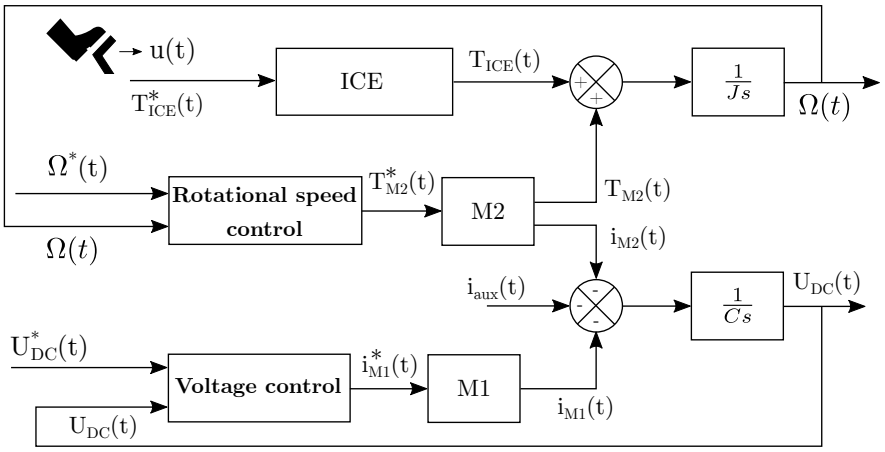

Figure 3.13 – Control scheme of the third strategy

Rotational speed control design

The rotational speed control consists of a linearization of the output Ω relative to the input T^*_{M2}, see [Glu15]. The control law is given by:

$$T^*_{M2}(t) = J(\dot{\Omega}^*(t) + \lambda_1(\Omega^*(t) - \Omega(t)) + \lambda_0 \int_0^t (\Omega^*(\iota) - \Omega(\iota))d\iota) - T_{ICE}(t) \quad (3.26)$$

where λ_0 and λ_1 are the tuning gain.

DC bus control design

The control law for the DC bus voltage has been taken from the section 2.5:

$$i^*_{M1}(t) = -C(\dot{U}^*_{DC}(t) + K_P(U^*_{DC}(t) - U_{DC}(t)) + K_I \int_0^t (U^*_{DC}(\iota) - U_{DC}(\iota))d\iota) \quad (3.27)$$

Simulation

See figure 3.14, the simulation uses the parameters display in table 3.3. The aim is to stabilize the rotational speed at $\Omega^* = 2500RPM$ and the DC bus voltage at $U^*_{DC} = 400V$. The vehicle speed is constant and $\Omega_{M1} = 1750RPM$. The user demand represented by

Symbol	Value
K_P	128
K_I	8464
λ_0	200
λ_1	235

Table 3.3 – Simulation parameters

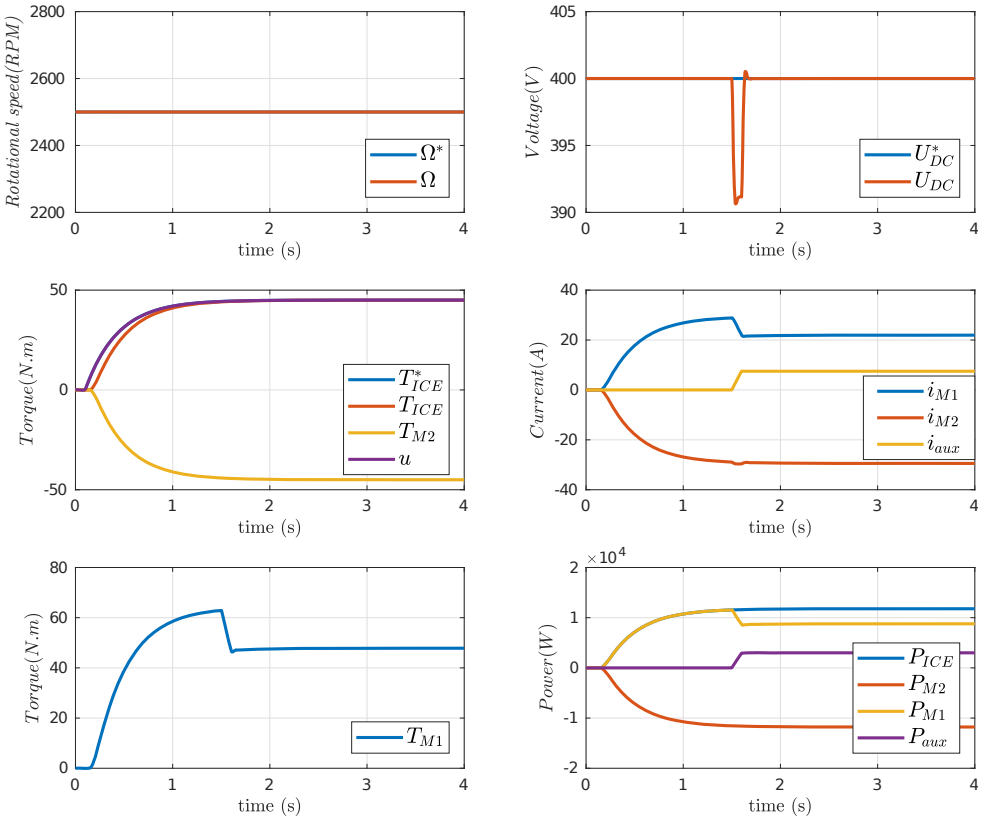

Figure 3.14 – Simulation of the third strategy with an instantaneous disturbance $i_{aux} = 7.5A$ at 1.5s

the M2 torque goes from 0 to $-45N.m$ with a first order with a respond time at 5% in $1s$.

On the bottom of figure 3.14, the power of the M1 follows the traction torque. Before, the auxiliary circuit disturbs the DC bus and consumes 0 to $3kW$ in $100ms$. The generated power of the M2 follows the consumption of the M1. When the auxiliary circuit turns on after $t = 1.5s$, it can be see that the power P_{M2} produced by the M2 doesn't change but the M1 consumption decreases from $11.5kW$ to $8.5kW$. The simulation shows some oscillation on the rotational speed Ω, a part is due to the double constant $\tau_\pm$ of the ICE.

Note that, the voltage U_{DC} is kept around $\pm 10V$.

3.4 Comparison between the strategies

The objective of this part is to show each aspect of the strategy developed here. Each strategy presented previously has downside and positive aspects. The table 3.4 drawn the different strong points.

Strategies comparison	Strategy 1	Strategy 2	Strategy 3
High respond time	✓✓✓	✓✓	✓
Complexity	✗✗	✗✗	✗
Predictor dependency	✗✗✗	✗✗✗	-
High frequencies disturbances on T_{M1}	-	✗✗✗	✗✗✗
Direct control of the traction	✓✓✓	✓✓	✓

Table 3.4 – Comparison of the strategies. Criteria are explained above.

Some explanation about the criteria is given here:

— the high respond time criterion refers to the respond time between the user demand and the output torque of the M1,

— the complexity criterion refers to the implementation complexity for computing the control scheme,

— the predictor dependency criterion refers to the necessity to implement a prediction scheme for the rotational speed control,

— the high frequencies disturbances on T_{M1} criterion refers to high frequencies perturbation occurring on the output torque of the M1,

— the direct control of the traction criterion refers to the direct link between the user demand and the output torque of the M1.

The topology of the strategies shows that the user demand goes from the direct control of the M1 torque on the strategy 1 to the indirect control on the strategy 3. For the strategy 1, the user demand is only delayed before it is applied to the M1 torque reference. In the strategy 2, the user demand is delayed then applied to the M2 torque demand. The M2

torque demand produces current on the DC bus that result in torque demand for the M1 in order to maintain the DC voltage. For the strategy 3, the cascade goes one level above, the user demand is the ICE torque demand, when the ICE produces the torque demand, it translates into an electrical power production by the M2, in order to maintain the flywheel speed. After, the M1 has to consume the power produced by applying more traction on the vehicle.

Thus, the strategy 1 comes with the positive aspect of high respond time, principally due to the direct control of the output torque and the fast actuation of the M1. The strategy 2 also comes with some high respond time from the fast actuation of the M2 and the M1, but with the disadvantage that every perturbation appearing on the DC bus is passed onto the M1 torque through the voltage control. This can introduce high frequencies disturbances on the traction. The same disadvantage comes with the strategy 3 where each perturbation occurring on the DC bus is rejected by the voltage control, i.e. the M1 torque. Moreover, the user demand on the strategy 3 is translated on the ICE torque with the slow dynamic of the ICE, resulting in low time respond from the user demand to the traction.

The strategy 1 and 2 have the complication of the implementation of a prediction scheme for the rotational speed control. Nevertheless, the strategy 1 has been chosen for the direct control of the traction against the possibility of having high frequencies disturbances on the M1 torque. This strategy will be developed in the next chapter.

3.5 Summary

Contributions

— Presentation of a dynamic modeling of the complete system.
— Proposition of three strategies for stabilizing the system and fulfill the user request.

Chapter 4

Control of a two time scales system - Singular perturbation approach and losses observation

4.1 Introduction

This chapter study the two time scales of the strategy 1 selected in the last chapter. The interaction is analyzed using singular perturbation approach. Indeed, the system under consideration has the particularity of having three concurrent time scales. The small time scale is the current dynamic of each electric motor (the alternator and the traction motor), the medium time scale is the voltage dynamic of the DC bus and the larger one is the rotational speed dynamic of the flywheel between the ICE and the alternator. While the interaction from the current of the PMSM and the voltage control has been approached in chapter 2. In this chapter, it is assumed that the parameters of the current control (i_q^*, i_d^*) are sufficiently large such that the current dynamic is faster than the voltage and rotational speed dynamics (see the assumption 7). The challenge is to control the DC bus voltage and the rotational speed of the flywheel with the constraint of a slow variation of the ICE torque and a fast variation of the electric current.

In the context of controlling a system with two time scales, the Hydrogen Fuel Cell (HFC) vehicle presents similar characteristics of the system here. Indeed, the HFC constraints the system, in the same way as the ICE, by the slow variation of his current output. [SGA20] describes the mathematical model of the HFC with DC-DC boost converter and supercapacicator. After, the authors proposes a control architecture based on the relative degree approach to achieve a decoupling and proposes a sliding mode controller. [Hil+13] proposes a passivity-based controller to coordinate HFC system and ensures the distribution of each dynamic. Moreover, the work on the singular perturbation approach presented by [Gha+11] has inspired the sequel. In this section, the dynamic of the PMSM

is not considered here. But if it was considered, the singular perturbation approach can be used between the current dynamic of the PMSM and the voltage control of the inverter as the paper [Agh+17].

Firstly a brief recall on the singular perturbation approach is given. Secondly, the singular perturbation is employed on the previous system and the approximation made in the last chapter is enhanced. Lastly, a method based on state observation is used to estimate the power losses highlighted. This chapter led to several publications [Rou+20a], [Rou+20b] and [Rou+21].

4.2 Singular perturbation approach

The system under consideration is a two time scales system. The control/management challenge is to stabilize:

— the DC bus voltage U with small variations under the constraint of a small capacitor using the fast electrical actuator,

— the rotational speed of the ICE-PMSM by the slow control torque of the ICE in the presence of the large flywheel.

To achieve this goal, a singular perturbation approach [KKO86; Kha96] is employed.

In the sequel, the singular perturbation approach is recalled, the system model is written in the state space form and the fast control law is designed as well as the slow control.

4.2.1 Brief recall of singular perturbation approach

Let us consider the following nonlinear system:

$$\dot{x} = f(x, \xi, \varepsilon) \tag{4.1}$$

$$\varepsilon\dot{\xi} = g(x, \xi, \varepsilon) \tag{4.2}$$

with $x \in R^m$, $\xi \in R^n$, ε a small positive parameter and f, g two analytical vector fields of appropriate dimensions. Roughly speaking, x can be seen as the slow state and ξ as the fast variable. Nevertheless, this statement must be clarified and some assumptions and theoretical developments must be added. First of all, it is usual to decompose the system (4.1)-(4.2) into two decoupled time scales dynamics. For this purpose, it is important to be able to compute the so-called slow manifold $\xi = \phi(x, \varepsilon)$.

It is the function ϕ that must verify the following equation:

$$\varepsilon\dot{\phi}(x,\varepsilon) = g(x,\phi(x,\varepsilon),\varepsilon) \tag{4.3}$$

where

$$\phi(x,\varepsilon) = \sum_{i=0}^{\infty} \alpha_i(x)\frac{\varepsilon^i}{i!} \tag{4.4}$$

is computed iteratively [Vas63]. For example the so-called frozen solution verifies

$$0 = g(x,\alpha_0(x),0).$$

The following assumption is generally requested for the existence of α_0.

Assumption 5 *The Jacobian* $\{\frac{\partial g(x,\xi,0)}{\partial \xi}\}$ *is regular in the considered slow and fast state spaces* $x \in D_x \subset R^M$ *and* $\xi \in D_\xi \subset R^n$*, respectively.*

This assumption is directly linked to the implicit function theorem and in the nonlinear case more than one solution is possible (this particular case is outside the scope of this thesis). Now, it is important to know if the system (4.1)-(4.2) converges on a slow manifold that is given by the well-known Tikhonov's theorem reformulated in [Hun04]. But before recalling the theorem, it is necessary to analyze the fast dynamics on the boundary-layer. For this, a new state variable $\eta = \xi - \phi$ is introduced and η converges rapidly to zero if the system behaviour converges on the slow manifold. This manifold is the ξ behaviour recovered when the fast transient time is ended ("outside the boundary-layer").

The η dynamics are equal to:

$$\dot{\eta} = \frac{1}{\varepsilon}g(x,\phi(x,\varepsilon)+\eta,\varepsilon) - \frac{\partial\phi(x,\varepsilon)}{\partial t}. \tag{4.5}$$

Setting $\varsigma = \dfrac{t}{\varepsilon}$, (4.5) may be rewritten as follows:

$$\frac{\partial\eta}{\partial\varsigma} = g(x,\phi(x,\varepsilon)+\eta,\varepsilon) - \frac{\partial\phi(x,\varepsilon)}{\partial\varsigma}. \tag{4.6}$$

Assumption 6 *The system (4.6) is at least locally in* η *and uniformly in* x *exponentially stable.*

Hereafter, Tikhonov's Theorem without considerations of time domain, existence and

uniqueness of the attractivity domain with respect to η solution (for example local Lipschitz condition around zero is ensured by Assumption 5) is introduced.

Theorem 1 *Assume that Assumptions 5-6 hold. There exist $\varepsilon > 0$ sufficiently small, such that the dynamics (4.1)-(4.2) tend to the slow dynamic* (4.7)

$$\dot{x} = f(x, \phi(x, \varepsilon), \varepsilon). \tag{4.7}$$

In many applications, $\phi(x, \varepsilon)$ in (4.7) is approximated by it frozen solution α_0 (given in (4)):

$$\dot{x} = f(x, \alpha_0(x), 0). \tag{4.8}$$

Remark 8 *This section limits itself to the frozen solution of the slow manifold, i.e. $\phi \simeq \alpha_0(x)$. Nevertheless, for example, when the slow dynamics has a behavior too close to fast dynamics, it is necessary to do a better approximation of ϕ.*

4.2.2 A state space model

The system (3.8) under consideration is recalled in a state variable form:

$$\begin{aligned}
\dot{x}_1(t) &= \frac{1}{J}(x_2(t) + \frac{i_{M2}(t)\, x_3(t) - P_{l2}(t)}{x_1(t)} - T_r(t)) \\
\dot{x}_2(t) &= \frac{x_1(t)\,(T^*_{ICE}(t-h) - x_2(t))}{\tau_\pm - \dfrac{\tau_- - \tau_+}{2}\, sign(T^*_{ICE}(t-h) - x_2(t))} \\
\dot{x}_3(t) &= \frac{1}{C}(-i_{M2}(t) - i_{aux}(t) - \frac{T_{M1}(t)\,\Omega_{M1}(t) + P_{l1}(t)}{x_3(t)})
\end{aligned} \tag{4.9}$$

with the state vector

$$x(t) = \begin{bmatrix} x_1(t) \\ x_2(t) \\ x_3(t) \end{bmatrix} = \begin{bmatrix} \Omega(t) \\ T_{ICE}(t) \\ U_{DC}(t) \end{bmatrix}. \tag{4.10}$$

Remark 9 *The model* (4.9) *contains two time scales processes, the fast one is given by $x_3 = U_{DC}$ dynamic and the slow one is represented by the dynamics of $x_1 = \Omega$ and $x_2 = T_{ICE}$.*

Assumption 7 *The parameters of the current control (i^*_q, i^*_d) are sufficiently large such*

that the internal controlled current dynamic of the M2 is greatly faster than all dynamics of (4.9).

The current in d-q frame are assigned by the very fast controller (2.18) where k_{di} and k_{dp} are the control gain for the d axis and k_{qi} and k_{qp} are the control gain for the q axis. Consequently, choosing parameters k_{dp}, k_{di}, k_{qp}, k_{qi} sufficiently large and the state-space representation of system (4.9) becomes:

$$\begin{aligned}
\dot{x}_1(t) &= \frac{1}{J}(x_2(t) + \frac{i^*_{M2}(t)\, x_3(t) - P_{l2}(t)}{x_1(t)} - T_r(t)) \\
\dot{x}_2(t) &= \frac{x_1(t)\,(T^*_{ICE}(t-h) - x_2(t))}{\tau_{\pm} - \dfrac{\tau_- - \tau_+}{2}\, sign(T^*_{ICE}(t-h) - x_2(t))} \\
\dot{x}_3(t) &= \frac{1}{C}(-i^*_{M2}(t) - i_{aux}(t) - \frac{T^*_{M1}(t)\,\Omega_{M1}(t) + P_{l1}(t)}{x_3(t)})
\end{aligned} \tag{4.11}$$

Assumption 8 *The following quantities $i_{aux}(t)$, $T^*_{M1}(t)$, $P_{l1}(t)$, $P_{l2}(t)$, $\Omega_{M1}(t)$, and $x^*_3(t)$ are slowly variable and can be considered such that $i_{aux}(t) \approx i_{aux}(t+h)$, $T^*_{M1}(t) \approx T^*_{M1}(t+h)$, $P_{l1}(t) \approx P_{l1}(t+h)$, $P_{l2}(t) \approx P_{l2}(t+h)$, $\Omega_{M1}(t) \approx \Omega_{M1}(t+h)$, and $x^*_3(t) \approx x^*_3(t+h)$.*

Indeed, this assumption ensured the convergence of the control approach and the prediction implementation.

4.2.3 Control diagram

The strategy developed with the singular perturbation approach comes from the strategy 1 and it is depicted in Fig. 4.1. It is composed of two subsystems: fast loop based on the fast actuators (PMSM) that drives the DC bus voltage U_{DC}; and slow loop based on the slow actuator (ICE) that stabilizes the rotational speed Ω of the flywheel. For the seek of clarity, the control is designed first by considering P_{l1}, P_{l2}, T_r and i_{aux} known. Then as in practice it is not the case, they will be estimated by the proposed observer to be integrated in the control.

4.2.4 The fast control law design

The fast voltage control in (4.12) is a PI controller in terms of i^*_{M2} that stabilizes the DC bus voltage $x_3 = U_{DC}$ at the reference level $x^*_3 = U^*_{DC}$:

$$i^*_{M2} = -C\,(K_P\,(x^*_3(t) - x_3(t)) + K_I\, x_4(t)) \tag{4.12}$$

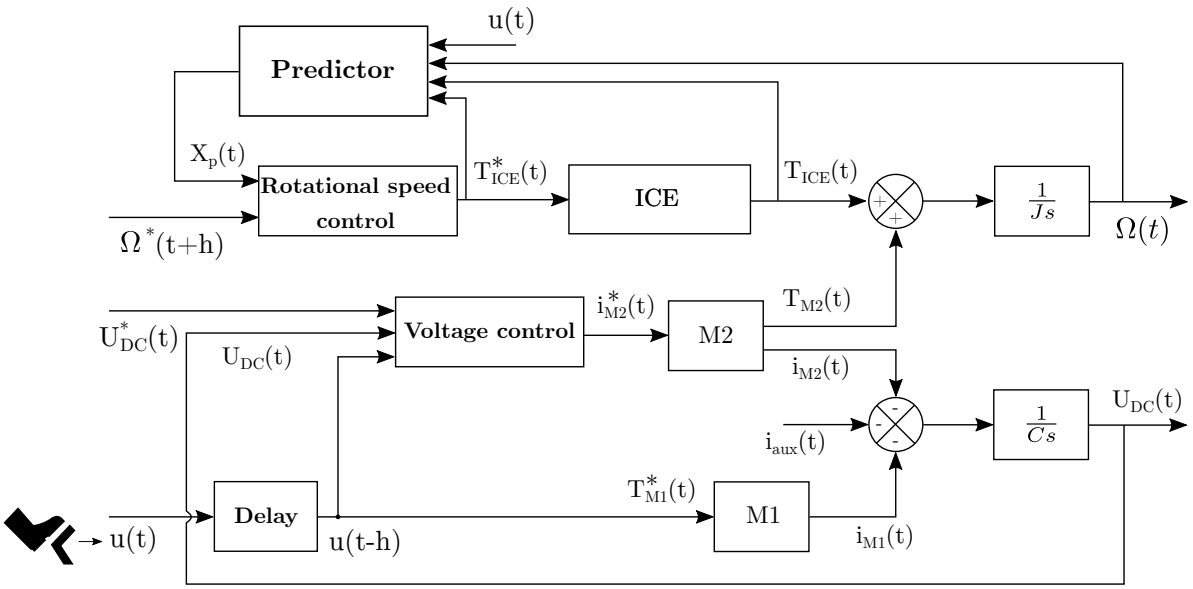

Figure 4.1 – Control scheme of the first strategy with the prediction

where $x_4(t) = \int_0^t (x_3^*(\iota) - x_3(\iota))d\iota$.

The control input (4.12) being applied to system (4.11) yields the closed loop nonlinear system:

$$\begin{aligned}
\dot{x}_1(t) &= \frac{1}{J}(x_2(t) + \frac{-C\left(K_P\left(x_3^*(t) - x_3(t)\right) + K_I\, x_4(t)\right) x_3(t) - P_{l2}(t)}{x_1(t)} - T_r(t)) \\
\dot{x}_2(t) &= \frac{x_1(t)\left(T^*_{ICE}(t-h) - x_2(t)\right)}{\tau_{\pm} - \dfrac{\tau_- - \tau_+}{2}\, sign(T^*_{ICE}(t-h) - x_2(t))} \\
\dot{x}_3(t) &= K_P(x_3^*(t) - x_3(t)) + K_I x_4(t) - \frac{i_{aux}(t)}{C} - \frac{T^*_{M1}(t)\,\Omega_{M1}(t) + P_{l1}(t)}{x_3(t)\,C} \\
\dot{x}_4(t) &= x_3^*(t) - x_3(t)
\end{aligned} \tag{4.13}$$

Following the singular perturbation approach, the fast variables are introduced as

$$\begin{aligned}
\varepsilon\,\xi_1(t) &= x_3^*(t) - x_3(t) \\
\varepsilon^2\,\xi_2(t) &= x_4(t)
\end{aligned} \tag{4.14}$$

Then system (4.13) can be rewritten as follows:

$$\begin{aligned}
\dot{x}_1(t) &= \frac{1}{J}(x_2(t) + \frac{-C\,(K'_P\,\xi_1(t) + K'_I\,\xi_2(t))\,x_3(t) - P_{l2}(t)}{x_1(t)} - T_r(t)) \\
\dot{x}_2(t) &= \frac{x_1(t)\,(T^*_{ICE}(t-h) - x_2(t))}{\tau_\pm - \frac{\tau_- - \tau_+}{2}\,sign(T^*_{ICE}(t-h) - x_2(t))} \\
\varepsilon\dot{\xi}_1(t) &= -K'_P\xi_1(t) - K'_I\xi_2(t) + \frac{i_{aux}(t)}{C} + \frac{T^*_{M1}(t)\,\Omega_{M1}(t) + P_{l1}(t)}{x_3(t)\,C} \\
\varepsilon\dot{\xi}_2(t) &= \xi_1(t)
\end{aligned} \tag{4.15}$$

where the tuning parameters of the fast control (4.12) are given by

$$K_P = \frac{K'_P}{\varepsilon} \text{ and } K_I = \frac{K'_I}{\varepsilon^2}. \tag{4.16}$$

The tuning choice of K'_P and K'_I is made such that the polynomial $s^2 + K'_P s + K'_I$ is Hurwitz that yields the desired characteristics of the transient response. According to [KKO86], eq. (4.15) is rewritten in a singular perturbation form:

$$\dot{X}(t) = f(t, X(t), \xi(t), \varepsilon) \tag{4.17}$$

$$\varepsilon\dot{\xi}(t) = g(t, X(t), \xi(t), \varepsilon) \tag{4.18}$$

where $X(t) = [x_1(t), x_2(t)]^T$, $\xi(t) = [\xi_1(t), \xi_2(t)]^T$ and ε is a small positive parameter.

Now, the frozen solution of the fast dynamic equation (4.15), i.e. $\varepsilon = 0$, is computed as follows:

$$\alpha_0(t) = \begin{bmatrix} 0 \\ \dfrac{i_{aux}(t)}{K'_I\,C} + \dfrac{T^*_{M1}(t)\,\Omega_{M1}(t) + P_{l1}(t)}{x_3(t)\,K'_I\,C} \end{bmatrix}. \tag{4.19}$$

Proposition 1 *For all $x_1(t) > \Omega_{min} > 0$ and $x_3(t) > U_{min} > 0$, a sufficiently small parameter $\varepsilon > 0$ exists such that the dynamics* (4.17)-(4.18) *can be accurately approximated by their slow dynamics described by the following system:*

$$\begin{aligned}
\dot{X}(t) &= f(t, X(t), \alpha_0(t), 0) \\
&= \begin{pmatrix} \dfrac{1}{J}(x_2(t) - i_{aux}(t)\dfrac{x^*_3(t)}{x_1(t)} - \dfrac{T^*_{M1}(t)\,\Omega_{M1}(t) + P_{l1}(t)}{x_1(t)} - \dfrac{P_{l2}(t)}{x_1(t)} - T_r(t)) \\ \dfrac{x_1(t)\,(T^*_{ICE}(t-h) - x_2(t))}{\tau_\pm - \frac{\tau_- - \tau_+}{2}\,sign(T^*_{ICE}(t-h) - x_2(t))} \end{pmatrix}
\end{aligned} \tag{4.20}$$

Proof 1 *Considering the first term of* (4.4)*. Then by setting* $\eta(t) := \xi(t) - \alpha_0(t)$*, the fast dynamic* (4.18) *becomes:*

$$\begin{aligned} \dot{\eta}_1(t) &= \frac{-K'_P\,\eta_1(t) - K'_I\,\eta_2(t)}{\varepsilon} \\ \dot{\eta}_2(t) &= \frac{\eta_1(t)}{\varepsilon} - \Gamma(t) \end{aligned} \tag{4.21}$$

where $\Gamma(t) = \frac{d}{dt}(\frac{i_{aux}(t)}{K'_I\,C} + \frac{T^*_{M1}(t)\,\Omega_{M1}(t) + P_{l1}(t)}{x_3(t)\,K'_I\,C})$.

This gives

$$\begin{aligned} \Gamma(t) = \frac{1}{K'_I\,C}\Bigg(&\frac{d\,i_{aux}(t)}{dt} + \frac{\Omega_{M1}(t)}{x^*_3(t) - \varepsilon\eta_1(t)}\frac{d\,T^*_{M1}(t)}{dt} + \frac{T^*_{M1}(t)}{x^*_3(t) - \varepsilon\eta_1(t)}\frac{d\,\Omega_{M1}(t)}{dt} \\ &+ \frac{1}{x^*_3(t) - \varepsilon\eta_1(t)}\frac{d\,P_{l1}(t)}{dt} - \frac{T^*_{M1}(t)\,\Omega_{M1}(t) + P_{l1}(t)}{(x^*_3(t) - \varepsilon\eta_1(t))^2}(K'_P\,\eta_1(t) + K'_I\,\eta_2(t))\Bigg). \end{aligned} \tag{4.22}$$

As by assumptions, $i_{aux}(t)$*,* $T^*_{M1}(t)$*,* $\Omega_{M1}(t)$*,* $P_{l1}(t)$*, and* $x^*_3(t)$ *are slowly variable, i.e.* $\frac{d\,i_{aux}(t)}{dt} = \frac{d\,T^*_{M1}(t)}{dt} = \frac{d\,\Omega_{M1}(t)}{dt} = \frac{d\,P_{l1}(t)}{dt} = \dot{x}^*_3(t) = 0$*, one has*

$$\Gamma(t) = -\frac{T^*_{M1}(t)\,\Omega_{M1}(t) + P_{l1}(t)}{K'_I\,C\,(x^*_3(t) - \varepsilon\eta_1(t))^2}(K'_P\,\eta_1(t) + K'_I\,\eta_2(t)). \tag{4.23}$$

Under assumption $x^*_3 - \varepsilon\eta_1 > U_{min} > 0$*,* (4.23) *is locally Lipschitz with respect to* η_1 *and* η_2*, then* (4.21) *becomes*

$$\begin{aligned} \dot{\eta}_1(t) &= \frac{-K'_P\,\eta_1(t) - K'_I\,\eta_2(t)}{\varepsilon} \\ \dot{\eta}_2(t) &= \frac{\eta_1(t)}{\varepsilon} + \Lambda_1(t)\,\eta_1(t) + \Lambda_2(t)\,\eta_2(t) \end{aligned} \tag{4.24}$$

with $|\Lambda_1(t)| \leq K'_P\frac{T^*_{M1}(t)\,\Omega_{M1}(t) + P_{l1}(t)}{K'_I\,C\,U^2_{min}}$ *and* $|\Lambda_2(t)| \leq \frac{T^*_{M1}(t)\,\Omega_{M1}(t) + P_{l1}(t)}{C\,U^2_{min}}$.

Consequently, for $\varepsilon \to 0^+$*, system* (4.21)*, with respect to the choice of gains* K'_P *and* K'_I*, is stable* $\forall\ t \geq 0$ *(this verifies Assumption 6). Moreover,* (4.21) *verifies that* $\frac{\partial\dot{\eta}}{\partial\eta}$ *is regular (see Assumption 5 for our considered case). From Tikhonov's theorem (Theorem 1) a slow manifold* (4.20) *exists for all* $x_1(t) > \Omega_{min} > 0$*.*

Remark 10 *In practice, due to the ICE non reversibility and the necessity to produce the power, the condition* $x_1(t) > \Omega_{min} > 0$ *holds for all* $t \geq 0$*. Moreover, due to the necessity*

to power the auxiliary circuit, the DC bus voltage is always maintained at a minimum level and the condition $x_3(t) > U_{min} > 0$ *holds for all* $t \geq 0$.

Remark 11 *Hereafter, the slow closed loop control will be designed by using the model* (4.20) *such that its dynamic is slower than the dynamic* (4.18).

4.2.5 The slow control law design

The desired reference point for $x_1(t)$ is given by $x_1^*(t) = \Omega^*(t)$, where Ω^* is the desired rotational speed. The torque demand T_{M1}^* represents the driving cycle of the serial hybrid electric vehicle.

Equation (4.20) is presented in a vector-matrix format:

$$\dot{X}(t) = \begin{pmatrix} \frac{1}{J}(x_2(t) - i_{aux}(t)\frac{x_3^*(t)}{x_1(t)} - \frac{T_{M1}^*(t)\,\Omega_{M1}(t) + P_{l1}(t)}{x_1(t)} - \frac{P_{l2}(t)}{x_1(t)} - T_r(t)) \\ \dfrac{x_1(t)\,(T_{ICE}^*(t-h) - x_2(t))}{\tau_{\pm} - \frac{\tau_- - \tau_+}{2}\,sign(T_{ICE}^*(t-h) - x_2(t))} \end{pmatrix} \tag{4.25}$$

From the strategy 1, it can be seen that the system (4.25) is more complete then the system (3.11) used in the prediction. Nevertheless, without the knowledge of the auxiliary current i_{aux}, the friction losses T_r and the electrical losses P_{l1} and P_{l2}, the prediction can be used as described in the strategy 1. Greater will be the losses, greater will be the prediction error on the rotational speed. Fortunately, the losses are small in compare of the traction power. But an observer method will be introduced in the next part in order to fulfill the lack.

Recall of the prediction

In order to introduce the predictor, the ICE dynamic is approximated as the equation (3.4) and presented in a vector-matrix format:

$$\dot{X}(t) = AX(t) + B\,T_{ICE}^*(t-h) + d(t) \tag{4.26}$$

with $A = \begin{bmatrix} 0 & 1/J \\ 0 & -x_1(t)/\tau_{\pm} \end{bmatrix}$, $B = \begin{bmatrix} 0 \\ x_1(t)/\tau_{\pm} \end{bmatrix}$ and

$$d(t) = \begin{bmatrix} -\dfrac{\Omega_{M1}(t)}{x_1(t)\,J} T^*_{M1}(t) - \dfrac{P_{l1}(t) + i_{aux}(t)\,x^*_3(t)}{x_1(t)\,J} - \dfrac{P_{l2}(t)/x_1(t) + T_r(t)}{J} \\ 0 \end{bmatrix}.$$

The predicted vector $X_p(t)$ for the state vector $X(t)$ is computed as [MO79], [Léc+16] (also see Fig.4.1):

$$\begin{array}{l} X_p(t) = [X_{p1}(t), X_{p2}(t)]^T = X(t+h) \\ = e^{Ah}X(t) + \int_0^h e^{A(h-s)}BT^*_{ICE}(t-h+s)\mathrm{d}s + \int_0^h e^{A(h-s)}d(t+s)\mathrm{d}s \end{array} \tag{4.27}$$

The state prediction (4.27) transforms the system (4.26) into a delay-free system:

$$\dot{X}_p(t) = AX_p(t) + BT^*_{ICE}(t) + d(t+h) \tag{4.28}$$

Since (4.28) is not delayed anymore, all the controllers for delay-free systems can be used to stabilize it.

The control T^*_{ICE} is designed as:

$$\begin{array}{rcl} T^*_{ICE}(t) & = & \dfrac{Jv(t)\tau_{\pm}}{X_{p1}(t)} + X_{p2}(t) \\ v(t) & = & \ddot{x}^*_1(t+h) + \lambda_2(\dot{x}^*_1(t+h) - \dot{X}_{p1}(t)) + \lambda_1(x^*_1(t+h) - X_{p1}(t)) \\ & & +\lambda_0 \int_0^t (x^*_1(\iota+h) - X_{p1}(\iota))d\iota \end{array} \tag{4.29}$$

where λ_0, λ_1 and λ_2 are tuning parameters defined hereafter.

Substituting the control (4.29) into the reduced model (4.20), the compensated slow dynamic becomes:

$$\begin{array}{rcl} \dot{X}_{p1}(t) & = & \frac{1}{J}(X_{p2}(t) - \dfrac{\Omega_{M1}(t+h)\,T^*_{M1}(t+h) + P_{l1}(t+h) + i_{aux}(t+h)\,x^*_3(t+h)}{X_{p1}(t)} \\ & & -\dfrac{P_{l2}(t+h)}{X_{p1}(t)} - T_r(t+h)) \\ \dot{X}_{p2}(t) & = & J(\dddot{x}^*_1(t+h) + \lambda_2\dot{\tilde{X}}_{p1}(t) + \lambda_1\tilde{X}_{p1}(t) + \lambda_0 \int_0^t \tilde{X}_{p1}(\iota)d\iota) \end{array} \tag{4.30}$$

with the error $\tilde{X}_{p1}(t) = x^*_1(t+h) - X_{p1}(t)$. By taking into account that its dynamic must be very slow, T^*_{ICE} is considered as a slow input and has only a slow effect on the convergence of the dynamic (4.30).

Note that the error $\tilde{X}_{p1}(t)$ satisfies:

$$\dddot{\tilde{X}}_{p1}(t) = -\lambda_2\,\ddot{\tilde{X}}_{p1}(t) - \lambda_1\,\dot{\tilde{X}}_{p1}(t) - \lambda_0 \int_0^t \tilde{X}_{p1}(\iota)d\iota + \frac{1}{J}\frac{\partial}{\partial t}\Psi(t) \tag{4.31}$$

with $\Psi(t) = \dfrac{\Omega_{M1}(t+h)\,T^*_{M1}(t+h) + P_{l1}(t+h) + i_{aux}(t+h)\,x_3(t+h) + P_{l2}(t+h)}{X_{p1}(t)}$
$+ T_r(t+h)$.

Thus, the tuning choice of λ_0, λ_1 and λ_2 is made such that the polynomial function $s^3 + \lambda_2 s^2 + \lambda_1 s + \lambda_0$ is Hurwitz and guarantees the desired slow dynamics in (4.30).

In our case, the flywheel J is designed sufficiently large with respect to the time derivative of the demand and the losses $\frac{\partial}{\partial t}\Psi(t)$, therefore, for λ_0, λ_1 and λ_2 sufficiently large, $\frac{\partial}{\partial t}\frac{\Psi(t)}{J}$ can be considered close to zero almost everywhere.

4.3 Electrical power and mechanical torque losses estimation

In this section, an estimation approach is proposed to capture the electrical power and mechanical torque losses in real-time (online estimation). The Input-Output Injection observer is used to achieve the objective [KI83], [KR85].

4.3.1 Input-Output Injection Observer

The system under consideration is recalled:

$$\begin{aligned}
\dot{x}_1(t) &= \frac{1}{J}(x_2(t) + \frac{i^*_{M2}(t)\,x_3(t)}{x_1(t)} - \frac{P_{l2}(t)}{x_1(t)} - T_r(t)) \\
\dot{x}_2(t) &= \frac{x_1(t)\,(T^*_{ICE}(t-h) - x_2(t))}{\tau_{\pm} - \dfrac{\tau_- - \tau_+}{2}\,sign(T^*_{ICE}(t-h) - x_2(t))} \\
\dot{x}_3(t) &= \frac{1}{C}(-i^*_{M2}(t) - \frac{T^*_{M1}(t)\,\Omega_{M1}(t)}{x_3(t)} - \frac{P_{l1}(t)}{x_3(t)} - i_{aux}(t))
\end{aligned} \tag{4.32}$$

The first and third states dynamic of system (4.32) are considered where the electrical power (P_{el}) and mechanical torque (T_{ml}) losses are being considered as constant states variables

$$\begin{aligned}
\dot{x}_1(t) &= \frac{1}{J}(x_2(t) + \frac{i^*_{M2}(t)\,x_3(t)}{x_1(t)} - T_{ml}(t)) \\
\dot{T}_{ml}(t) &= 0 \\
\dot{x}_3(t) &= \frac{1}{C}(-i^*_{M2}(t) - \frac{T^*_{M1}(t)\,\Omega_{M1}(t)}{x_3(t)} - \frac{P_{el}(t)}{x_3(t)}) \\
\dot{P}_{el}(t) &= 0
\end{aligned} \tag{4.33}$$

where $T_{ml}(t) = \dfrac{P_{l2}(t)}{x_1(t)} + T_r(t)$ and $P_{el}(t) = i_{aux}(t)x_3(t) + P_{l1}(t)$.

The goal is to estimate (P_{el}) and (T_{ml}) by considering the speed $x_1(t) = \Omega(t)$, the torque $x_2(t) = T_{ICE}(t)$, the DC bus $x_3(t) = U_{DC}(t)$, the traction torque $T^*_{M1}(t)$ and the current $i^*_{M2}(t)$ as outputs-inputs measurements.
Consequently, the system (4.33) can be written in the Input-Output Injection form [KI83]

$$\begin{aligned} \dot{Z}_1 &= A_1 Z_1 + \psi_1(y,u) \\ y_1 &= C_1 Z_1 \end{aligned} \tag{4.34}$$

where $Z_1 = [x_1(t);\, T_{ml}]^T$, $A_1 = \begin{pmatrix} 0 & -\dfrac{1}{J} \\ 0 & 0 \end{pmatrix}$,

$\psi_1(y,u) = \begin{pmatrix} \dfrac{x_2(t) + i^*_{M2}\dfrac{x_3(t)}{x_1(t)}}{J} \\ 0 \end{pmatrix}$ and $C_1 = [1;\, 0]$;

$$\begin{aligned} \dot{Z}_2 &= A_2(y) Z_2 + \psi_2(y,u) \\ y_2 &= C_2 Z_2 \end{aligned} \tag{4.35}$$

where $Z_2 = [x_3(t);\, P_{el}]^T$, $A_2(y) = \begin{pmatrix} 0 & -\dfrac{1}{C\,x_3(t)} \\ 0 & 0 \end{pmatrix}$, $\psi_2(y,u) = \begin{pmatrix} \dfrac{-i^*_{M2}(t) - \dfrac{T^*_{M1}(t)\Omega_{M1}(t)}{x_3(t)}}{C} \\ 0 \end{pmatrix}$

and $C_2 = [1;\, 0]$.

By applying the Kalman criterion, it can be remarked that system (4.34) and (4.35) are observable, since the rank of $\begin{pmatrix} C_i \\ C_i A_i \end{pmatrix}$, $i = 1, 2$, is equal to 2, with $x_3(t) \geq U_{min}$ for system (4.35). Then, an observer can be designed for systems (4.34) and (4.35) as:

$$\begin{aligned} \dot{\hat{Z}}_i &= A_i \hat{Z}_i + \psi_i(y,u) + G_i C_i (Z_i - \hat{Z}_i) \\ \hat{y}_i &= C_i \hat{Z}_i, \quad i = 1, 2 \end{aligned} \tag{4.36}$$

where $\hat{Z}_1 = [\hat{x}_1(t); \hat{T}_{ml}]^T$, $\hat{Z}_2 = [\hat{x}_3(t); \hat{P}_{el}]^T$ and $G_i = [G_{i1}; G_{i2}]^T$ is the gain of the corresponding observer.

4.3.2 Observer convergence

Let us define the estimation error as: $e_{i0} = Z_i - \hat{Z}_i$. The related dynamics is given by

$$\dot{e}_{i0} = (A_i - G_i C_i) e_{i0} \tag{4.37}$$

Proposition 2 *Consider systems* (4.34) *and* (4.35)*. Then, system* (4.36) *is an exponential observer for systems* (4.34) *and* (4.35)*, for* G_{i1} *and* G_{i2} *sufficiently large.*

Proof 2 *To achieve the exponential stability of the error (4.37), the gains* G_{i1} *and* G_{i2} *are assigned by a pole placement:* $det[(A_i - G_i C_i) - \Lambda] = \Lambda^2 + 2m\omega_0\Lambda + \omega_0^2$*. The estimation leads to:*

$$G_1 = [2\,m\,\omega_0 \;\; -\omega_0^2\,J]^T, \quad G_2 = [2\,m\,\omega_0 \;\; -\omega_0^2\,C\,x_3]^T. \tag{4.38}$$

There exists a positive definite symmetric matrix P_i *which satisfies*

$$P_i(A_i - G_i C_i) + (A_i - G_i C_i)^T P_i = -Q_i$$

where Q_i *is a definite positive matrix. The derivative of the quadratic function*

$$V_{i0} = e_{i0}^T\, P_{ie}\, e_{i0}$$

along solutions of (4.37) satisfies

$$\dot{V}_{i0} = -e_{i0}^T\, Q_i\, e_{i0}.$$

This result implies that the error equation (4.37) *converge uniformly exponentially to zero for* e_{10} *and for* e_{20} *only exponentially to zero for* $x_3(t) \geq U_{min}$*.*

4.4 Stability analysis of the closed loop system

In order to implement the controls (4.12)-(4.29), the controls $T^*_{ICE}(t)$ (4.29) and $i^*_{M2}(t)$ (4.12) remains the same, the losses (P_{el}) and (T_{ml}) are replaced in (4.27) by their estimates

resulting in the predictor

$$X_p(t) = e^{Ah}X(t) + \int_0^h e^{A(h-s)}BT^*_{ICE}(t-h+s)\mathrm{d}s + \int_0^h e^{A(h-s)}d(t+s)\mathrm{d}s \tag{4.39}$$

with $A = \begin{bmatrix} 0 & \frac{1}{J} \\ 0 & -\frac{x_1(t)}{\tau_\pm} \end{bmatrix}$, $B = \begin{bmatrix} 0 \\ \frac{x_1(t)}{\tau_\pm} \end{bmatrix}$ and $d(t) = \begin{bmatrix} -\frac{\Omega_{M1}(t)\,T^*_{M1}(t) + \hat{P}_{el}(t)}{x_1(t)\,J} - \frac{\hat{T}_{ml}(t)}{J} \\ 0 \end{bmatrix}$.

Where $(\hat{P}_{el})$ and $(\hat{T}_{ml})$ are given by observers (4.36).

Theorem 2 *Consider system* (4.9) *controlled by* (4.12) *and* (4.29)*. Then there exists observer gains* G_1 *and* G_2 *of* (4.36) *that guaranty the practical stability of system* (4.9) *under the cation of the observer based control.*

Proof 3 *The proof follows from singular perturbation argument because observer gains* G_1 *and* G_2 *of* (4.36) *are selected such that the observer dynamic is largely faster than mechanical dynamic* (4.28)*. Since the dynamic of* $i^*_q(t)$ (4.12) *is not affected by losses estimations (*$\hat{P}_{el}$ *and* $\hat{T}_{ml}$*), it is not necessary to have observer gains faster than this electrical dynamic*

Remark 12 *For simplicity, the observer and electrical speeds (eigenvalues) dynamics can be chosen closer.*

4.5 Summary

Contributions

— Singular perturbation approach used for studying the selected strategy.
— State observer employed for estimating the power losses.

Chapter 5

Power management

5.1 Introduction

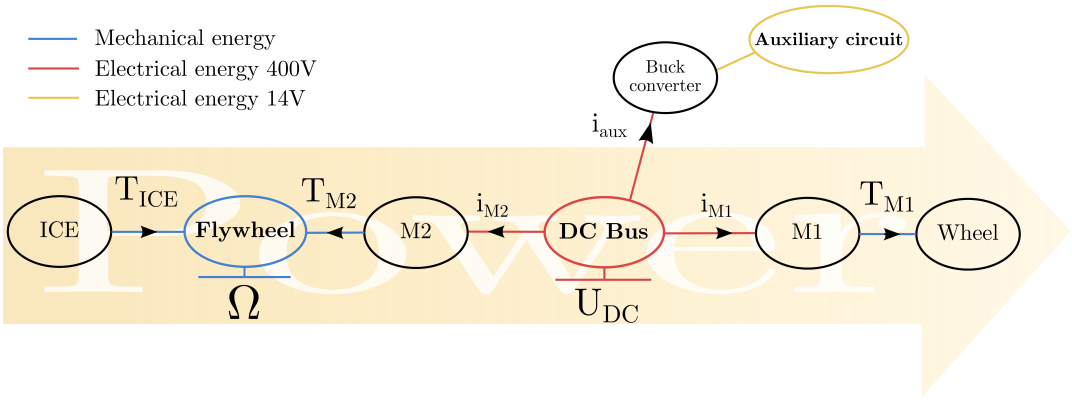

Figure 5.1 – Global Architecture

In this chapter, a power management that will provide the references for the flywheel rotational speed and the DC bus voltage is proposed. The principal aim behind the power management is to deal with the saturation of each element of the hybrid serial vehicle figure 5.1 and find the best references that will realize the driver demand. The driver demand is here the accelerator pedal, it has to somehow correspond to the torque demand on the M1.

In the serial hybrid vehicle, the power goes from the ICE to the M1. The ICE produces mechanical power by burning the fuel, the M2 converts this power into electrical power and the M1 uses this power to tract the vehicle. Between the ICE and the M2, a flywheel acts as a storage of mechanical energy. Between the M2 and the M1, a capacitor acts as a storage of electrical energy. In this configuration, the flywheel and the capacitor are the key to maintain the power transmission needed to realize the user demand. The physical value of the voltage and the rotational speed representing the level of energy storage that each buffer has.

Figure 5.2 shows the different constraint that the power management has to overcome to take the fullest advantage of the system. Firstly, the maximum power consumption of the M1 has to meet the maximum power produced by the M2, minus the possible perturbation. Secondly, the M2 maximum power production depends on the voltage bus and the rotational speed of the flywheel. Thirdly, the ICE maximum power production also depends on the rotational speed. Thus, to get the maximum power for the M1, the system has to be inside the constraint of each element. Moreover, the power production dynamic is limited by the slow dynamic of the ICE.

The next section will present:

— the car modeling,
— the torque saturation of the M1, the M2 and the ICE,
— the proposed power management,
— the respond of a step demand.

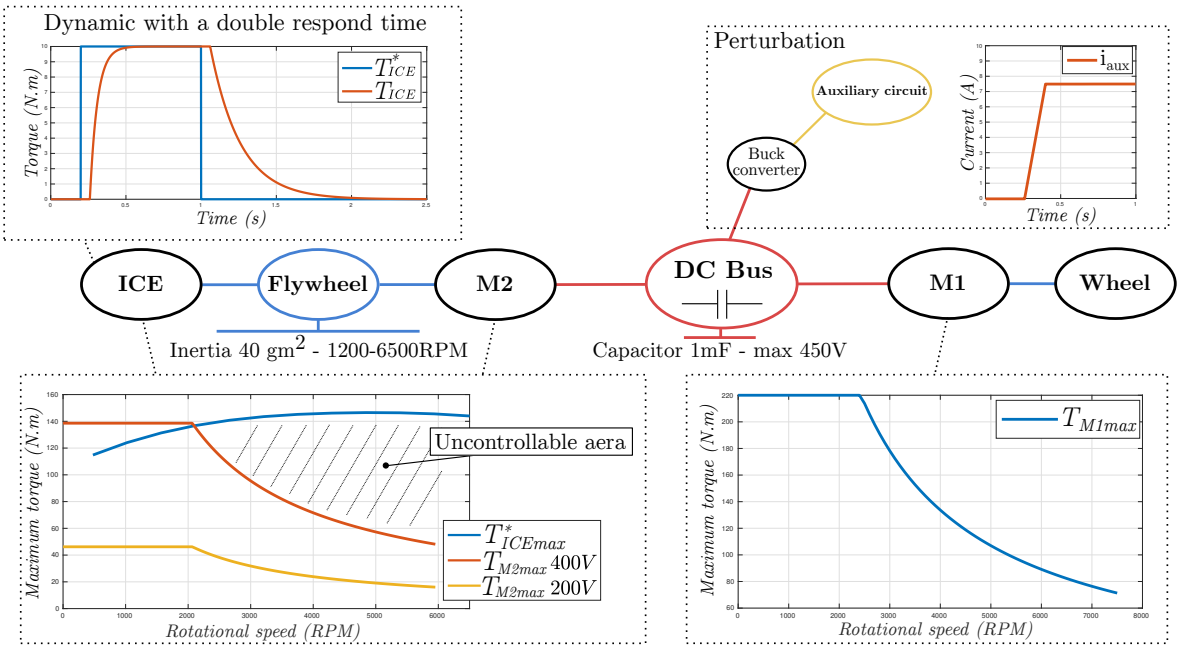

Figure 5.2 – Usage domain and constraint for the serial hybrid vehicle

5.2 Car modeling

The car modeling is simplified as possible. It only involves the inertia J_{M1}:

$$\dot{\Omega}_{M1}(t) = \frac{T_{M1}(t)}{J_{M1}} \tag{5.1}$$

The inertia is linked to the car mass m_{car} by the wheel radius r_{wheel} and the reduction ratio of the gearbox $R_{gearbox}$ such that:

$$J_{M1} = m_{car} \frac{r_{wheel}^2}{R_{gearbox}^2} \tag{5.2}$$

Also, the vehicle speed V_{car} is given by:

$$V_{car} = 3.6\,\Omega_{M1} \frac{r_{wheel}}{R_{gearbox}} \tag{5.3}$$

The various units used in the equations are: Ω_{M1} in rad/s, r_{wheel} in m, V_{car} in km/h, m_{car} in kg, J_{M1} in $kg.m^2$. Note that, the rotational speed is displayed in RPM and not in rad/s for the simulation reading.

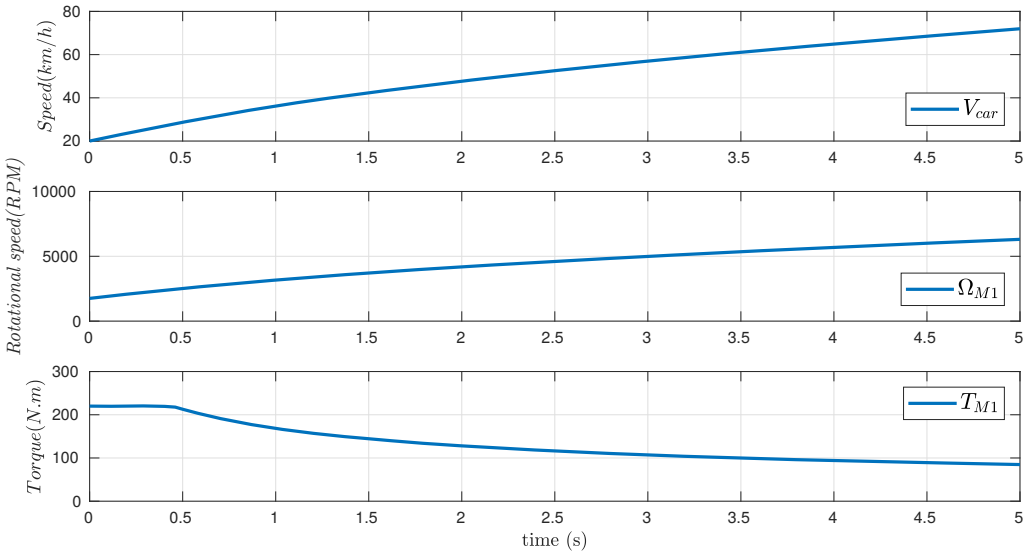

Figure 5.3 – Simulation with the maximum torque delivered by the M1, the mass of the car is 1500kg

5.3 The saturation constraint and efficiency

In this section, the maximum torques and the efficiencies of the M2 and the ICE are shown. As well as the maximum torque is shown for the M1.

5.3.1 The ICE and M2 torque saturation

The quasi-static model of the ICE comes from the book [GS13] and has been adapted to the company engine. The quasi-static model describes the efficiency and the maximum torque of the ICE. The M2 maximum torque comes from the manufacturer specification and the efficiency is derived from the offline optimization presented in the section 2.4.

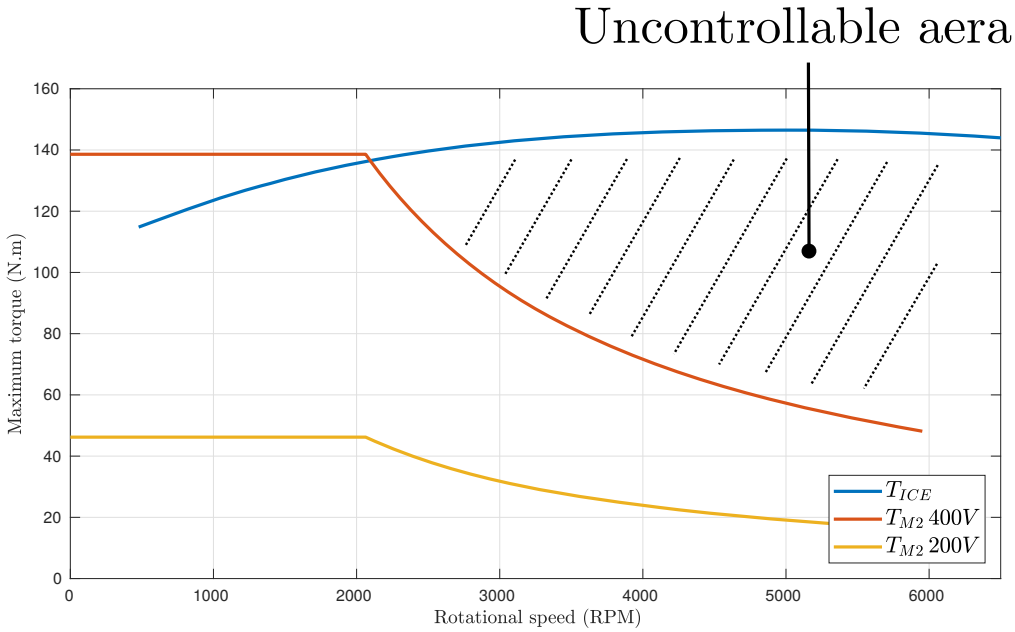

Figure 5.4 – The ICE and M2 maximum torques

The maximum torques of the ICE and the M2 are shown on figure 5.4. The ICE produces the maximum torque around $4500RPM$ and his maximum power $80kW$ around $5500RPM$. In the same figure, the maximum torque for the M2 is displayed for a DC bus at $200V$ and $400V$. The torque is limited by the maximum torque value below $2100RPM$. Above this rotational speed, the torque is limited by the maximum power of the M2. For a DC bus at $200V$, the maximum power reaches $10kW$ and at $400V$ the maximum power is $30kW$.

On figure 5.4, it appears an uncontrollable area. This region represents an unstable

area. If the ICE produces more torque than the maximum torque that the M2 can absorb. Then, the rotational speed increases moving the operation point to higher RPM. This will decrease the M2 maximum torque. At this point, if the ICE torque is not cut. Then this phenomenon will rapidly increase the torque difference $T_{ICE} - T_{M2}$, resulting in an uncontrollable acceleration of the rotational speed.

5.3.2 The ICE and the M2 efficiencies

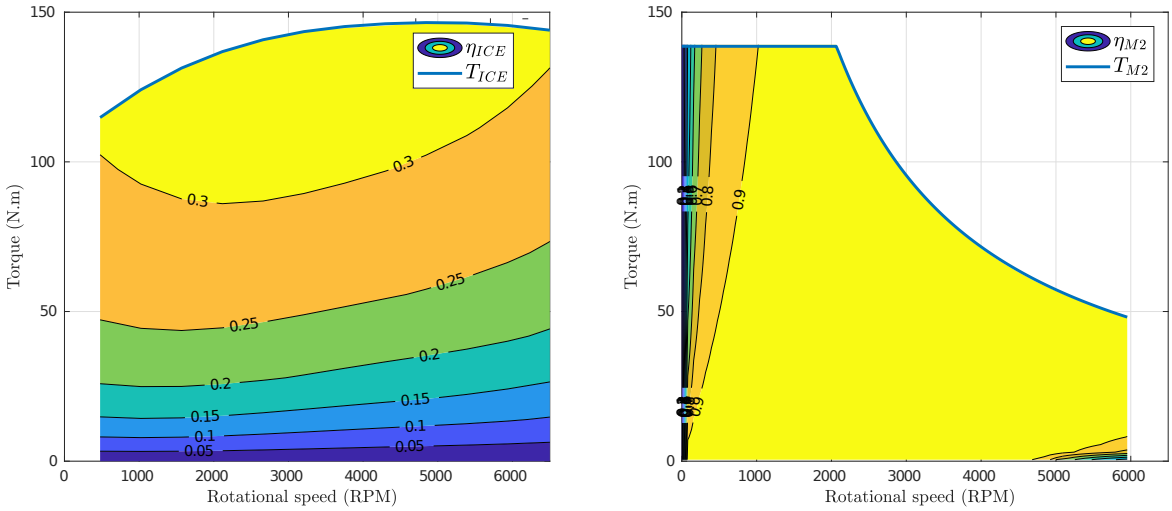

Figure 5.5 – The quasi-static model of the ICE and M2 showing the maximum torques and the efficiencies. Left: the ICE characteristic – Right: the M2 characteristic

Below the maximum torque produced by the ICE, the efficiency is displayed in figure 5.5-left. Note that, the region with the higher efficiency is under 40% and around the maximum torque. For the M2, the efficiency is shown on figure 5.5-right. The electric motor is much efficient than the internal combustion engine. The efficiency area above 90% covers the majority of the operating point. Nevertheless, the efficiency declined with lower rotational speed and arrived at 0% for $0RPM$. At low torque and high RPM, the efficiency is also decreasing due to the de-fluxing of the PMSM.

Moreover, the ICE and M2 efficiencies are combined in figure 5.6. The combination of the ICE and M2 efficiencies show the power efficiency from the fuel combustion to the electrical power. This figure shows the most efficient point from the coupling ICE/M2 in order to produce the energy needed for the M1.

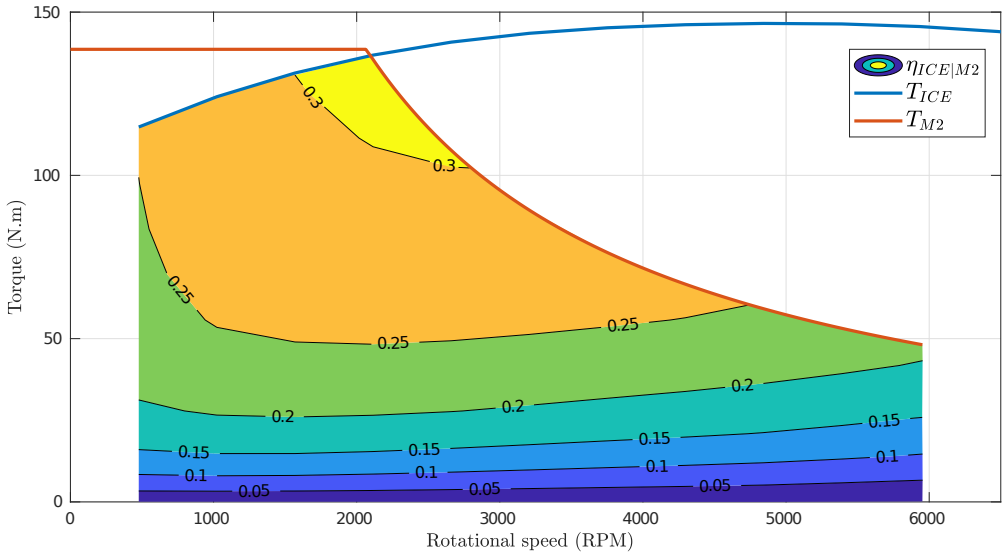

Figure 5.6 – The combination of the ICE and the M2 efficiencies

5.3.3 The M1 saturation

The M1 saturation is shown on figure 5.7. For the DC bus voltage at $400V$, the torque is limited at $220N.m$ below $1600RPM$ and above $1600RPM$ by the maximum power of $70kW$ that the M1 can produce.

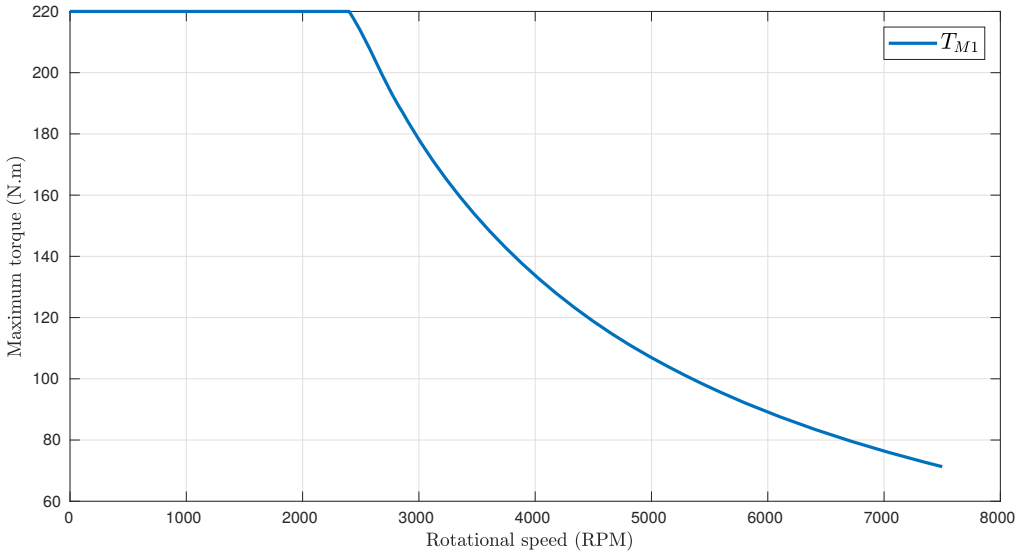

Figure 5.7 – The M1 maximum torque

5.4 The power management

In this section, the power management is in charge of attributing the rotational speed reference and the voltage bus reference for lower level of strategies developed in the section 3.3 and recalls in figure 5.8. In the sequel, the operating area of the M1 is divided in different region. The attribution of the voltage is explained, as well as the rotational speed.

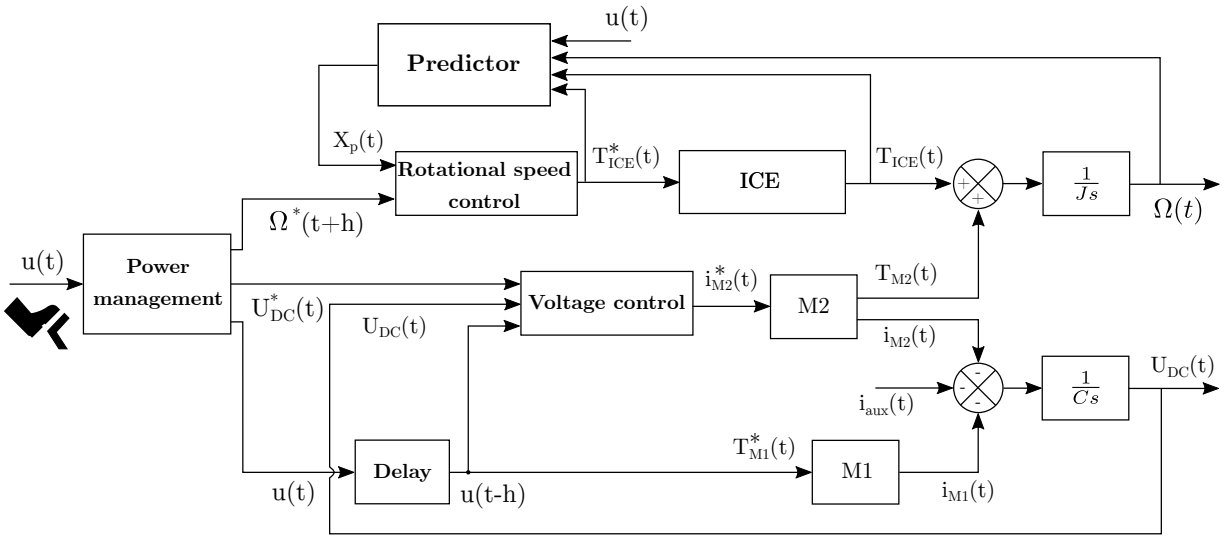

Figure 5.8 – Power management with the first strategy

5.4.1 The operating area of the M1

See figure 5.9, the M1 operating area is enclosed by: the saturation of the M1 motor and the maximum power available on the DC bus. The M2 can deliver $30kW$. The perturbation from the auxiliary can consume $3kW$. Thus, when the perturbation occurs, the power available for the M1 is reduced at $27kW$.

Thus the operating area can be divided in three region by the following condition:

if $\Omega_{M1} < 1200RPM$ (1)
$0 < T_{M1} < 220N.m$
else if $P_{M1} < 27kW$ (2)
$0 < T_{M1} < 27kw/\Omega_{M1}$
else if $P_{M1} < 30kW$ (3)
$27kw/\Omega_{M1} < T_{M1} < 30kW/\Omega_{M1}$

On figure 5.9, the area 1 is limited by the maximum torque $220N.m$ and $1200RPM$, this area corresponds at the M2 can produce enough power and the M1 saturation limit the traction power. The area 2 corresponds at the region above $1200RPM$ and below the iso-power curve of $27kW$. It is the region, if the perturbation occur, the M2 limit the maximum power for the traction. The area 3 corresponds at the last part of the operating point accessible, if the perturbation doesn't occur. It is situated below the M2 maximum power that is $30kW$.

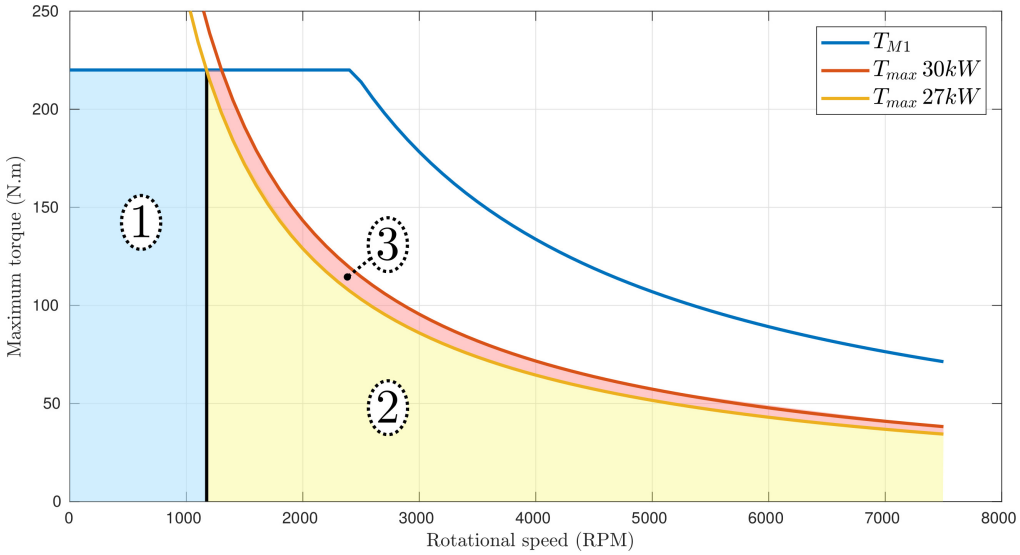

Figure 5.9 – The operating area of the M1 enclosed by the M1 maximum torque, the iso-power curve of $27kW$ and $30kW$.

In practice, the operating point is kept in the area 1 and 2. Thus, if the perturbation occurs, the M2 and ICE can produce the power needed by the auxiliary circuit. That is, if the system is attended to work in area 3, the power needed by the auxiliary circuit has to be deduced from the traction power because the M2 cannot provide it.

5.4.2 The DC bus reference

From the characteristic of the M2, recalled on figure 5.10, the M2 is able to produce more power with higher voltage. But, the capacitor placed on the DC bus is rated at the maximum voltage of $450V$ and a security of $50V$ ensures some room before damaging it. Thus, the DC bus voltage reference is chosen to be $400V$. The tradeoff made with a

constant voltage reference is that the losses in the inverter are greater with higher voltage than needed. If the aim was to minimize the inverter losses, the strategy would have to choose the lowest voltage for the power production. Nevertheless, the inverter losses can be compromised in front of the constant voltage and safety.

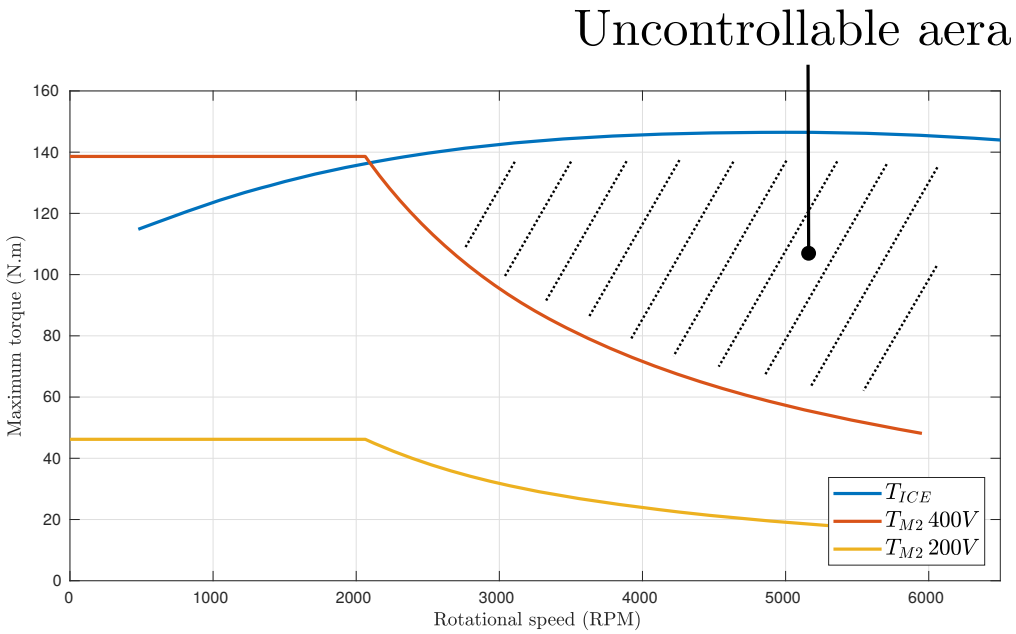

Figure 5.10 – The ICE and M2 maximum torque

5.4.3 The rotational speed reference

In order to attribute the best rotational speed for the flywheel, the idea is to choose a linkage curve between the most efficient point producing the maximum power out of the M2 and the zero power point located on the minimal rotational speed. On figure 5.11, the combination of the ICE and M2 efficiencies is recalled and it can be seen that the best efficiency point producing $P_{M2max} = 30kW$ is around $\Omega_{max} = 2300RPM$ and $T_{M2max} = 120N.m$. Also, the zero power point is around the minimum speed at $\Omega_{min} = 1000RPM$. From these two points a straight line presents the benefit to be simple to implement and follow the best efficiency point. Thus, it has been chosen for the rotational speed reference. This straight line is defined by:

$$T^*_{M2} = \frac{\Omega^* - \Omega_{min}}{\Omega_{max} - \Omega_{min}} T_{M2max} \tag{5.4}$$

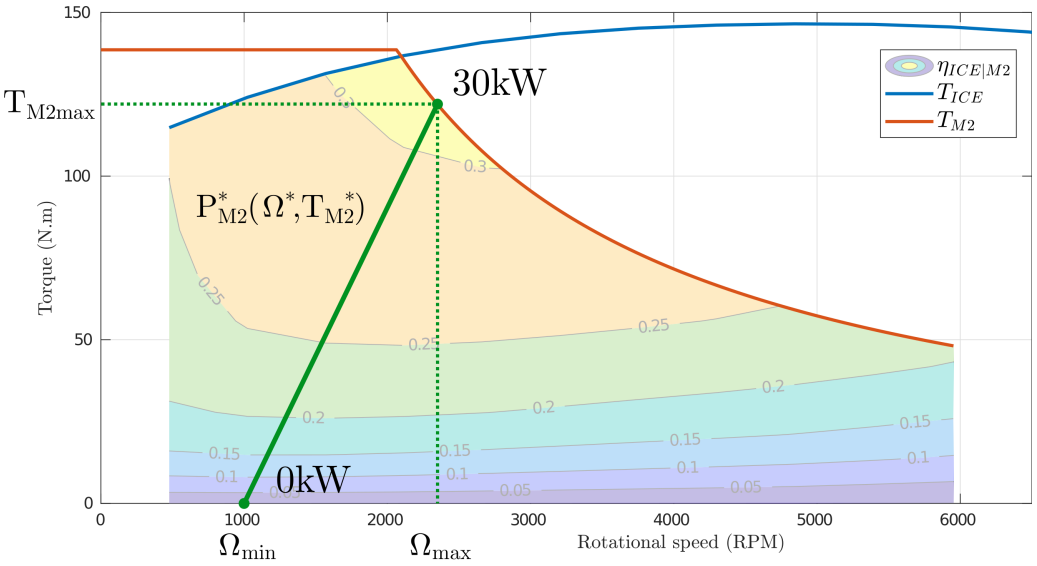

Figure 5.11 – The ICE and M2 maximum torque and efficiencies with the rotational speed reference

The power produced by the M2 being:

$$P^*_{M2} = T^*_{M2}\,\Omega^* \tag{5.5}$$

The rotational wheel reference is:

$$\Omega^* = \frac{\Omega_{min} + \sqrt{4\,P^*_{M2}\,\Omega_{max}(\Omega_{max} - \Omega_{min}) + \Omega^2_{min}}}{2} \tag{5.6}$$

Thus, from the power reference needed by the traction, the appropriate rotational speed is chosen for the ICE. The strategy proposed here is simple, easily adjustable and can be used for a complex curve minimizing the quasi-static power losses. The method for choosing the parameter can be adapted to different motor without difficulty.

5.4.4 Power management simulation

The simulation is conducted with the strategy 1 developed in the previous and recall in figure 5.12.

With the approximation (3.14), the power recall from the M1 is formulated as:

$$P^*_{M2} = T^*_{M2}\,\Omega^* = T^*_{M1}\,\Omega_{M1} = u\,\Omega_{M1} \tag{5.7}$$

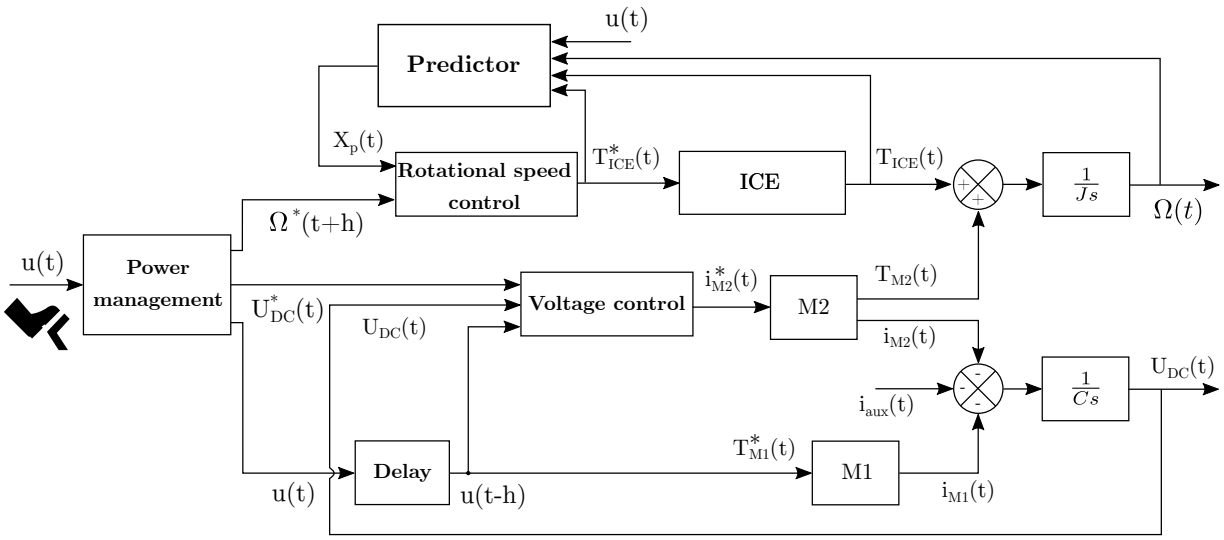

Figure 5.12 – Power management with the first strategy

The first result is shown on figure 5.13. The aim is to deliver 50% of the capability of the M2, i.e. 15kW. Beginning at the rotational speed $\Omega^* = 1000RPM$ and the DC bus voltage at $U^*_{DC} = 400V$. The vehicle speed start at $20km/h$, corresponding to $\Omega_{M1} = 1750RPM$. The user demand represented by the M1 torque goes from 0 to $82N.m$ with a ramp from $t_1 = 0.1s$ to $t_2 = 1.1s$.

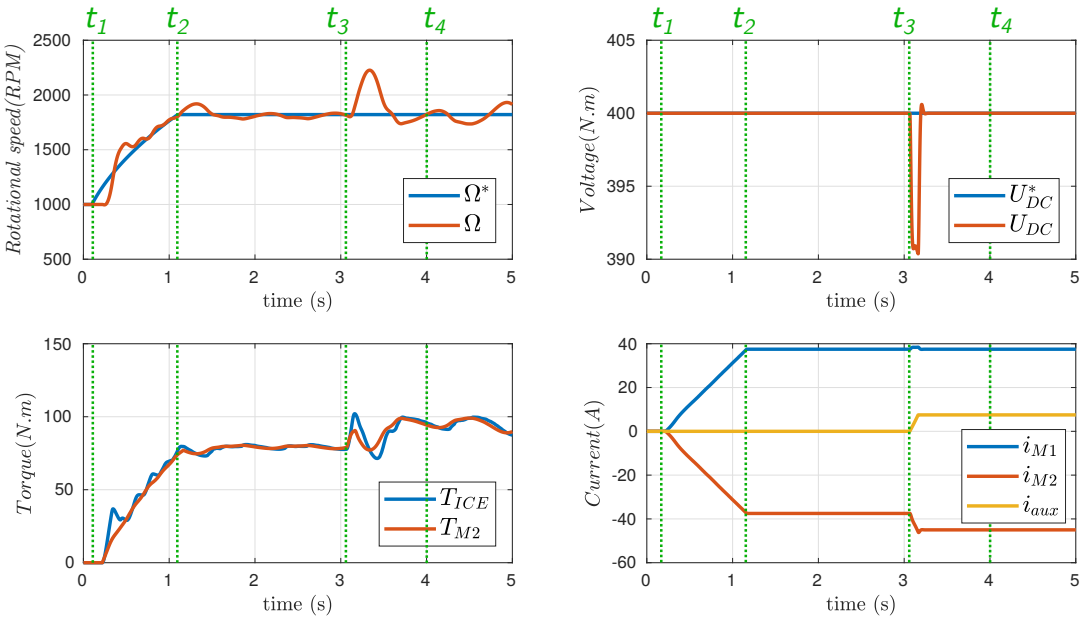

Figure 5.13 – Simulation at 50% of the M2 capability with an instantaneous disturbance $i_{aux} = 7.5A$ at $t_3 = 3.1s$

On the bottom left of the figure, the torque of the M2 follows the ICE torque. On the bottom right of the figure, the current of the M2 follows the consumption of the M1. Except at $t_3 = 3.1s$, when the auxiliary circuit disturbs the DC bus, it consumes $0A$ at $t_3 = 3.1s$ to $7.5A$ in $100ms$. It can be seen that the current i_{M2} produces by the M2 increase. On the top of the figure, the simulation shows some oscillation on the rotational speed Ω, a part is due to the double constant $\tau_{\pm}$ of the ICE. The voltage U_{DC} is kept around $\pm 10V$.

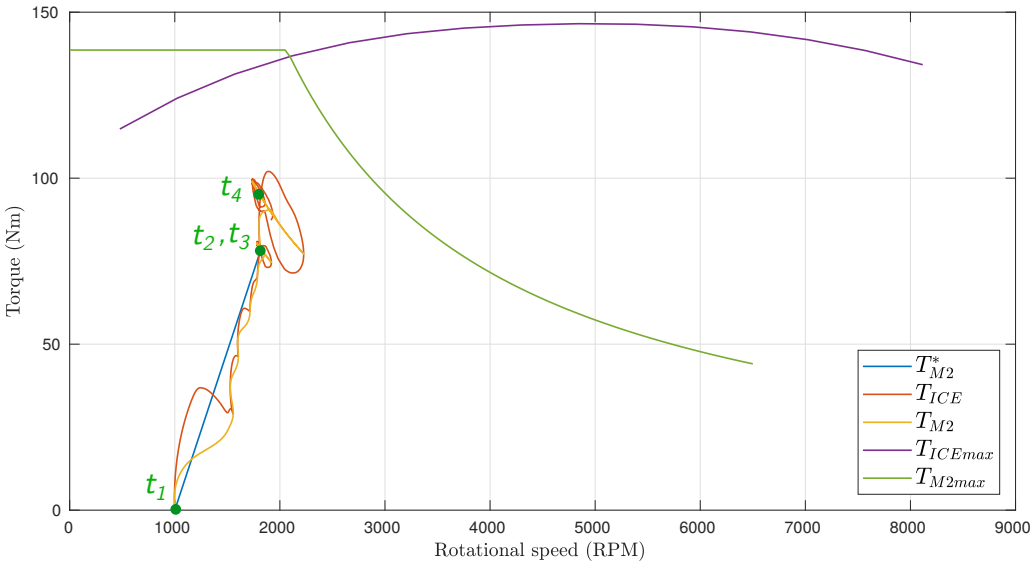

Figure 5.14 – Operating of the ICE and M2 at 50%

On figure 5.14, the operating point (Ω, T) of the simulation is shown. The figure illustrates the trajectory of the ICE, the M2 and also their torque saturation. It can be seen that the ICE and M2 begin at the point $(1000RPM, 0N.m)$ and follows the reference to $(1800RPM, 78N.m)$. When the auxiliary circuit disturbs the DC bus, the operating point moves to higher torque $t_4 = (1800RPM, 98N.m)$ in order to compensate the consumption from the auxiliary circuit.

The second simulation shows the case where the power demand is higher than the capacity of the M2. The simulation is shown on figure 5.15, the aim is to deliver 100% of the capability of the M2, i.e. 30kW. Beginning at the rotational speed $\Omega^* = 1000RPM$ and the DC bus voltage at $U^*_{DC} = 400V$. The vehicle speed start at $20km/h$ corresponding to $\Omega_{M1} = 1750RPM$. The user demand represented by the M1 torque goes from 0 to $164N.m$ with a ramp from $t_1 = 0.1s$ to $t_2 = 2.1s$.

The current of the M2 follows the consumption of the M1. Except at $t_3 = 3.1s$, when

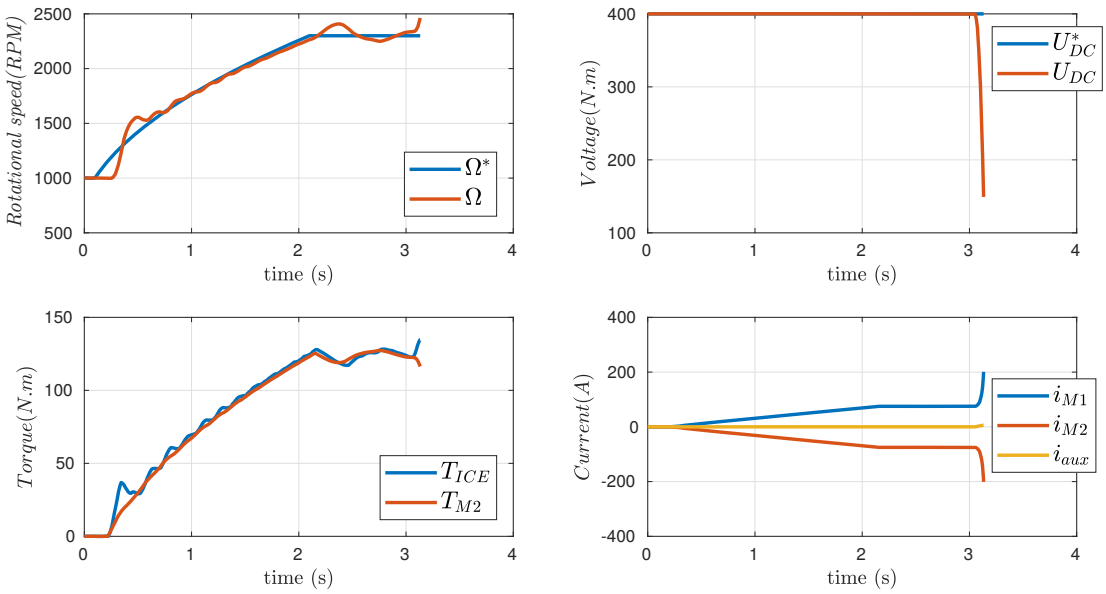

Figure 5.15 – Simulation at 100% of the M2 capability with an instantaneous disturbance $i_{aux} = 7.5A$ at $t_3 = 3.1s$

the auxiliary circuit disturbs the DC bus, it consumes $0A$ at $t_3 = 3.1s$ to $7.5A$ in $100ms$. It can be seen that the voltage bus U_{DC} rapidly decreases and the simulation is stopped.

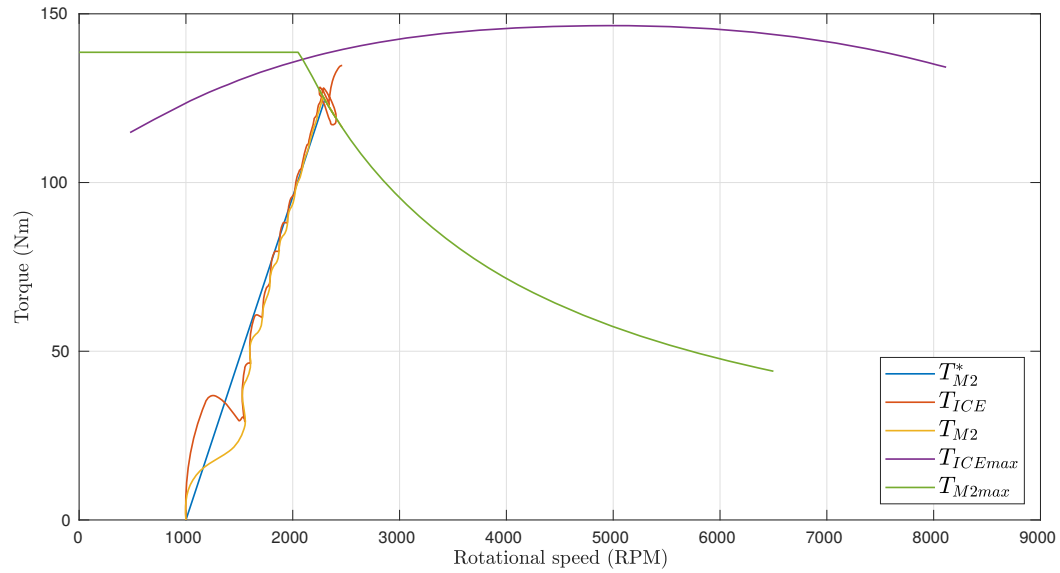

Figure 5.16 – Operating of the ICE and M2 at 100%

On figure 5.16, the operating point (Ω, T) of the simulation is shown. The figure illustrates the trajectory of the ICE, the M2 and also their torque saturation. It can be seen that the ICE and M2 begin at the point ($1000RPM$, $0N.m$) and follows the reference to ($2300RPM$, $140N.m$). When the auxiliary circuit disturbs the DC bus, the operating point of the ICE moves to higher torque in order to compensate the consumption from the auxiliary circuit. But, the M2 torque saturates and the simulation is stopped from the critical voltage. It is due to the M1 demand being $30kW$, placing the operating point the area 3 describes previously. The M2 has a maximum power of $30kW$, when the auxiliary circuit kick on and consumes $3kW$, the DC bus voltage collapse. This case shows the importance to maintain the M1 demand under $27kW$.

5.5 Open loop strategy for a step demand

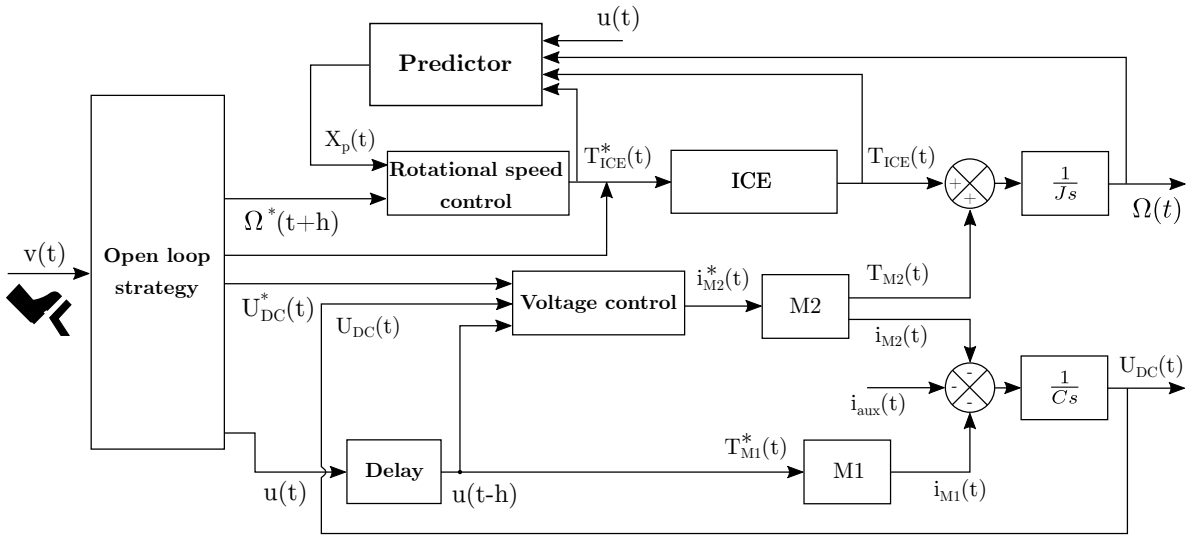

Figure 5.17 – Open loop strategy with the power management

In this section, an open loop method is proposed for a greater time respond from this serial hybrid vehicle. The aim is to open the control loop dedicated to the rotational speed. The loop will be cut, as shown in figure 5.17, in between the control law and the torque reference for the ICE. The idea is to impose the maximum torque demand to the ICE when a high demand occurs from the user. Doing this, the ICE throttle is fully open, the torque will climb as well as the rotational speed of the flywheel. When enough energy is stored in the flywheel, the M1 is switched on from the initial state to the user demand and

the loop is closed. Thus, the user demand is delayed for the time that the ICE torque gets higher and the flywheel gets enough energy before realizing the demand. The dynamic of the M1 can give a better feeling to the user than the slow dynamic of the ICE.

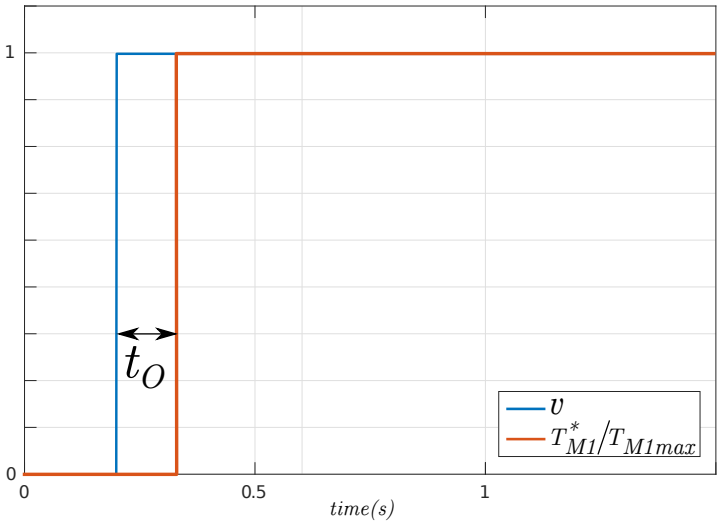

Figure 5.18 – Type of step demand delayed by t_O

On one hand, see figure 5.18, the user demand v consider here is a step demand from 0 to a normalized value:

$$v = \frac{u}{T_{M1max}} = \frac{u\,P_{M2max}}{\Omega_{M1}} \tag{5.8}$$

On the other hand, the torque request $T^*_{M1} = u/T_{M1max}$ for the M1 can be a delayed step of v by t_O.

The open strategy is:

while $t < t_u + t_O$
$T_{M1}(t+h) = 0$
$T_{ICE}(t) = T_{ICEmax}$

otherwise
$T_{M1}(t+h) = T^*_{M1}$
$T_{ICE}(t)$ regul Ω

with the objective to have $0 < t_O < 300ms$ and the time t_u being the instant where the user demand occurs.

A simulation of the open loop strategy is shown in figure 5.19. The aim is to deliver 60% of the capability of the M2. Beginning at the rotational speed $\Omega^* = 1200RPM$

and the DC bus voltage at $U^*_{DC} = 400V$. The vehicle speed starts at $20km/h$. The user demand represented by the M1 torque goes from 0 to $98N.m$ at $0.1s$. The loop opens at $0.1s$ and for $t_O = 220ms$. During this time, the maximum torque is requested to the ICE. After this delay, the M1 realizes the torque demand.

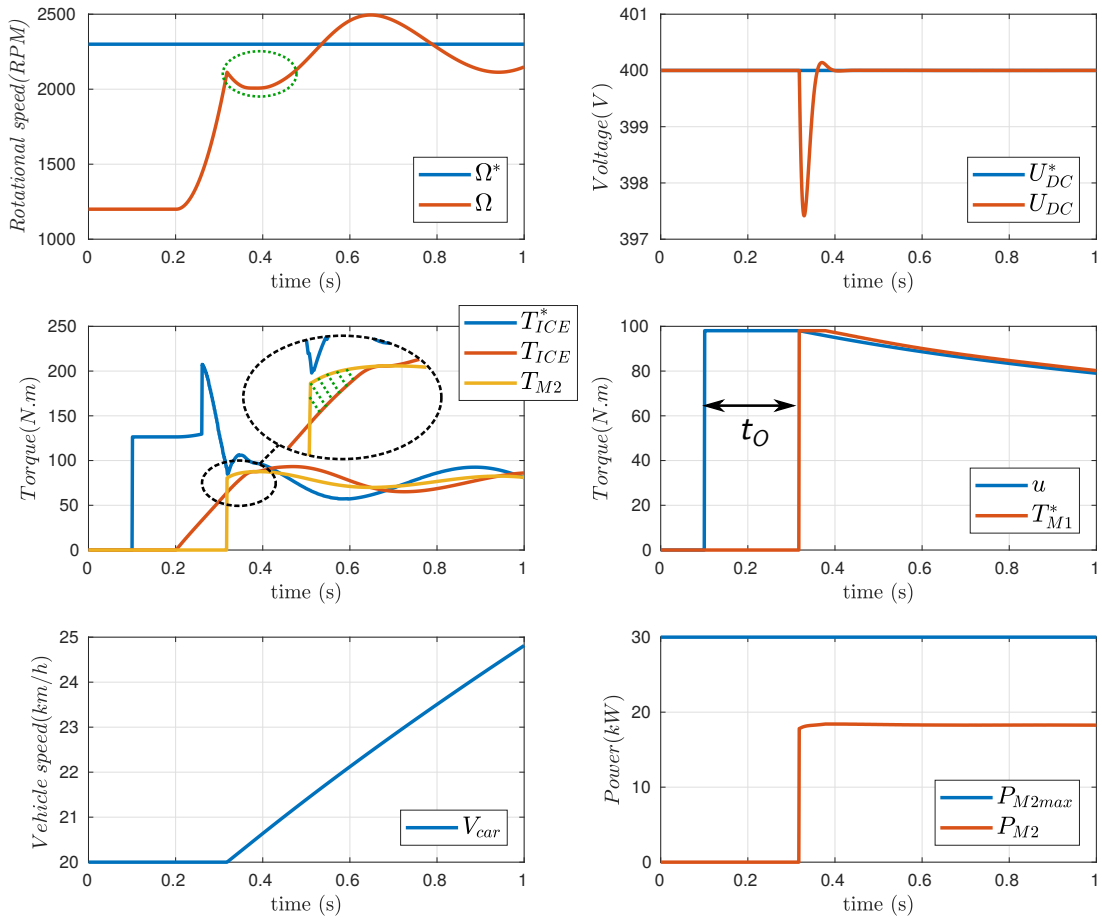

Figure 5.19 – Simulation of the open loop strategy with an open loop delay $t_O = 220ms$

Note the decreasing of the rotational speed (circle in green on the top left of the figure) when the M1 torque occurs. It corresponds to the area where the M2 torque is higher than the ICE torque. It is an instant where the energy is drawn from the flywheel. If the delay t_O is too short. An example is given in the simulation figure 5.20, the delay is $t_O = 210ms$, the rotational speed of the flywheel drops and will conduct to an engine stalling.

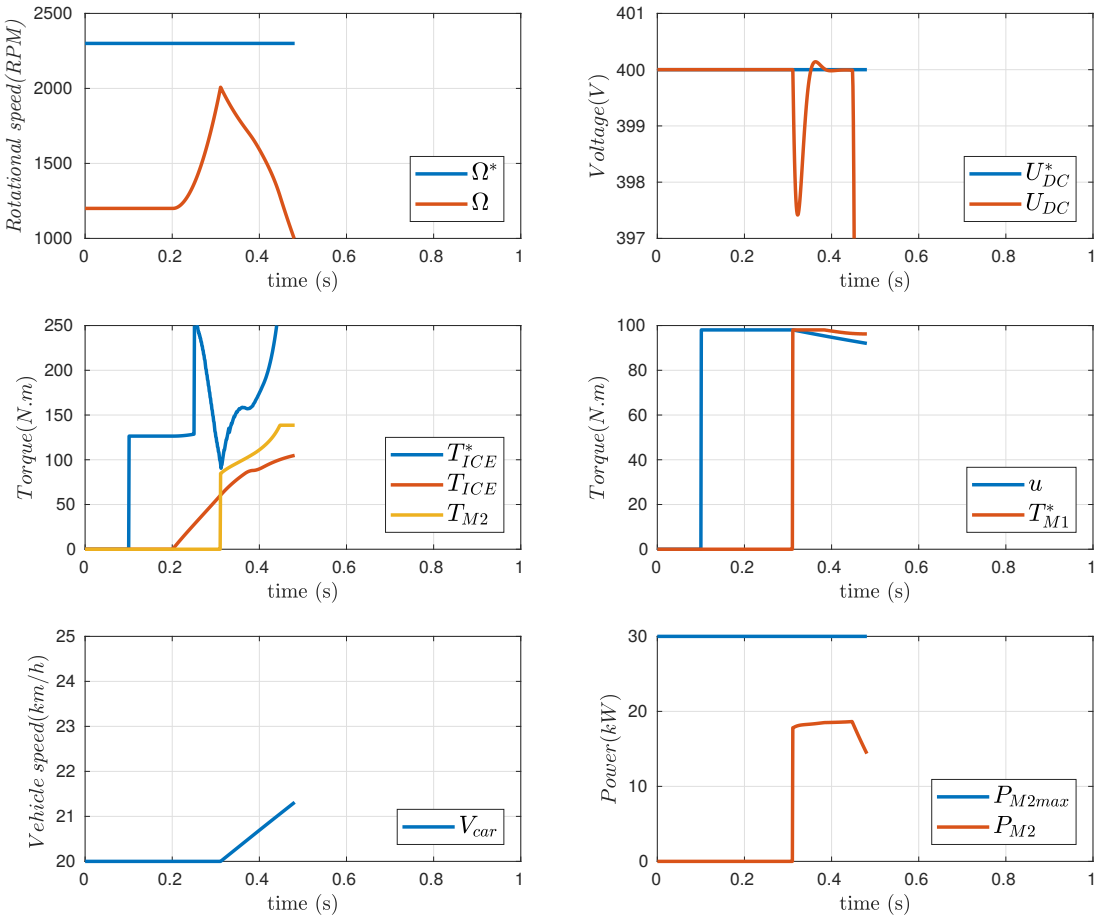

Figure 5.20 – Simulation of the open loop strategy with a to low delay $t_O = 210ms$

Using different user demand and different initial speed of the flywheel, i.e. from 0 to 95% of the maximum power of the M2 and Ω from $1000RPM$ to $3000RPM$. An iterative method has been used to find the minimum delay for each situation. The result is shown on figure 5.21. It can be seen that for lower initial rotational speed the delay is larger as well as for higher user demand the delay is larger. Note that, the delay can be reduced under $50ms$ for low requested demand and above a certain speed.

In this subsection, the open loop strategy has been studied for a step demand and an iterative method has been shown the existence of numerous delay permitting to realize a step demand. This approach can be adapted for ramp and first order respond with simple modification. Thus, this strategy can be extended for a lot of user cases.

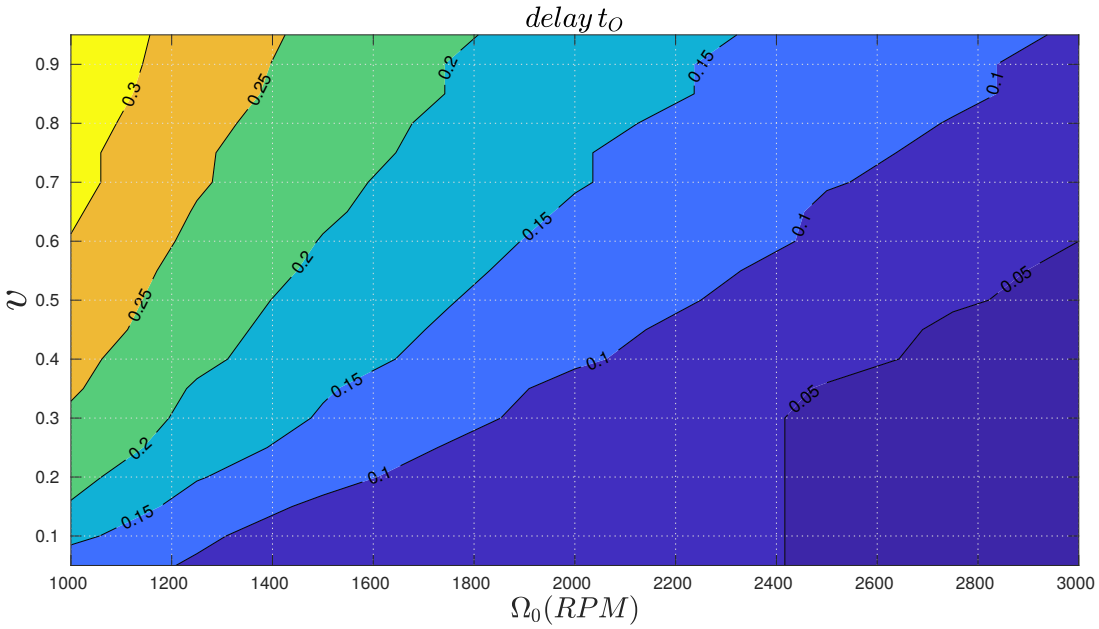

Figure 5.21 – Minimum delay t_O for different user demand and initial rotational speed

5.6 Summary

Contributions

— Presentation of a power management able to realize the user demand and to deal with the saturation of each element of the vehicle.

— Proposition of an open loop strategy for higher performance of the system.

Chapter 6

Validation on a test bench

6.1 Introduction

This chapter presents experimental results achieved by the control algorithm developed in previous chapters. The test bench used for the implementation has been adapted from an available setup existing in the laboratory, see figure 6.1. Numerous PhD thesis and collaboration have been made on this platform. Recently, [Mes19] proposed new observation technique for the angular position and validated the technique on this test bench.

Figure 6.1 – Test Bench

In the next section of this chapter, the constitution and technical specification of the test bench will be discussed and compared to the system presents in the vehicle. After, the current control will be recalled from chapter 2 and applied on the test bench. Then, the

singular perturbation approach presented on chapter 4 will be adapted to the platform modeling and the experimental setup will be used to ascertained the performance achieved with the approach. Lastly, the open strategy presented in chapter 5 will be demonstrated on the platform.

6.2 Constitution and technical specification of the test bench

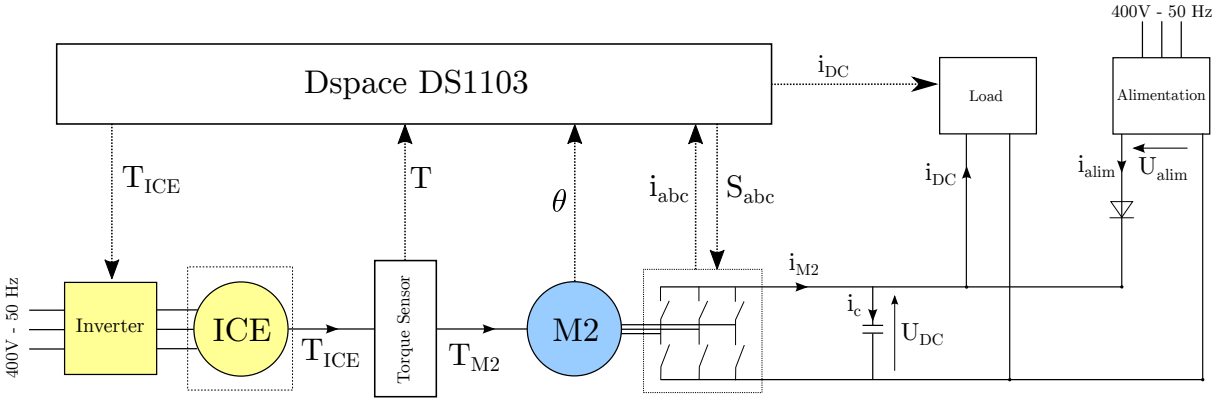

Figure 6.2 – Diagram of the test bench

The test bench is described in figure 6.2. The control is implemented on a solution supplied by dSPACE. The real-time model produced via Matlab/Simulink is compiled and downloaded in the dSPACE board DS1103. Where, the micro-controller inside the board executed the software in real-time. The dSPACE board used: analog to digital converter to acquire the measure needed for the control scheme, 5V TTL signal to control the inverter branch and digital to analog converter to send the required torque to the ICE inverter and current reference to the load. Note that, no internal combustion engine has been used for the experiment. The ICE comportment is simulated in software, see figure 6.3. Thus, the ICE torque is produced by an inverter and a PMSM. In this section, ICE designates the PMSM motor responsible to produce the torque instead of a real internal combustion engine. The ICE motor is an $8\,kW$ SEW synchronous motor with a peak torque of $68.30\,N.m$ and a nominal speed of $3000\,RPM$. The ICE motor is powered by a SEW inverter with a rated power of $5.5\,kW$. This inverter receives and controls the torque of the motor. The resulting torque dynamic is sufficiently fast relative to the ICE dynamic,

such that the software simulation and the PMSM reproduces faithfully the comportment of a real internal combustion engine.

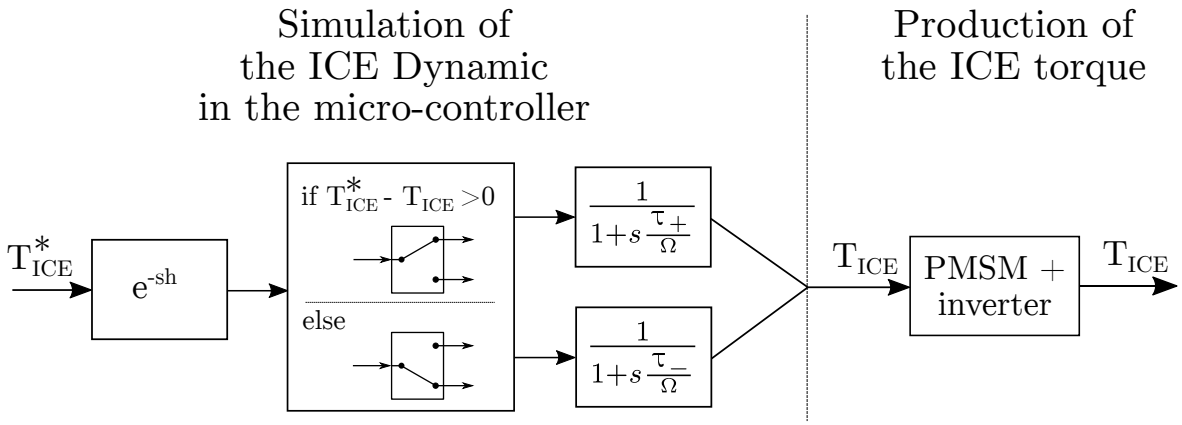

Figure 6.3 – Implementation of the ICE dynamic

A flywheel has been added to the output shaft of the ICE. The added flywheel permits to reach the total desired inertia of $40\,g.m^{-2}$. The flywheel is then coupled to a $50\,N.m$ KTR torque sensor through a joint. On the opposite side of the torque sensor, a Leroy Somer PMSM has been connected through a second joint. This motor is the M2 in figure 6.2. His nominal power is $3kW$ and its maximum speed is $4000RPM$. The Leroy Somer motor is provided with an optical encoder that presents 4096 pulses per revolution. The inverter connected to the M2 is made by ARCEL and can sustain $120A$ and $1200V$. The DC bus of the inverter has been modified to only have a $1\,mF$ capacitor. The DC bus can be powered by a $6kW - 500V$ Micronics power supply. It can be discharged by a DC load specially made by Micronics. This load is controlled in current, can sustain $2kW$ and used analog components to fallow fast transient. Thus, the DC load possess a bandwidth up to $1kHz$ in order to reproduce a PMSM consumption.

Because, the test bench posses only one DC load, the current send to the load is:

$$i_{DC} = i_{aux} + i_{M1} \tag{6.1}$$

where i_{aux} represents the unknown current consumes by the auxiliary circuit and i_{M1} represents the current consumes by the M1.

System	Symbol	Experiment value	Vehicle value	Unit
ICE	τ_+	$10\pi/3$	$10\pi/3$	
	τ_-	$40\pi/3$	$40\pi/3$	
M2	p	3	4	
	R_s	0.45	0.035	Ω
	L_d	3.8	0.1	mH
	L_q	3.8	0.3	mH
	Φ_f	0.14	0.042	Wb
Inertia	J	40	40	gm^2
Capacitor	C	1	1	mF
Current closed loop bandwidth	F_i	100	100	Hz

Table 6.1 – System parameters

6.2.1 Scale adaptation from the vehicle parameters to the test bench parameters

The test bench has been modified from the last thesis in order to accommodate the new needs. Old parts of the platform have been renewed and adapted to the powertrain dynamic. The powertrain parameters and the experiment parameters are given in the table 6.1.

From the vehicle, the ICE can delivered $90kW$ and the M2 can generated $30kW$. On the experiment, the ICE and the M2 are ten times smaller. The ICE is a $9kW$ motor and the M2 is rated to $3kW$. Thus, a power ratio of ten exists between the vehicle and the experiment.

The dynamic difference between the experiment and the vehicle are given by the parameter of each element. The parameters dissimilarity between the two M2 are handled by the current control shows in the next section. The existing tuning parameters presents in the current control have been tuned to present the same closed-loop bandwidth. The ICE parameters are the time constants from the vehicle. The added flywheel and the capacitor bank give us the same buffer dynamic than in the vehicle. Moreover, the sampling rate for the current control, the voltage control and rotational control has been chosen to be the same than the vehicle. Thus, if the system doesn't go into saturation, the dynamic behavior of the platform corresponds to the powertrain present inside the vehicle.

6.3 Low level control on the test bench

The current control is achieved as chapter 2 describes it. In the following section, the control of the current is recalled, the parameters are displayed and an experiment will illustrate the first step.

In the case of the experiment, the diagram in figure 6.4 shows the different inputs and outputs signals of the system. The diagram also shows the distribution between the transformation running inside the software, the connection with the hardware signal and feedback measure. Each block has been previously presented in the section 2.2. In the sequel, the essential block will be recalled.

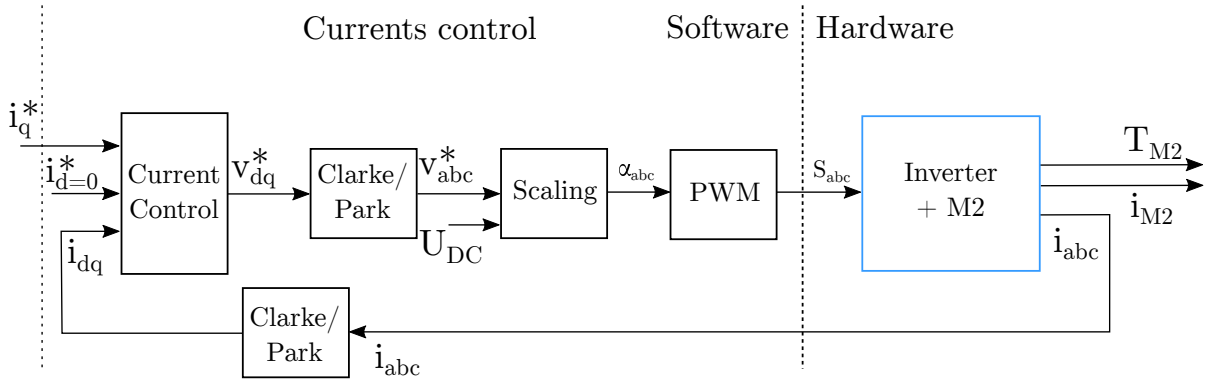

Figure 6.4 – Diagram of the current control

6.3.1 Current control

The first block is the current control. This block is made with two PI control law with the decoupling term introduced such that:

$$\begin{aligned} v_d^* &= k_{di} \int (i_d^* - i_d)dt + k_{dp}(i_d^* - i_d) - L_q i_q \omega_r \\ v_q^* &= k_{qi} \int (i_q^* - i_q)dt + k_{qp}(i_q^* - i_q) + \omega_r \Phi_f + L_d i_d \omega_r \end{aligned} \tag{6.2}$$

where k_{di} and k_{dp} are the control gain for the d axis and k_{qi} and k_{qp} are the control gain for the q axis.

The scaling consists of:

$$\begin{bmatrix} \alpha_a \\ \alpha_b \\ \alpha_c \end{bmatrix} = \frac{1}{U_{DC}} \begin{bmatrix} v_a^* \\ v_b^* \\ v_c^* \end{bmatrix} + \frac{1}{2} \tag{6.3}$$

where $[v_a^*, v_b^*, v_c^*]^T$ are the voltage references, $[\alpha_a, \alpha_b, \alpha_c]^T$ are the duty-cycles and U_{DC} is the DC bus voltage.

The PWM is implemented with the intersective method. This method used the duty-cycle to calculate the control signal needed for the IGBT. It is described in the section 2.2.4.

6.3.2 Current references

The M2 present in the experiment is a PMSM with smooth poles configuration. This configuration implies that $L_d = L_q$, that is the optimization problem presented in the section 2.4 can be simplified.

The electromagnetic torque T_{M2} is created by the interaction of the permanent magnets and the magnetic flux induced by the current in the stator winding. With smooth poles motors, the torque applied to the shaft output is such that:

$$T_{M2} = \frac{3}{2} p \, \Phi_f \, i_q = \alpha \, i_q \tag{6.4}$$

with the torque coefficient $\alpha = \frac{3}{2} p \, \Phi_f$.

Thus, the current i_d doesn't interact with the torque and the offline optimization has to be replaced in the experiment by the following setting:

— the current $i_d^* = 0$,
— the current $i_q^* = T_{M2}^*/\alpha$ as the input for the control design.

6.3.3 Experiment results with the current control

The tuning process involve to try and adapt the control parameters, first on simulation then on the system itself. Here, the parameters were chosen such that the close loop bandwidth is around $100Hz$. The resulted tuning is given on table 6.2 and the response of the system is shown in figure 6.5. The motor is turning at $1000RPM$ and the DC bus voltage is fixed at $180V$. The current i_d is stabilized around $0A$. The current reference i_q^* is stepping from $0A$ to $1A$. The current i_q shows the transient response when the current reference i_q^* changes. Compared to the simulation, the currents i_d and i_q present some oscillation due to the inverter non-linearity and the imperfection of the motor.

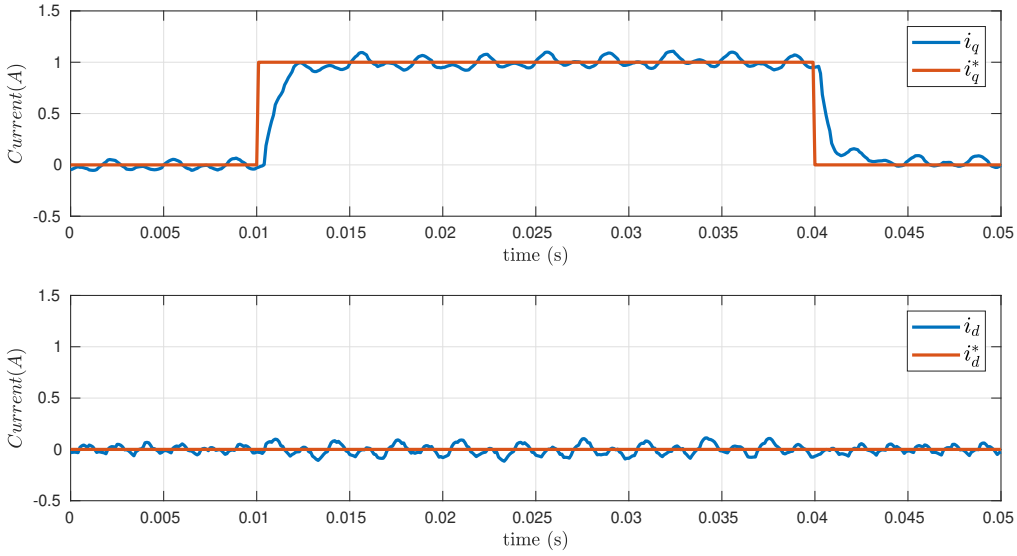

Figure 6.5 – Experiments results with the control of i_d and i_q. – Top: i_d current – Bottom: i_q current.

6.4 Voltage and rotational speed control

From the last section, the currents (i_d, i_q) are controlled and regulated around their references (i_d^*, i_q^*). Thus, the design control can evolve at the next level. Using the singular perturbation approach, developed in the section 4.2, the voltage and rotational speed control are designed. The singular perturbation approach is recalled with the experimental modeling. The difference from the vehicle and the experiment being the input control for the M2. In the case of the vehicle, the input of the M2 is the current produce on the DC bus. Here, the reference i_q^* is the image of the torque putted on the shaft of the M2. Thus, the next part is the presentation of the experiment modeling.

6.4.1 The experiment modeling

The structure of the system is represented in figure 6.6. The system shows three input: the torque reference T_{ICE}^* for the ICE, the current reference i_q^* of the M2 and the current reference i_{M1}^* of the M1. Also, the perturbations are: the current i_{aux} for the DC bus, the electrical losses P_{l2} from the M2 and the friction torque T_r on the flywheel shaft. The aims are to: realize the user demand that is the current demand i_{M1}^* for the M1, stabilize the rotational speed Ω of the flywheel and stabilize the voltage U_{DC} of the DC bus.

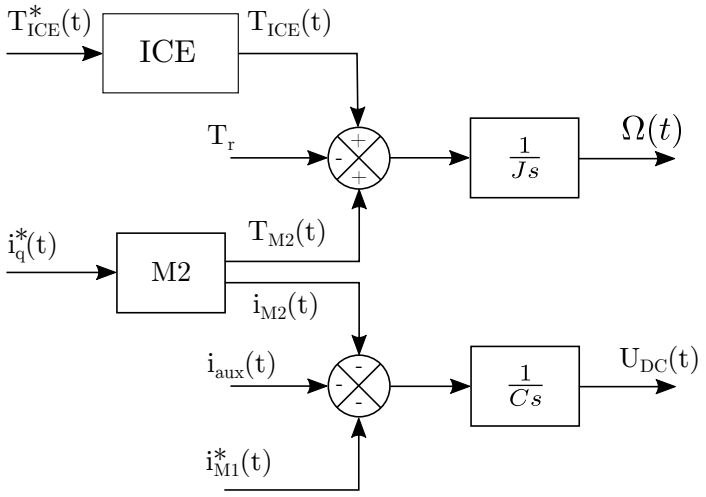

Figure 6.6 – Block diagram of the test bench

The state space model of the experiment is:

$$\begin{aligned} \dot{\Omega}(t) &= \frac{T_{ICE}(t) + \alpha i_q^*(t) - T_r}{J} \\ \dot{T}_{ICE}(t) &= \frac{\Delta T_{ICE}(t)\Omega(t)}{\tau_\pm - \frac{\tau_- - \tau_+}{2} sign\Delta T_{ICE}(t)} \\ \dot{U}_{DC}(t) &= \frac{-i_{M2}(t) - i_{aux}(t) - i_{M1}^*(t)}{C} \end{aligned} \tag{6.5}$$

with $\Delta T_{ICE}(t) = T^*_{ICE}(t - h(t)) - T_{ICE}(t)$ and $i_{M2}(t) = \dfrac{\alpha\, i_q^*(t)\, \Omega(t) + P_{l2}(t)}{U_{DC}(t)}$.

Where α is the torque coefficient of the M2 (see (6.4)), T_r is the friction torque present on the flywheel shaft and P_{l2} the electrical losses from the M2.

6.4.2 Application of the singular perturbation approach

The system (6.5) under consideration is recalled in a state variable form:

$$\begin{aligned} \dot{x}_1(t) &= \frac{1}{J}(x_2(t) + \alpha\, i_q^*(t) - T_r(t)) \\ \dot{x}_2(t) &= \frac{x_1(t)\,(T^*_{ICE}(t-h) - x_2(t))}{\tau_\pm - \frac{\tau_- - \tau_+}{2} sign(T^*_{ICE}(t-h) - x_2(t))} \\ \dot{x}_3(t) &= \frac{1}{C}(-\frac{\alpha\, i_q^*(t)\, x_1(t) + P_{l2}(t)}{x_3(t)} - i_{aux}(t) - i_{M1}^*) \end{aligned} \tag{6.6}$$

with the state vector

$$x(t) = \begin{bmatrix} x_1(t) \\ x_2(t) \\ x_3(t) \end{bmatrix} = \begin{bmatrix} \Omega(t) \\ T_{ICE}(t) \\ U_{DC}(t) \end{bmatrix}. \tag{6.7}$$

Remark 13 *The model* (6.6) *contains two time scales processes, the fast one is given by* $x_3 = U_{DC}$ *dynamic and the slow one is represented by the dynamics of* $x_1 = \Omega$ *and* $x_2 = T_{ICE}$.

Control diagram

The strategy developed with the singular perturbation approach comes from the strategy 1 and it is depicted in figure 6.7. It is composed of two subsystems: fast loop based on the fast actuators (PMSM) that drives the DC bus voltage U_{DC}; and slow loop based on the slow actuator (ICE) that stabilizes the rotational speed Ω of the flywheel.

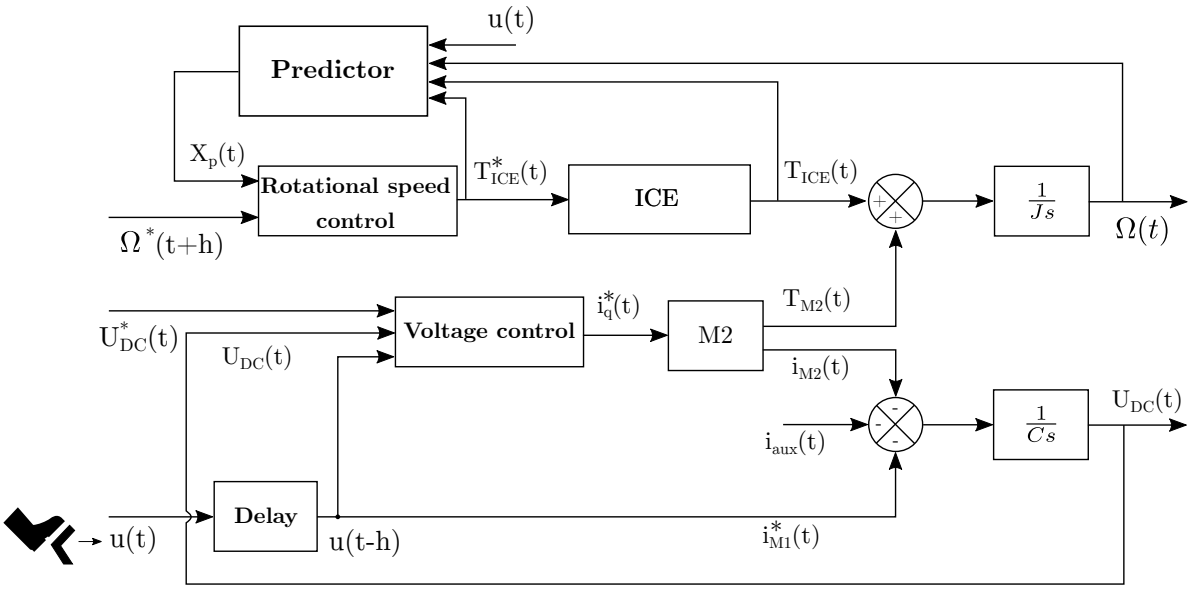

Figure 6.7 – Control scheme of the first strategy with the prediction

The fast control law design

The fast voltage control in (6.8) is a PI controller in terms of i_q^* that stabilizes the DC bus voltage $x_3 = U_{DC}$ at the reference level $x_3^* = U_{DC}^*$:

$$i_q^*(t) = -\frac{C\,x_3(t)}{\alpha\,x_1(t)}\left(K_P\left(x_3^*(t) - x_3(t)\right) + K_I\,x_4(t)\right) \tag{6.8}$$

where $x_4(t) = \int_0^t (x_3^*(\iota) - x_3(\iota))d\iota$.

The control input (6.8) being applied to system (6.6) yields the closed loop nonlinear system:

$$\begin{aligned}
\dot{x}_1(t) &= \frac{1}{J}\left(x_2(t) - \frac{C\,x_3(t)}{x_1(t)}(K_P\left(x_3^*(t) - x_3(t)\right) + K_I\,x_4(t)) - T_r(t)\right)\\
\dot{x}_2(t) &= \frac{x_1(t)\left(T_{ICE}^*(t-h) - x_2(t)\right)}{\tau_\pm - \frac{\tau_- - \tau_+}{2}\,sign(T_{ICE}^*(t-h) - x_2(t))}\\
\dot{x}_3(t) &= K_P\left(x_3^*(t) - x_3(t)\right) + K_I\,x_4(t) - \frac{1}{C}\left(\frac{P_{l2}(t)}{x_3(t)} + i_{aux}(t) + i_{M1}^*(t)\right)\\
\dot{x}_4(t) &= x_3^*(t) - x_3(t)
\end{aligned} \tag{6.9}$$

Following the singular perturbation approach, the fast variables are introduced as

$$\begin{aligned}
\varepsilon\,\xi_1(t) &= x_3^*(t) - x_3(t)\\
\varepsilon^2\,\xi_2(t) &= x_4(t)
\end{aligned} \tag{6.10}$$

Then system (6.9) can be rewritten as follows:

$$\begin{aligned}
\dot{x}_1(t) &= \frac{1}{J}\left(x_2(t) - \frac{C\,x_3(t)}{x_1(t)}(K_P'\,\xi_1(t) + K_I'\,\xi_2(t)) - T_r(t)\right)\\
\dot{x}_2(t) &= \frac{x_1(t)\left(T_{ICE}^*(t-h) - x_2(t)\right)}{\tau_\pm - \frac{\tau_- - \tau_+}{2}\,sign(T_{ICE}^*(t-h) - x_2(t))}\\
\varepsilon\dot{\xi}_1(t) &= -K_P'\xi_1(t) - K_I'\xi_2(t) + \frac{1}{C}\left(\frac{P_{l2}(t)}{x_3(t)} + i_{aux}(t) + i_{M1}^*(t)\right)\\
\varepsilon\dot{\xi}_2(t) &= \xi_1(t)
\end{aligned} \tag{6.11}$$

where the tuning parameters of the fast control (6.8) are given by

$$K_P = \frac{K_P'}{\varepsilon} \text{ and } K_I = \frac{K_I'}{\varepsilon^2}. \tag{6.12}$$

The tuning choice of K'_P and K'_I is made such that the polynomial $s^2 + K'_P s + K'_I$ is Hurwitz that yields the desired characteristics of the transient response. According to [KKO86], eq. (6.11) is rewritten in a singular perturbation form:

$$\dot{X}(t) = f(t, X(t), \xi(t), \varepsilon) \tag{6.13}$$

$$\varepsilon\dot{\xi}(t) = g(t, X(t), \xi(t), \varepsilon) \tag{6.14}$$

where $X(t) = [x_1(t), x_2(t)]^T$, $\xi(t) = [\xi_1(t), \xi_2(t)]^T$ and ε is a small positive parameter.

Now, the frozen solution of the fast dynamic equation (6.11), i.e. $\varepsilon = 0$, is computed as follows:

$$\alpha_0(t) = \begin{bmatrix} 0 \\ \dfrac{1}{K'_I}\left(\dfrac{P_{l2}(t)}{C\,x_3(t)} + \dfrac{i_{aux}(t)}{C} + \dfrac{i^*_{M1}(t)}{C}\right) \end{bmatrix}. \tag{6.15}$$

Proposition 3 *For all $x_1(t) > \Omega_{min} > 0$, a sufficiently small parameter $\varepsilon > 0$ exists such that the dynamics* (6.13)-(6.14) *can be accurately approximated by their slow dynamics described by the following system:*

$$\begin{aligned} \dot{X}(t) &= f(t, X(t), \alpha_0(t), 0) \\ &= \begin{pmatrix} \dfrac{1}{J}\left(x_2(t) - \dfrac{P_{l2}(t)}{x_1(t)} - i_{aux}(t)\dfrac{x^*_3(t)}{x_1(t)} - i^*_{M1}(t)\dfrac{x^*_3(t)}{x_1(t)} - T_r(t)\right) \\ \dfrac{x_1(t)\,(T^*_{ICE}(t-h) - x_2(t))}{\tau_\pm - \frac{\tau_- - \tau_+}{2}\,sign(T^*_{ICE}(t-h) - x_2(t))} \end{pmatrix} \end{aligned} \tag{6.16}$$

The slow control law design

The desired reference point for $x_1(t)$ is given by $x^*_1(t) = \Omega^*(t)$, where Ω^* is the desired rotational speed. The torque demand T_{M1} represents the driving cycle of the serial hybrid electric vehicle.

Equation (6.16) is presented in a vector-matrix format:

$$\dot{X}(t) = \begin{pmatrix} \dfrac{1}{J}\left(x_2(t) - \dfrac{P_{l2}(t)}{x_1(t)} - i_{aux}(t)\dfrac{x^*_3(t)}{x_1(t)} - i^*_{M1}(t)\dfrac{x^*_3(t)}{x_1(t)} - T_r(t)\right) \\ \dfrac{x_1(t)\,(T^*_{ICE}(t-h) - x_2(t))}{\tau_\pm - \frac{\tau_- - \tau_+}{2}\,sign(T^*_{ICE}(t-h) - x_2(t))} \end{pmatrix} \tag{6.17}$$

From the strategy 1, it can be seen that the system (6.17) is more complete than the

system (3.11) used in the prediction. Nevertheless, without the knowledge of the auxiliary current i_{aux}, the friction losses T_r and the electrical losses P_{l2}, the prediction can be used as described in the strategy 1. Greater will be the losses, greater will be the prediction error on the rotational speed. Fortunately, the power losses are small in comparison of the traction power. But, an observer method will be introduced in the next part in order to fulfill the lack.

Recall of the prediction

In order to introduce the predictor, the ICE dynamic is approximated as the equation (3.4) and presented in a vector-matrix format:

$$\dot{X}(t) = AX(t) + B\,T^*_{ICE}(t-h) + d(t) \tag{6.18}$$

with $A = \begin{bmatrix} 0 & 1/J \\ 0 & -x_1(t)/\tau_\pm \end{bmatrix}$, $B = \begin{bmatrix} 0 \\ x_1(t)/\tau_\pm \end{bmatrix}$ and

$$d(t) = \begin{bmatrix} \frac{1}{J}\left(-\frac{P_{l2}(t)}{x_1(t)} - i_{aux}(t)\frac{x^*_3(t)}{x_1(t)} - i^*_{M1}(t)\frac{x^*_3(t)}{x_1(t)} - T_r(t)\right) \\ 0 \end{bmatrix}.$$

The predicted vector $X_p(t)$ for the state vector $X(t)$ is computed as [MO79], [Léc+16] (also see Fig.4.1):

$$\begin{array}{l} X_p(t) = [X_{p1}(t), X_{p2}(t)]^T = X(t+h) \\ = e^{Ah}X(t) + \int_0^h e^{A(h-s)}BT^*_{ICE}(t-h+s)\mathrm{d}s + \int_0^h e^{A(h-s)}d(t+s)\mathrm{d}s \end{array} \tag{6.19}$$

The state prediction (6.19) transforms the system (6.18) into a delay-free system:

$$\dot{X}_p(t) = AX_p(t) + BT^*_{ICE}(t) + d(t+h) \tag{6.20}$$

Since (6.20) is not delayed anymore, all the controllers for delay-free systems can be used to stabilize it.

The control T^*_{ICE} is designed as:

$$\begin{array}{rcl} T^*_{ICE}(t) & = & \dfrac{Jv(t)\tau_\pm}{X_{p1}(t)} + X_{p2}(t) \\ v(t) & = & \ddot{x}^*_1(t+h) + \lambda_2(\dot{x}^*_1(t+h) - \dot{X}_{p1}(t)) + \lambda_1(x^*_1(t+h) - X_{p1}(t)) \\ & & +\lambda_0 \int_0^t (x^*_1(\iota+h) - X_{p1}(\iota))d\iota \end{array} \tag{6.21}$$

where λ_0, λ_1 and λ_2 are tuning parameters defined hereafter.

Substituting the control (6.21) into the reduced model (6.16), the compensated slow dynamic becomes:

$$\begin{aligned}\dot{X}_{p1}(t) &= \frac{1}{J}(X_{p2}(t) - \frac{P_{l2}(t+h) + i_{aux}(t+h)\, x_3^*(t+h)}{X_{p1}(t)} \\ &\quad - \frac{i_{M1}^*(t+h)\, x_3^*(t+h)}{X_{p1}(t)} - T_r(t+h)) \\ \dot{X}_{p2}(t) &= J(\ddot{x}_1^*(t+h) + \lambda_2 \dot{\tilde{X}}_{p1}(t) + \lambda_1 \tilde{X}_{p1}(t) + \lambda_0 \textstyle\int_0^t \tilde{X}_{p1}(\iota) d\iota)\end{aligned} \tag{6.22}$$

with the error $\tilde{X}_{p1}(t) = x_1^*(t+h) - X_{p1}(t)$. By taking into account that its dynamic must be very slow, T_{ICE}^* is considered as a slow input and has only a slow effect on the convergence of the dynamic (6.22).

Note that the error $\tilde{X}_{p1}(t)$ satisfies:

$$\ddot{\tilde{X}}_{p1}(t) = -\lambda_2 \dot{\tilde{X}}_{p1}(t) - \lambda_1 \tilde{X}_{p1}(t) - \lambda_0 \textstyle\int \tilde{X}_{p1}(t) dt + \frac{1}{J}\frac{\partial}{\partial t}(\Psi(t)) \tag{6.23}$$

with $\Psi(t) = \dfrac{P_{l2}(t+h) + i_{aux}(t+h)\, x_3^*(t+h) + i_{M1}^*(t+h)\, x_3^*(t+h)}{X_{p1}(t)} + T_r(t+h)$

Thus, the tuning choice of λ_0, λ_1 and λ_2 is made such that the polynomial function $s^3 + \lambda_2 s^2 + \lambda_1 s + \lambda_0$ is Hurwitz and guarantees the desired slow dynamics in (6.22).

6.4.3 Electrical power and mechanical torque losses estimation

In this section, an estimation approach is proposed to capture the electrical power (P_{el}) and mechanical torque losses (T_{ml}) in real-time (online estimation). The Input-Output Injection observer is used to achieve the objective [KI83], [KR85].

Input-Output Injection Observer

The first and third states dynamic of system (6.6) are considered where the electrical power (P_{el}) and mechanical torque (T_{ml}) losses are being considered as constant states

variables

$$\begin{array}{rcl} \dot{x}_1(t) & = & \dfrac{x_2(t) + \alpha\, i_q(t) - T_{ml}(t)}{J} \\ \dot{T}_{ml}(t) & = & 0 \\ & & -\dfrac{\alpha\, i_q(t) x_1(t) + P_{el}(t)}{x_3(t)} - i_{M1}(t) \\ \dot{x}_3(t) & = & \dfrac{}{C} \\ \dot{P}_{el}(t) & = & 0 \end{array} \tag{6.24}$$

where $T_{ml}(t) = T_r(t)$ and $P_{el}(t) = P_{l2}(t) + i_{aux}(t)x_3(t)$.

The goal is to estimate (P_{el}) and (T_{ml}) by considering the speed $x_1(t) = \Omega(t)$, the torque $x_2(t) = T_{ICE}(t)$, the DC bus $x_2(t) = U(t)$, the load current $i_l(t)$ and the current $i_q(t)$ as outputs-inputs measurements.
Consequently, the system (6.24) can be written in the Input-Output Injection form [KI83]

$$\begin{array}{rcl} \dot{Z}_1 & = & A_1 Z_1 + \psi_1(y,u) \\ y_1 & = & C_1 Z_1 \end{array} \tag{6.25}$$

where $Z_1 = [x_1(t); T_{ml}]^T$, $A_1 = \begin{pmatrix} 0 & -\frac{1}{J} \\ 0 & 0 \end{pmatrix}$,
$\psi_1(y,u) = \begin{pmatrix} \dfrac{x_2(t) + \alpha\, i_q(t)}{J} \\ 0 \end{pmatrix}$ and $C_1 = [1;0]$;

$$\begin{array}{rcl} \dot{Z}_2 & = & A_2(y) Z_2 + \psi_2(y,u) \\ y_2 & = & C_2 Z_2 \end{array} \tag{6.26}$$

where $Z_2 = [x_3(t); P_{el}]^T$, $A_2(y) = \begin{pmatrix} 0 & -\frac{1}{C\, x_3(t)} \\ 0 & 0 \end{pmatrix}$,
$\psi_2(y,u) = \begin{pmatrix} -\dfrac{\alpha\, i_q(t) x_1(t)}{x_3(t)} - i_{M1}(t) \\ \hline C \\ 0 \end{pmatrix}$, $C_2 = [1;0]$.

By applying the Kalman criterion, it can be remarked that system (6.25) and (6.26) are observable, since the rank of $\begin{pmatrix} C_i \\ C_i A_i \end{pmatrix}$, $i = 1, 2$, is equal to 2, with $x_3(t) \geq U_{min}$ for

system (6.26). Then, an observer can be designed for systems (6.25) and (6.26) as:

$$\begin{array}{rcl} \dot{\hat{Z}}_i & = & A_i\hat{Z}_i + \psi_i(y,u) + G_iC_i(Z_i - \hat{Z}_i) \\ \hat{y}_i & = & C_i\hat{Z}_i, \quad i = 1,2 \end{array} \tag{6.27}$$

where $\hat{Z}_1 = [\hat{x}_1(t); \hat{T}_{ml}]^T$, $\hat{Z}_2 = [\hat{x}_3(t); \hat{P}_{el}]^T$ and $G_i = [G_{i1}; G_{i2}]^T$ is the gain of the corresponding observer.

In order to implement the control scheme (6.8)-(6.21), the controls $T^*_{ICE}(t)$ (6.21) and $i^*_{M2}(t)$ (6.8) remains the same, the losses (P_{el}) and (T_{ml}) are replaced in the predictor (6.19) by their estimates resulting in the predictor:

$$X_p(t) = e^{Ah}X(t) + \int_0^h e^{A(h-s)}BT^*_{ICE}(t-h+s)\mathrm{d}s + \int_0^h e^{A(h-s)}d(t+s)\mathrm{d}s \tag{6.28}$$

$$\text{with } A = \begin{bmatrix} 0 & \frac{1}{J} \\ 0 & -\frac{x_1(t)}{\tau_\pm} \end{bmatrix},\ B = \begin{bmatrix} 0 \\ \frac{x_1(t)}{\tau_\pm} \end{bmatrix} \text{ and } d(t) = \begin{bmatrix} -\frac{i^*_{M1}(t)\,x^*_3(t)}{J\,x_1(t)} - \frac{\hat{P}_{el}(t)}{J\,x_1(t)} - \frac{\hat{T}_{ml}(t)}{J} \\ 0 \end{bmatrix}.$$

Where $(\hat{P}_{el})$ and $(\hat{T}_{ml})$ are given by observers (6.27).

6.4.4 Experimental results

The parameters K'_P and K'_I of the fast control (6.8) (fast loop) are tuned such that the second order polynomial $s^2 + K'_P s + K'_I$ is Hurwitz, and the DC link voltage in the steady state is kept close to the reference U^*_{DC} with $\pm 10V$ of margin. Then, according to (6.12), K_P and K_I are calculated to make ε sufficiently small in order to achieve two times-scales (see table 6.2).

The parameters λ_0 and λ_1 of the slow control (6.21) (slow loop) are fixed (see table 6.2) such that:

— the compensated dynamics of the slow loop are slower than the fast loop (6.14),
— the polynomial function $s^3 + \lambda_2 s^2 + \lambda_1 s + \lambda_0$ is Hurwitz,
— the transient error is kept at ± 250RPM when the power demand occurs.

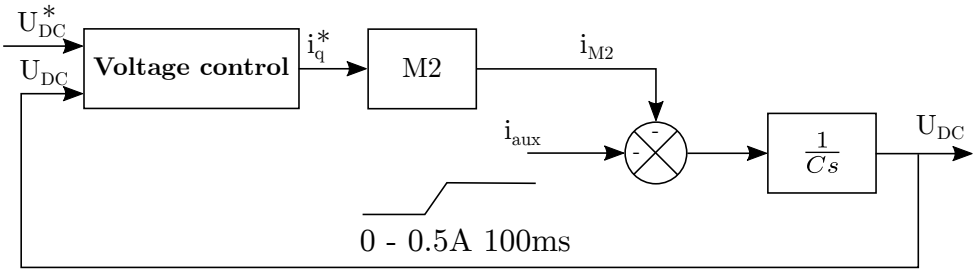

Figure 6.8 – Diagram of the voltage control experiment

Voltage control

In the following test, it has been decided to study only the voltage loop presented in figure 6.8. It is made by assuming that the rotational speed is being perfectly regulated. In practice, the ICE dynamic simulation is removed from this experiment software and the rotational speed is controlled through the torque by a PI control law. Note that, the goal is to ensure that the DC bus control is tested without the interaction of the rotational speed. The aim is to maintain the voltage on a desired range when a perturbation occurs:

$$|U_{DC}^{*} - U_{DC}| \leq 10V \tag{6.29}$$

With the following conditions:

— the perturbation demand i_{aux} is unknown and rise from $0A$ to $0.5A$ in $100ms$,

— the close loop bandwidth of the PMSM current control is around $100Hz$,

— the voltage control is run at $10kHz$,

— the PWM period is $0.1ms$.

Figure 6.9 shows the result with a constant rotational speed at $\Omega = 1000\,RPM$, the

Symbol	Value
K_P	25.76
K_I	338.6
ε	0.1
λ_0	120.0
λ_1	15.3
G_1	$[36.8, -13.9]^T$
G_2	$[36.8, -67.7]^T$

Table 6.2 – Control parameters

tuning gain $\omega_c = 628\,rad/s$, $\xi = 0.7$, $\lambda_0 = 128$ and $\lambda_1 = 8200$. It can be seen that the voltage is kept above $190V$ when the perturbation occur at $0.5s$. Also to realize the current demand $i_l = 0.5A$, the i_q^* is moving accordingly in order to compensate the consumption.

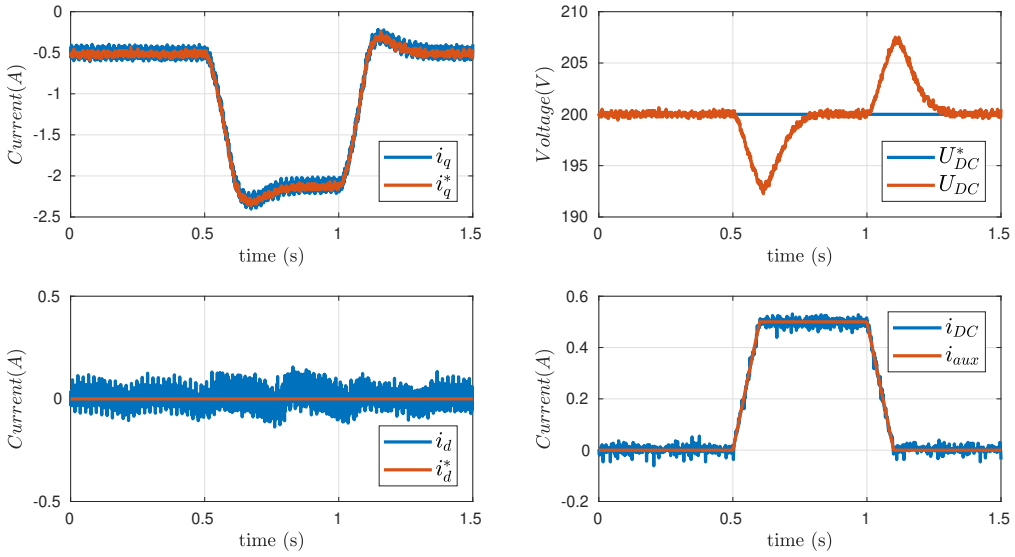

Figure 6.9 – Experimentation results of the voltage control and the auxiliary circuit i_{aux} varies between 0A and 0.5A. Recall $i_{DC} = i_{aux} + i_{M1}$ – Top left: i_q current – Top right: DC link voltage – Bottom left: i_d current – Bottom right : Load current.

The experiment presented here, see figure 6.9, can be compared to the simulation presented in the end of the first chapter, see figure 2.17. The experiment is run with the real hardware while the simulation is run with the switching model of the inverter and the PMSM model. Despite the assumptions made in the simulation, the experiment shows a similar behavior, particularly in the voltage transient is closed to the simulation. The experiment presents more noise than the simulation, especially on the current i_q and the current i_d. It is mostly due to inverter non-linearity and imperfection of the M2. It can be noted the offset presents on the current i_q when the current load is zero. This offset corresponds to the current needed to overcome the electrical losses.

Thus, the experiment shows the ability to stabilize the voltage of the DC bus under the perturbation and with the current control developed previously.

Rotational control

The performance of the proposed controls (6.8) and (6.21) is experimentally tested. The system parameters are given in table 6.2. The benchmark references are given in figure 6.10.

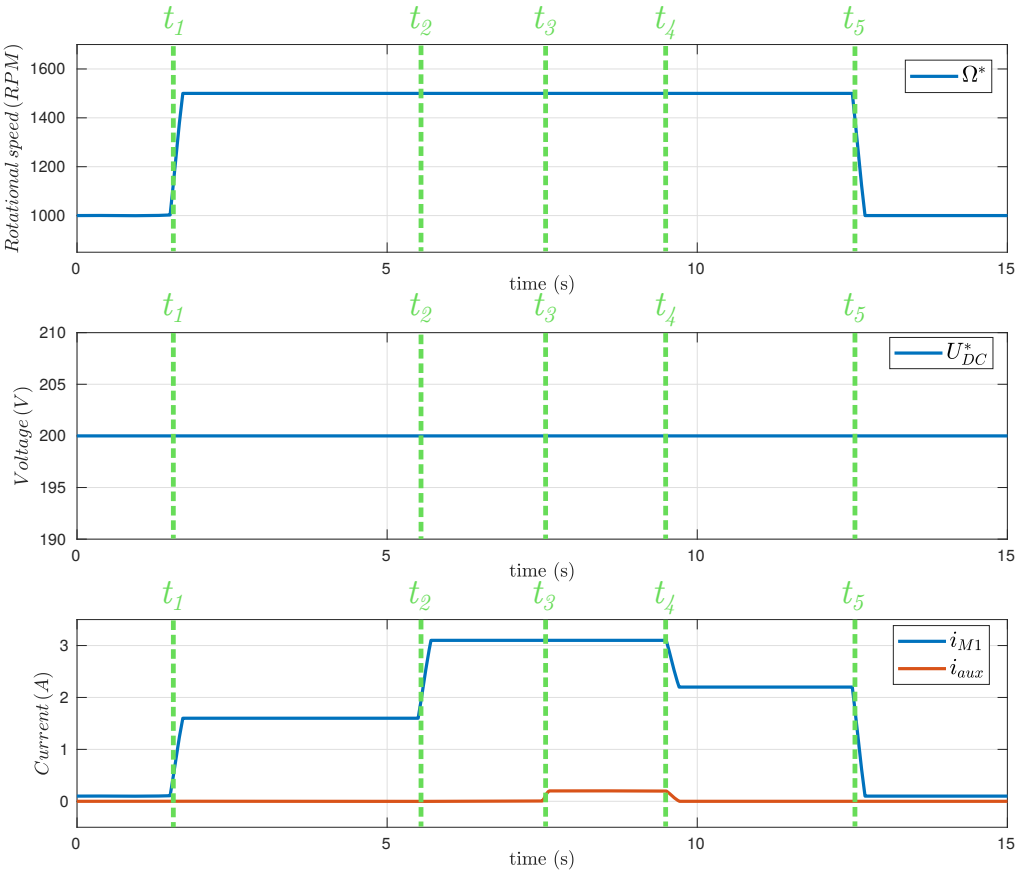

Figure 6.10 – Experimentation references for the rotational speed control with the prediction and the voltage control. – Top: Rotational speed reference – Middle: Voltage references – Bottom: Current references.

For this experiment, the observers described previously are disable. The voltage reference of the DC bus is set to $U^*_{DC} = 200V$. At the beginning of the experiment, the rotational speed starts around the idle speed at $\Omega^* = 1000RPM$ and the current demand are all close to zero. At the time $t = t_1$, the current demand occurs $i_{M1} = 1.6A$ and the rotational speed quickly increases to $\Omega^* = 1500RPM$ in order to avoid the power limitation of the M2. At the time $t = t_2$, the current demand goes to $i_{M1} = 3.1A$. At the time $t = t_3$, the auxiliary circuit kick in and consumes $i_{aux} = 0.2s$. At the time $t = t_4$, the current

decreases at $i_{M1} = 2.2A$ and the auxiliary consumption is set off. At the time $t = t_5$, the current demand is set to zero and the rotational speed decreases to $\Omega^* = 1000RPM$.

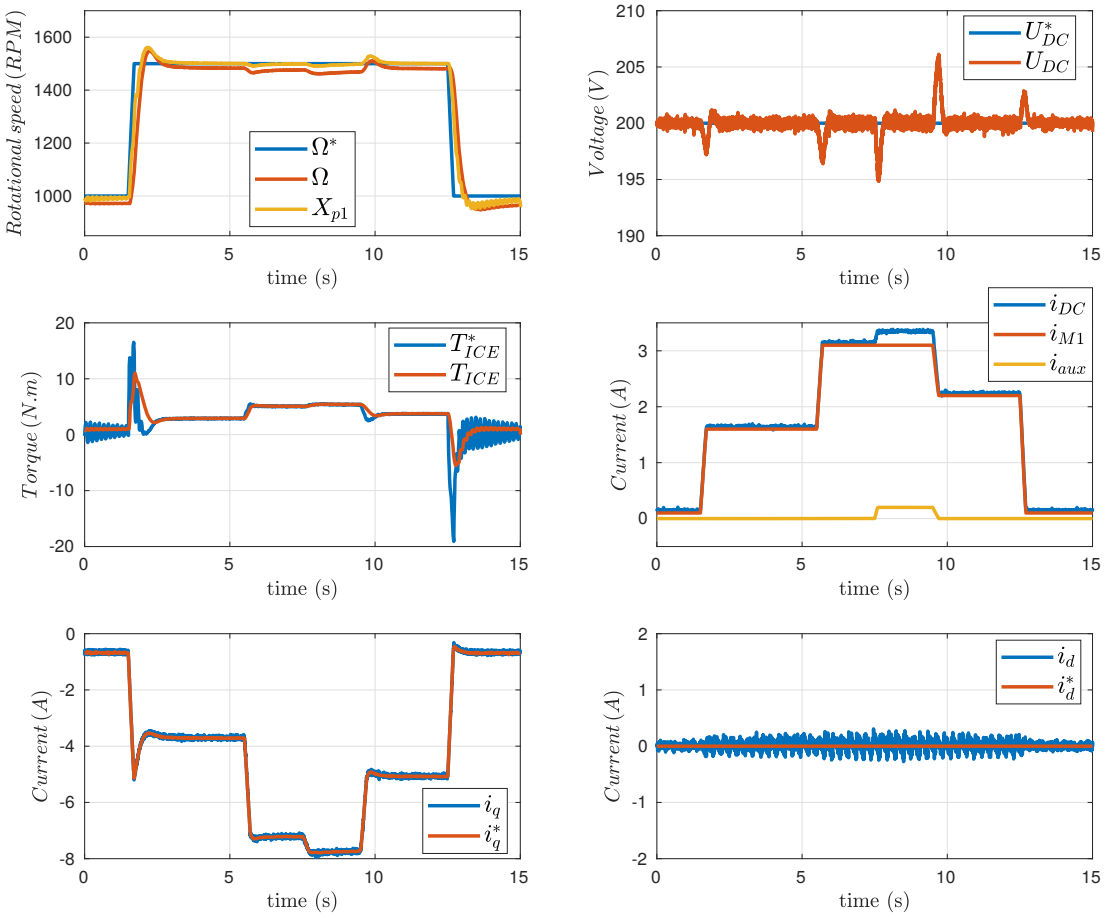

Figure 6.11 – Experimentation results of the rotational speed control with the prediction ans the voltage control (recall $i_{DC} = i_{aux} + i_{M1}$).

Figure 6.11 shows the response of the system according to the reference trajectories. It can be seen:

— an accurate regulation of the DC bus voltage ensured by the proposed fast control (6.8),

— a smooth response of the ICE during the fast power demands of the load.

The energy balance is characterized by a predicted rotational speed X_{p1} reaching accurately the desired set point (1500 RPM) at steady state by the proposed slow control (6.21). Note the steady state error between the speed prediction X_{p1} and the speed Ω can be observed in figure 6.12.

It can be seen from figure 6.12 that between $t = t_1$ and $t = t_2$, the load reaches

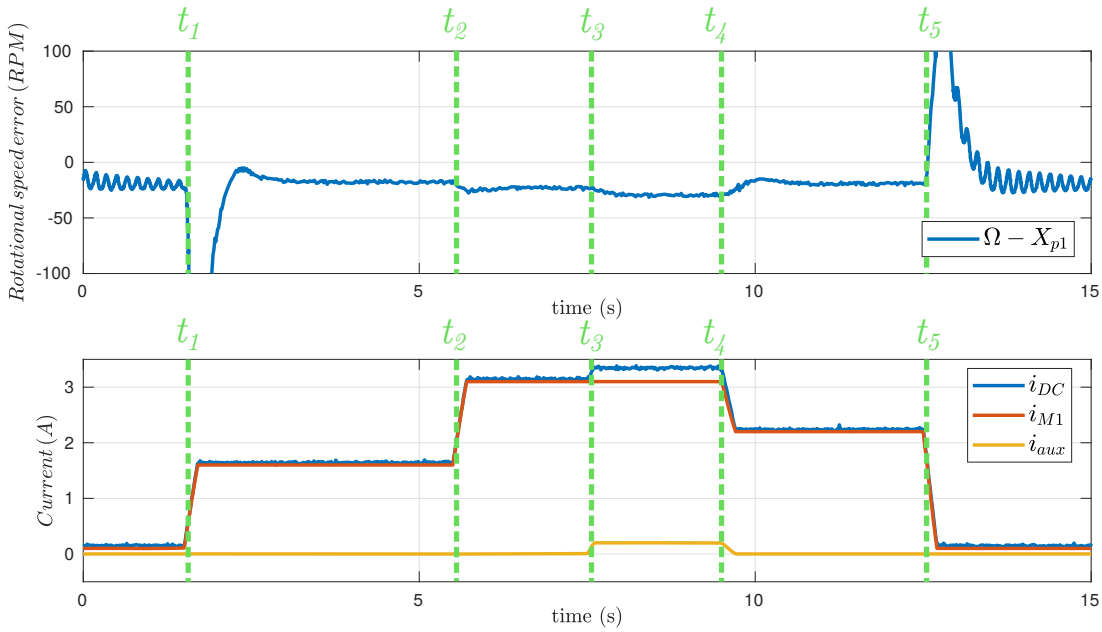

Figure 6.12 – Experimentation results of the rotational speed control with the prediction and the voltage control (recall $i_{DC} = i_{aux} + i_{M1}$). Top: Predicted rotational speed error – Bottom: Load current.

a value of $1.6A$, and the steady state error is around 18RPM (1.2% of the 1500RPM). Between $t = t_2$ and $t = t_3$, the load current is set to $3.1A$, and the steady state error is around 23RPM (1.5%). Between $t = t_4$ and $t = t_5$, the load current is set to $2.2A$ and the steady state error is around 20RPM (1.3%). Therefore, the experiment results show that the error depends on the current load. The error in this experiment can be explained by the fact that the control model (6.5) has been considered with the energy losses set to zero. In addition to the load current set to $3.1A$, the auxiliary circuit consumes $0.2A$ between $t = t_3$ and $t = t_4$. This unknown consumption to the prediction scheme push the steady state error around 30RPM (2%). The results presented in this experiment show a similar behavior than the simulation figure 3.10. The experiment also shows the possibility of a real implementation of the control scheme. The stabilization error can be reduced by estimating the energy losses and the current consumption of auxiliary circuit. The estimation can be fed to the predictor and the control function in order to cancel the error.

Rotational control with the observation approach

The performance of the proposed observation approach is tested in this part. The observers parameters are given in table 6.2. The benchmark references are exactly the same as before.

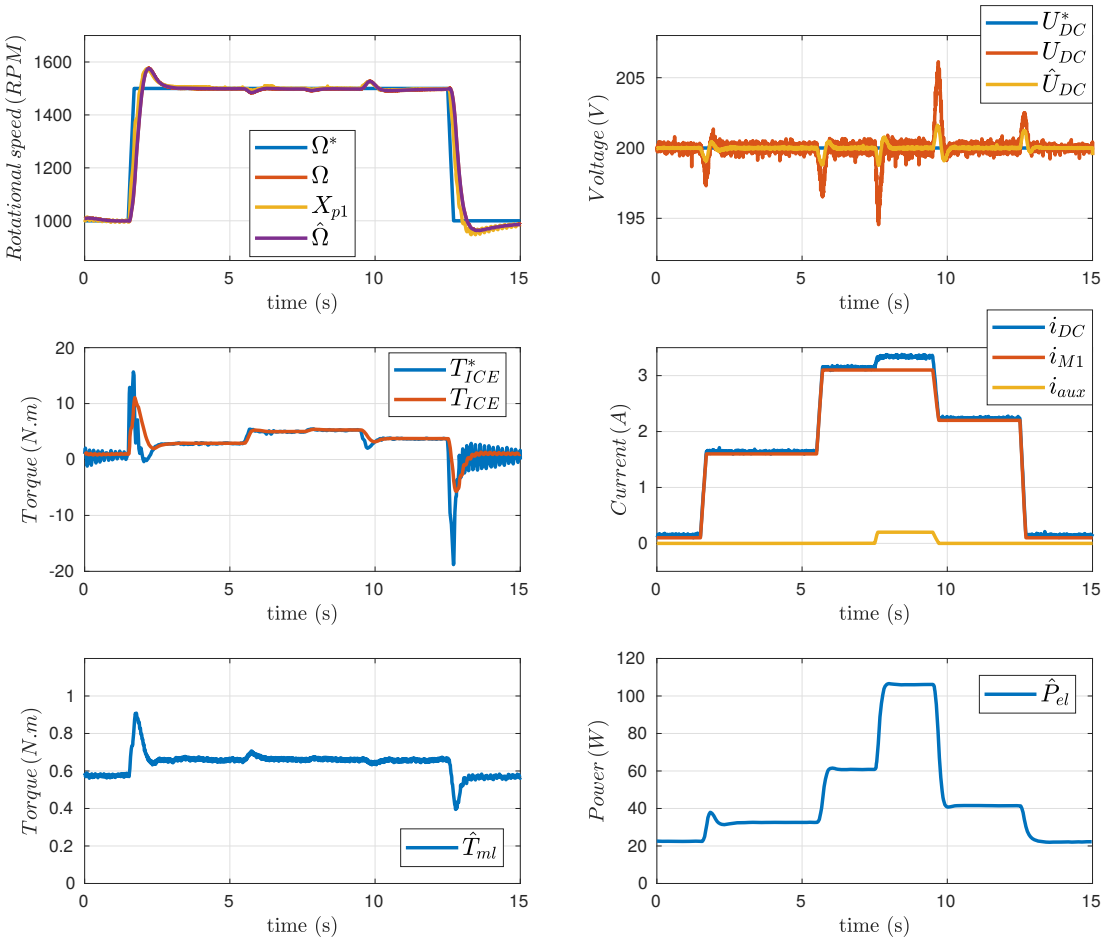

Figure 6.13 – Experimentation results of the rotational speed control with the prediction, the observation approach and the voltage control (recall $i_{DC} = i_{aux} + i_{M1}$).

Figure 6.13 shows the response of the system according to the reference trajectories. It can be seen:

— an accurate regulation of the DC bus voltage ensured by the proposed fast control (6.8),

— a smooth response of the ICE during the fast power demands of the load,

— the torque losses observer converge around $0.65N.m$ and the electrical power losses varies with the current load.

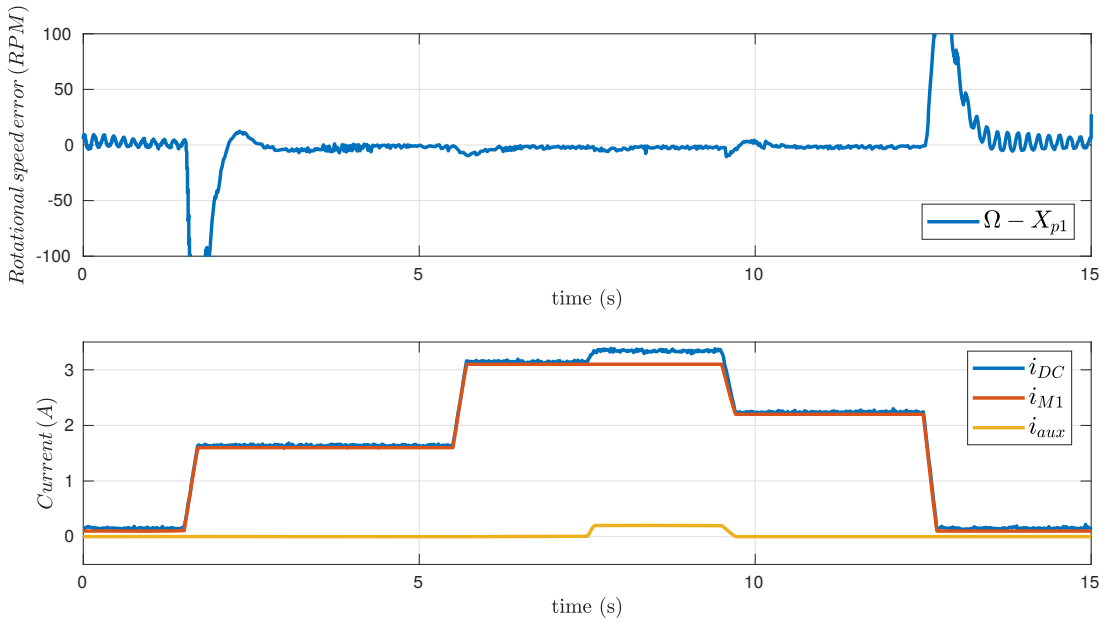

Figure 6.14 – Experimentation results of the rotational speed control with the prediction, the observation approach and the voltage control (recall $i_{DC} = i_{aux} + i_{M1}$). – Top: Predicted rotational speed error – Bottom: Load current.

Compare to the last experiment, it can be seen from figure 6.14 that the steady state error varying with the load is no longer present.

6.5 Open loop supervision

On this part, the open loop method proposed on the part 5.5 is tested on the bench. The open loop method has been proposed for improving the time respond from this serial hybrid vehicle. The aim is to open the slow control loop dedicated to the rotational speed when the demand occurs. See figure 6.15, the loop will be cut between the control law and the torque reference for the ICE.

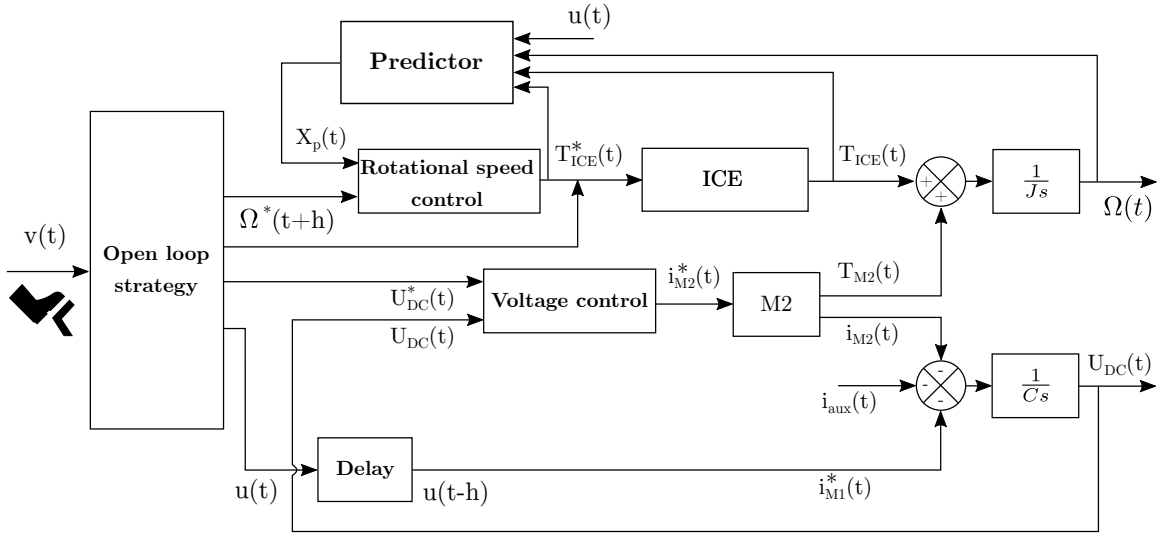

Figure 6.15 – Control scheme of the open loop strategy with the prediction

The idea is to demand the maximum torque to the ICE and wait until the flywheel has stored enough energy before switching the M1 from his initial state to the traction demanded by the user. Doing this, the user demand is delayed by the time needed to reach the requested ICE power and the flywheel gets enough energy to absorb the transient.

An experiment of the open loop strategy is shown in figure 6.16. The aim is to deliver $900W$ corresponding at 60% of the capability of the M2 at this rotational speed. Beginning at the rotational speed $\Omega^* = 1000RPM$ and the DC bus voltage at $U^*_{DC} = 200V$. The user demand represented by the M1 current goes from 0 to $4.5A$ at $0.5s$. The loop opens at $0.5s$ and for $t_O = 100ms$. During this time, the maximum torque $20N.m$ is requested to the ICE. Thus, the ICE torque is climbing as well as the rotational speed of the flywheel. When the flywheel reaches $1100RPM$, the M1 is switched on and the loop is closed after the delay.

Note the decreasing of the rotational speed (circle in green on the top left of the figure) when the M1 current is rising. It corresponds to the area where the M2 torque is higher

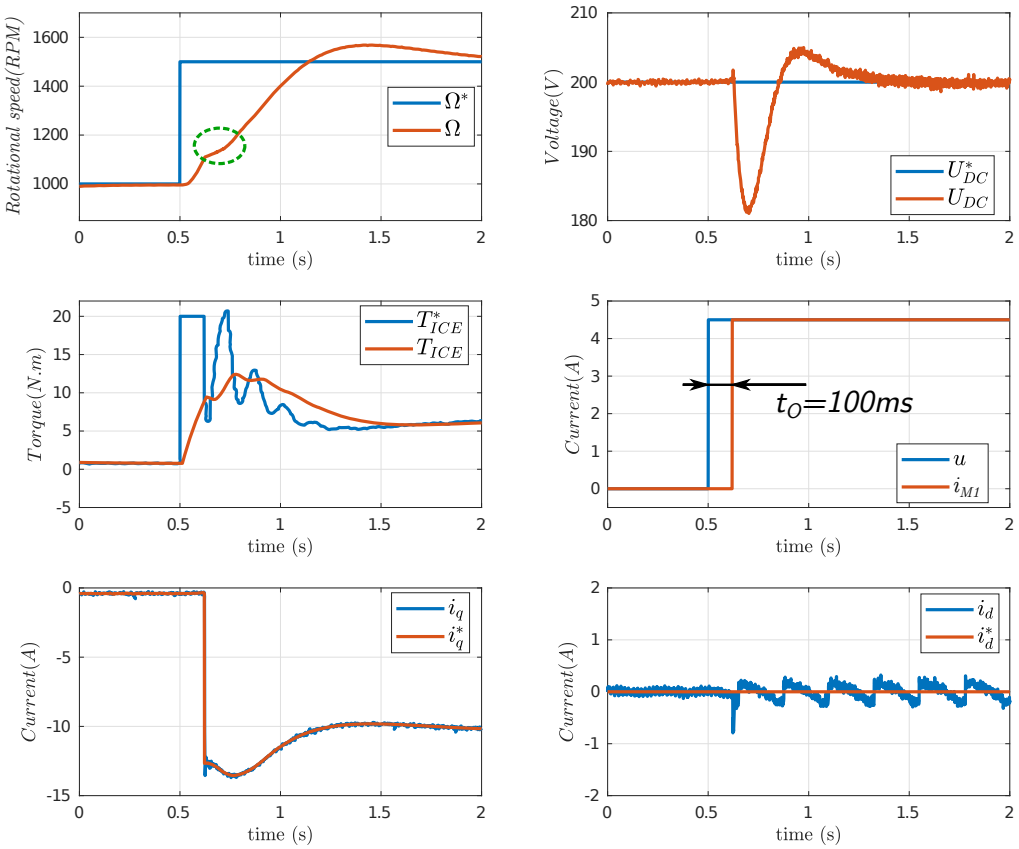

Figure 6.16 – Experimentation results of the open loop supervision with the prediction and the voltage control.

than the ICE torque. It is an instant where the energy is drawn from the flywheel.

6.6 Summary

Contributions

— Application of the control scheme developed on the thesis.

— Validation of the proposed scheme on a test bench.

Conclusion

In this thesis, we have studied and achieved a control solution for a serial electric hybrid vehicle without the main battery. A strategy based on a cascade of simple control law has been proposed to counteract the system problem. Indeed, the main contributions are:

— to demonstrate the feasibility of propelling the car without the main battery connected,
— to present different strategy to control the powertrain,
— to give an understanding of the coupling effect between the two time scales,
— to estimate the power losses and integrate them in the control loop,
— to proposes simple algorithm for improving the driver feeling.

The feasibility and performance have been an important focus of this research work. The powertrain being already designed, it has been crucial to determine if a battery failure could be overcome with the physical parameters given by the constructor. Indeed, the E-TECH powertrain has been entered in the sale marker at the beginning of 2020, with a simple but robust algorithm to overcome the battery failure. Thus, this thesis has been dedicated to not only overcome the failure, but extends the use-case around a more advance solution. Where the battery can be safely disconnected to improve the traction performance when the battery is cold or discharged.

The first chapter began by recalling the various HEV characteristics like the topology and the size. The problems, the objectives and the constraints offers by the powertrain are highlighted. This allows to introduce the context and the challenge that the thesis will have to encounter.

The second chapter has presented the modeling of the electric motor, the inverters and DC bus. It has shown the control design and offline optimization needed to properly regulate the voltage of the DC bus. The method presented in this chapter is recalled from the literature and give to thesis a foundation for the next stage.

The third chapter has presented three strategies, where each strategies assigned differently one control aim to one of the system inputs. The strategies are implemented with a first approximation and discussed around results provided by simulations. The three

strategies have been shown downside and positive aspects: to regulate the flywheel speed, to control the DC bus voltage and to realize the driver demand.

The fourth chapter has been picked the most suitable strategy outgoing from last chapter. The first approximation made to implement the strategy has been developed with the singular perturbation approach. The approach has revealed the validity of the approximation and shows the improvement of the strategy by using an observer method to estimate the losses present in the system. Thus, this chapter presents the outcome of the second and third chapter.

The fifth chapter has presented a power management able to provide the references for the flywheel rotational speed and the DC bus voltage. The principal aim behind the presented power management has been to deal with the saturation of each element of the hybrid serial vehicle and found the best references that realize the driver's request. The last contribution has been an open loop method proposed to get a greater time respond. The approach developed here consisted by delaying the driver demand to store energy and respond with a better feeling for the driver.

The sixth chapter has presented experiments to verify the effectiveness of the control algorithm designed in the previous chapters. The test bench is introduced and the effect of the scale difference between the vehicle powertrain and the bench parameters has been discussed. The control algorithms presented in previous chapters are recalled and applied to the test bench configuration. Moreover, the experimental results are shown and explained.

Other than the works done in the thesis, the study of the serial hybrid vehicle with a disconnected battery could be further developed in the following aspects:

— investigate allocation technic and frequencies decoupling for the control partitioning,
— in-depht stability analysis with a three stage singular perturbation approach,
— develop an optimization for finding the best open time in the open-loop strategy,
— implement the developed algorithm on Renault vehicle.

BIBLIOGRAPHY

[AD05] Glumineau Alain and Jesus De Leon-Morales, *Sensorless AC Motor Control: Robust Advanced Design Techniques and Applications*, SPRINGER, May 2005, DOI: 10.1007/978-3-319-14586-0, URL: https://hal.archives-ouvertes.fr/hal-01180079.

[ADE18] ADEME, *Évolution du marché, caractéristiques environnementales et techniques des Véhicules particuliers neufs vendus en France*, tech. rep. EAN 9791029701573, Oct. 2018.

[Agh+17] A. Aghmadi et al., « Decoupling method of the Permanent Magnet Synchronous Generator using Singular Perturbation Theory », *in*: *2017 International Renewable and Sustainable Energy Conference (IRSEC)*, 2017, pp. 1–7, DOI: 10.1109/IRSEC.2017.8477563.

[Bou17] Abdelkader Bouarfa, « Méthodes de commande par allocation de convertisseurs statiques polyphasés, multi-niveaux : de la modélisation à la mise en oeuvre temps-réel », Theses, Université Paul Sabatier - Toulouse III, Nov. 2017, URL: https://tel.archives-ouvertes.fr/tel-01906348.

[Bre12] Delphine Bresch-Pietri, « Commande robuste de systèmes à retard variable : Contributions théoriques et applications au contrôle moteur », Thèse de doctorat dirigée par Petit, Nicolas Mathématique et automatique Paris, ENMP 2012, PhD thesis, 2012, URL: http://www.theses.fr/2012ENMP0060/document.

[Car10] Sébastien Carrière, « Synthèse croisée de régulateurs et d'observateurs pour le contrôle robuste de la machine synchrone », PhD thesis, May 2010, URL: https://oatao.univ-toulouse.fr/7203/.

[Chi05] J. Chiasson, *Modeling and High Performance Control of Electric Machines*, IEEE Press Series on Power Engineering, Wiley, 2005, ISBN: 9780471684497.

[Dai15] Ping Dai, « Réjection de perturbation sur un système multi-sources - Application à une propulsion hybride », 2015POIT2251, PhD thesis, 2015, URL: http://www.theses.fr/2015POIT2251/document.

[Edw11] Edwards R, Larive' J, Beziat J, *Well-to-Wheels Analysis of Future Automotive Fuels and Power Trains in the European Context*, JRC65998, Report, Version 3c, Luxembourg (Luxembourg): Publications Office of the European Union, 2011, URL: https://publications.jrc.ec.europa.eu/repository/handle/JRC65998.

[Err10] Rachid Errouissi, « Contribution à la commande prédictive non linéaire d'une machine synchrone à aimants permanents », Theses, Université du Québec à Chicoutimi, June 2010, URL: https://constellation.uqac.ca/261/.

[Gaz19] Yvonnick Gazeau, « Précis d'électrification automobile », *in*: *Ingénieurs de l'Auto*, vol. 860, 2019.

[Ger+16] Andreas Gerlach et al., « Efficient control of internal combustion engines for electric power generation without throttle actuator », *in*: *IECON 2016 - 42nd Annual Conference of the IEEE Industrial Electronics Society*, 2016, pp. 1802–1807, DOI: 10.1109/IECON.2016.7793254.

[Gha+11] Malek Ghanes et al., « Singular Perturbation Control for coordination of converters in a Fuel Cell System », *in*: *ELECTRIMACS*, Cergy-Pontoise, France, June 2011, URL: https://hal.inria.fr/hal-00752998.

[Glu15] A. Glumineau, *Stratégies Avancées de Commande des Systèmes Non Linéaires - Cours SACNL*, Centrale Nantes, 2015.

[GS13] Lino Guzzella and Antonio Sciarretta, *Vehicle Propulsion Systems - Introduction to Modeling and Optimization*, Springer-Verlag Berlin Heidelberg, 2013, ISBN: 978-3-642-35913-2, DOI: 10.1007/978-3-642-35913-2.

[Har12] Brian Harries, « Development of a Supervisory Control Unit for a Series Plug-in Hybrid Electric Vehicle », *in*: 2012.

[Hil+13] M. Hilairet et al., « A passivity-based controller for coordination of converters in a fuel cell system », *in*: *Control Engineering Practice* 21.*8* (2013), pp. 1097–1109, ISSN: 0967-0661, DOI: https://doi.org/10.1016/j.conengprac.2013.04.003, URL: http://www.sciencedirect.com/science/article/pii/S0967066113000701.

[HON] HONDA, *2015 Fit Hybrid*, URL: https://global.honda/heritage/timeline/product-history/automobiles/2015FitHybrid.html, (accessed: 24.04.2021).

[HS97] D. Hrovat and Jing Sun, « Models and control methodologies for IC engine idle speed control design », *in*: *Control Engineering Practice* 5.*8* (1997), pp. 1093–1100, ISSN: 0967-0661, DOI: https://doi.org/10.1016/S0967-0661(97)00101-9.

[Hun04] John Hunter, « Asymptotic Analysis and Singular Perturbation Theory », *in*: (Jan. 2004).

[Jan11] Noëlle Janiaud, « Modélisation du système de puissance du véhicule électrique en régime transitoire en vue de l'optimisation de l'autonomie, des performances et des coûts associés. », Theses, Supélec, Sept. 2011, URL: https://tel.archives-ouvertes.fr/tel-00660749.

[Kes+08] J. T. B. A. Kessels et al., « Online Energy Management for Hybrid Electric Vehicles », *in*: *IEEE Transactions on Vehicular Technology* 57.*6* (2008), pp. 3428–3440, DOI: 10.1109/TVT.2008.919988.

[Kha96] H. Khalil, *Nonlinear systems, 2nd edition*, Upper-Saddle River: Printice-Hall, 1996.

[KI83] A. J. Krener and A. Isidori, « Linearization by output injection and nonlinear observers », *in*: *Systems & Control Letters* 3 (1983), pp. 47–52.

[KKO86] P. V. Kokotovic, H. K. Khalil, and J. O'Reilly, *Singular Perturbation Methods in control: Analysis and design*, New York: Academic Press, 1986.

[Kot12] Mohamad Koteich, *Sensorless Vector Control of Brushless Motors (French)*, Sept. 2012, DOI: 10.13140/2.1.3149.8561.

[KR85] Arthur J Krener and Witold Respondek, « Nonlinear observers with linearizable error dynamics », *in*: *SIAM Journal on Control and Optimization* 23.*2* (1985), pp. 197–216.

[Léc+16] V. Léchappé et al., « Delay Estimation and Predictive Control of Uncertain Systems With Input Delay: Application to a DC Motor », *in*: *IEEE Transactions on Industrial Electronics* 63.*9* (Sept. 2016), pp. 5849–5857, ISSN: 1557-9948, DOI: 10.1109/TIE.2016.2527692.

[MAC18] Mohamed MACHMOUM, *Electrotechniques analytique*, Ecole polytechnique de l'université de Nantes, 2018.

[Mal14] A. A. Malikopoulos, « Supervisory Power Management Control Algorithms for Hybrid Electric Vehicles: A Survey », *in*: *IEEE Transactions on Intelligent Transportation Systems* 15.*5* (2014), pp. 1869–1885, DOI: 10.1109/TITS.2014.2309674.

[ME14] Roland Matthe and Ulrich Eberle, « The Voltec System: Energy Storage and Electric Propulsion », *in*: Jan. 2014, pp. 151–176, ISBN: 978-0-444-59513-3, DOI: 10.1016/B978-0-444-59513-3.00008-X.

[Mes19] Amir Messali, « Contribution to Rotor Position and Speed Estimation for Synchronous Machine Drive Using High Frequency Voltage Injection : Application to EV/HEV Powertrains », Theses, École centrale de Nantes, Nov. 2019, URL: https://tel.archives-ouvertes.fr/tel-02492255.

[MK16] Ludovic Merienne and Ahmed KETFI-CHERIF, « Dispositif de pilotage d'une boite de vitesses robotisée pour véhicule automobile à propulsion hybride », European pat. FR3058698, RENAULT SAS, Nov. 14, 2016.

[MK17] Ludovic Merienne and Ahmed KETFI-CHERIF, « Method for controlling the torque available on a hybrid vehicle while changing gears », patentwo WO2017/198913A1, RENAULT SAS, Nov. 23, 2017.

[MO79] A. Manitius and A.W. Olbrot, « Finite spectrum assignment problem for systems with delays », *in*: *IEEE Transactions on Automatic Control* 24.*4* (1979), pp. 541–552.

[MV00] G. Maggetto and J. Van Mierlo, « Electric and electric hybrid vehicle technology: a survey », *in*: *IEE Seminar Electric, Hybrid and Fuel Cell Vehicles (Ref. No. 2000/050)*, 2000, pp. 1/1–111, DOI: 10.1049/ic:20000261.

[NCC10] M. Njeh, S. Cauet, and P. Coirault, « Persistent disturbances rejection on Internal Combustion engine torque in Hybrid Electric Vehicles », *in*: *49th IEEE Conference on Decision and Control (CDC)*, 2010, pp. 6421–6426, DOI: 10.1109/CDC.2010.5717066.

[PFA18] PFA, *Contribution des véhicules légers et lourds à la réduction de la demande énergétique et des émissions de CO2 à horizon 2035 dans le monde*, tech. rep., 2018, URL: https://pfa-auto.fr/wp-content/uploads/2018/06/2018-Novembre-Note_technique_PFA.pdf.

[RET08] J-M. RETIF, *Commandes vectorielles des machines asynchrones et synchrones*, INSA Lyon, 2008.

[RO15] Rizzoni, Giorgio and Onori, Simona, « Energy Management of Hybrid Electric Vehicles: 15 years of development at the Ohio State University », *in*: *Oil Gas Sci. Technol. – Rev. IFP Energies nouvelles* 70.*1* (2015), pp. 41–54, DOI: 10.2516/ogst/2014006, URL: https://doi.org/10.2516/ogst/2014006.

[Rou+20a] S. Rouquet et al., « Power Management in Serial Hybrid Electric Vehicle: A singular perturbation approach. », *in*: *IFAC-PapersOnLine* 53.*2* (2020), Berlin, Germany, pp. 13775–13780, ISSN: 2405-8963, DOI: https://doi.org/10.1016/j.ifacol.2020.12.885.

[Rou+20b] Sébastien Rouquet et al., « Energy management in a mechatronics system with delay: A series hybrid electric vehicle case », *in*: *2020 IEEE Conference on Control Technology and Applications (CCTA)*, Montréal, Canada, 2020, pp. 679–684, DOI: 10.1109/CCTA41146.2020.9206269.

[Rou+21] Sébastien Rouquet et al., « Energy management in a mechatronics system with delay: A series hybrid electric vehicle case », *in*: *IEEE Transactions on Control Systems Technology*, 2021.

[Sch64] A. Schonung, « Static Frequency Changers with "Subharmonic" Control in Conjunction with Reversible Variable-Speed A.C.Drives », *in*: *Brown Boveri Review* 51 (1964), pp. 555–577.

[Sep17] Leopold Sepulchre, « Pour l'optimisation de la commande des machines synchrones à aimants permanents en régime de haute vitesse pour véhicule électrique », 2017INPT0025, PhD thesis, 2017, URL: http://www.theses.fr/2017INPT0025/document.

[SGA20] Yuri B. Shtessel, Malek Ghanes, and Roshini S. Ashok, « Hydrogen Fuel Cell and Ultracapacitor Based Electric Power System Sliding Mode Control: Electric Vehicle Application », *in*: *Energies* 13.*11* (June 2020), pp. 1–20, ISSN: 1996-1073, DOI: 10.3390/en13112798, URL: https://www.mdpi.com/1996-1073/13/11/2798.

[Sit09] L. Situ, « Electric Vehicle development: The past, present future », *in*: *2009 3rd International Conference on Power Electronics Systems and Applications (PESA)*, 2009, pp. 1–3.

[TM17] T. Tashiro and T. Maruyama, « Traction control design using model predictive control with fuel cut method for an internal combustion engine », *in*: *2017 IEEE Conference on Control Technology and Applications (CCTA)*, Aug. 2017, pp. 584–589, DOI: 10.1109/CCTA.2017.8062525.

[TS09] E. D. Tate and Peter J. Savagian, « The CO2 Benefits of Electrification E-REVs, PHEVs and Charging Scenarios », *in*: *SAE Technical Paper*, SAE International, Apr. 2009, DOI: 10.4271/2009-01-1311, URL: https://doi.org/10.4271/2009-01-1311.

[van+10] Oscar P.R. van Vliet et al., « Techno-economic comparison of series hybrid, plug-in hybrid, fuel cell and regular cars », *in*: *Journal of Power Sources* 195.*19* (2010), pp. 6570–6585, ISSN: 0378-7753, DOI: https://doi.org/10.1016/j.jpowsour.2010.04.077, URL: https://www.sciencedirect.com/science/article/pii/S0378775310007688.

[Vas63] A. B. Vasil'eva, « Asymptotic behavior of solutions to certain problems involving nonlinear differential equations containing a small parameter multipling the highest derivatives », *in*: *Rusian Math. Surveys* 18 (1963), pp. 13–18.

[XCC08] X. D. Xue, K. W. E. Cheng, and N. C. Cheung, « Selection of electic motor drives for electric vehicles », *in*: *2008 Australasian Universities Power Engineering Conference*, 2008, pp. 1–6.

[YPK14] M. Yildirim, M. Polat, and H. Kürüm, « A survey on comparison of electric motor types and drives used for electric vehicles », *in*: *2014 16th International Power Electronics and Motion Control Conference and Exposition*, 2014, pp. 218–223.

Titre : Gestion d'énergie optimisée pour véhicule hybride série

Mot clés : Véhicule hybride série, gestion d'énergie, moteur synchrone à aimants permanents, moteur à combustion interne, perturbation singulière.

Résumé : Cette thèse s'inscrit dans le cadre de la Chaire entre Renault et Centrale Nantes pour l'amélioration des performances des véhicules hybrides et électriques. La thèse est dédiée au développement de stratégies de contrôle pour un véhicule hybride série sans la batterie principale. En mode hybride série, le moteur à combustion interne est couplé à un générateur électrique pour produire la puissance utilisée par un deuxième moteur électrique pour propulser le véhicule. En l'absence de la batterie principale, le groupe motopropulseur possède deux petits tampons d'énergie, ce qui rend le système sensible à des faibles perturbations. De plus, le système a la particularité d'avoir trois échelles de temps différents, ce qui a conduit à plusieurs partitionnements des lois de commande. Ce partitionnement a été fait afin de maintenir le niveau de chaque tampon d'énergie, repousser les perturbations et améliorer le fonctionnement du groupe motopropulseur. Après avoir sélectionné une stratégie, les interrogations scientifiques ont porté sur la compréhension du couplage entre chaque échelle de temps et la stabilité du système. L'interaction entre les étages de contrôle a été étudiée avec l'approche des perturbations singulières et améliorée avec des observateurs. Les algorithmes et stratégies développés ont été testés en simulation et sur banc d'essai. Les résultats obtenus ont mis en évidence la faisabilité et les avantages des stratégies proposées dans la thèse.

Title: Optimized Energy Management for Serial Hybrid Vehicles

Keywords: Serial hybrid electric vehicle (HEV, PHEV), energy management, Permanent magnet synchronous machine, Internal combustion engine, Singular perturbation approach.

Abstract: This thesis is a part of the project Chair between Renault and Centrale Nantes for the improvement of EV/HEV propulsion performances. It is dedicated to proposed control strategies for a serial hybrid vehicle without the main battery. In the serial hybrid mode, the internal combustion engine is coupled with an electrical generator to produce power used by a second electric motor to propel the vehicle. In the absence of the main battery, the powertrain has small energy buffer, making the system sensitive to small disturbance. Moreover, the system presents the particularity of having three different time scales. The three time scales have been driving the control design to propose different strategies for partitioning the control in sub stage, maintaining the level of the energy storage, asses the perturbation and improves the operation of the powertrain. After proposing different strategies, the scientific interrogations have been the understanding of the coupling between each time scale and the stability of the overall system. The interaction of the control stage has been studied with the singular perturbation approach and improved with the observation method. The algorithms and strategies developed have been tested in simulation and on a test bench. The results obtained have highlighted the feasibility and the benefits of the strategies proposed in the thesis.